

ANALYZING POWER AND CROSS SECTION
DISTRIBUTIONS OF THE $^{12}\text{C}(p,p\alpha)^8\text{Be}$ CLUSTER
KNOCKOUT REACTION AT AN INCIDENT
ENERGY OF 100 MeV

by

Justin Mabiala



*Dissertation presented in partial fulfilment
of the requirements for the degree of
Doctor of Philosophy
at
Stellenbosch University*

Promoter: Prof A. A. Cowley

Co-promoter: Dr S. V. Förtsch

Date: March 2010

Declaration

By submitting this dissertation electronically, I declare that the entirety of the work contained therein is my own, original work, that I am the authorship owner thereof (unless to the extent explicitly otherwise stated) and that I have not previously in its entirety or in part submitted it for obtaining any qualification.

Signature:

Date: March 2010

Copyright © 2010 Stellenbosch University

All rights reserved

Abstract

The $(p, p\alpha)$ reaction on ^{12}C was investigated experimentally using polarized incident protons of 100 MeV. Coincident data, which were obtained at ten quasifree angle pairs for proton angles ranging from 25° to 110° , were analyzed in terms of the distorted-wave impulse approximation (DWIA). Calculated energy-sharing cross section and analyzing power distributions reproduce the data reasonably well. The observed agreement allows the extraction of distorted momentum distributions from experimental data. These distributions are very consistent over a wide range of angle pairs at which cross section energy-sharing distributions vary considerably.

Since measurements of analyzing powers were made, spin-orbit distortions were included in the DWIA calculations. The effects of spin-orbit distortions were found to be very small near zero recoil momentum and did not destroy the validity of the factorization approximation where the two-body $p\text{-}\alpha$ cross section enters as a multiplicative factor in the three-body $(p, p\alpha)$ cross section expression. Spectroscopic factors derived from the data are fairly consistent with the trend of the theoretical predictions.

Analyzing power data also follow the trend of free $p\text{-}^4\text{He}$ scattering data, and comparisons with DWIA predictions are in reasonable agreement. The theory reproduces also very well analyzing power angular distributions of the projectile-cluster two-body scattering at large angular momentum of the residual nucleus. This indicates that a quasifree knockout mechanism dominates the reaction.

The two-body interaction response between the projectile and the α cluster was found to resemble the scattering of protons from a free α particle to a remarkable degree, the present results strongly imply the existence of preformed α clusters in ^{12}C .

Opsomming

Die $(p, p\alpha)$ reaksie op ^{12}C is eksperimenteel ondersoek deur middel van gepolariseerde protone met 'n invalenergie van 100 MeV. Koïnsidensie data, wat verkry is by tien kwasi-vrye hoekpare, met proton hoeke tussen 25° en 110° , is geanaliseer in terme van die vervormde-golf-impuls-benadering (DWIA). Die berekende energie-verdeelde kansvlak en analiseervermoë verspreidings reproduseer die data redelik goed. Die waargenome ooreenstemming maak dit moontlik om vervormde momentumverdelings uit die eksperimentele data te verkry.

Aangesien analiseervermoë metings gedoen is, is spin-baan wisselwerking by die DWIA berekenige ingesluit. Die bydra as gevolg van spin-baan wisselwerking blyk baie klein te wees naby nul terugslag momentum en het nie die geldigheid van die faktoriseringsbenadering, waartydens die twee-deeltjie, $p\text{-}\alpha$ kansvlak as 'n vermenigvuldigingsfaktor in die uitdrukking vir die drie-deeltjie $(p, p\alpha)$ kansvlak verskyn, vernietig nie. Spektroskopiese faktore wat uit die data herlei is, is redelik konsistent met die verloop van die teoretiese voorspellings.

Analiseervermoë data volg ook die verloop van die vrye $p\text{-}^4\text{He}$ verstrooiings-data en vergelyk redelik goed met DWIA voorspellings. Die teorie reproduseer ook die hoekverdelings in die analiseervermoë van die twee-deeltjie projektiel-bondel verstrooiing by groot hoekmomentum waardes vir die oorblywende kern baie goed. Dit dui daarop dat 'n kwasi-vrye uitslaanmeganisme die reaksie domineer.

Die twee-deeltjie wisselwerkingsgedrag tussen die projektiel en die α -bondel toon sterk ooreenkomste met die verstrooiing van protone vanaf 'n vrye α -deeltjie. Die huidige resultate lewer sterk bewyse vir die bestaan van voorafgevormde α -bondels in ^{12}C .

Dedicated to my parents

Acknowledgements

I wish to express my sincere gratitude to my Promoter Prof. A.A. Cowley for suggesting this exciting project and for providing patient guidance throughout the period of my research work. I consider it an honour to have had the privilege of working with him.

I am grateful to my Co-promoter Dr. S.V. Förtsch for his constant encouragement, guidance and friendship.

I wish to acknowledge the help of Dr. R. Neveling for his invaluable help during the data analysis and for many fruitful discussions I had with him.

Many thanks go to Dr. F.D. Smit, Dr. E.Z. Buthelezi, Dr. G.F. Steyn, J.J. van Zyl and all the staff of iThemba LABS, for their valuable support in conducting the experiment successfully.

The invaluable assistance in computer environment provided by Dr. J.V. Pilcher from iThemba LABS is gratefully acknowledged.

A special word of thanks goes to the members of Nuclear Physics group from Stellenbosch University, Dr. S.M. Wyngaardt, Dr. P. Papka and J.J. van Zyl, for their interests and assistance.

My parents, my family, my colleagues and my friends, especially Gaelle Carine, definitely deserve my thanks for their support and love throughout the years.

This work is financially supported in part by the National Institute for Theoretical Physics (NiThep) and iThemba Laboratory for Accelerator Based Sciences through the South African National Research Foundation (NRF), to them I am very grateful.

Contents

1	Introduction	1
1.1	Historical Review of Alpha Clustering in Nuclei	1
1.2	Nuclear Structure and Nuclear Reactions	2
1.2.1	Quasifree knockout	3
1.2.2	Optical model	4
1.2.3	The shell model	7
1.3	Review of the Experiments Related to the Present Work	7
1.4	Purpose and Scope of This Study	9
1.5	Layout of This Dissertation	10
2	Theory	11
2.1	Overview	11
2.2	The Transition Amplitude and Energy Density	12
2.3	The Plane-wave Impulse Approximation	14
2.4	The Distorted-wave Impulse approximation	17
2.5	Calculations with the Computer Code THREEDEE	24

2.5.1	The two-body scattering amplitude	24
2.5.2	The bound state wave function	25
2.5.3	The distorted-wave functions	26
2.6	Analyzing Power	28
3	Experimental Details	29
3.1	Overview	29
3.2	The Facility	29
3.3	Polarimeters	30
3.3.1	K-line polarimeter	31
3.3.2	P-line polarimeter	32
3.4	Scattering Chamber	32
3.5	Targets	33
3.6	Detector Telescopes	34
3.7	Telescope positions	38
3.8	Electronics	39
3.8.1	Preamplifiers	39
3.8.2	Timing signals	40
3.8.3	Linear signals	43
3.8.4	Current Integrator	44
3.8.5	Pulsers	44
3.8.6	Clock	46

3.8.7	Event trigger	46
3.8.8	Computer busy	46
3.8.9	Pattern registers	46
3.8.10	Scalers	46
3.8.11	Computer interface	47
3.9	Data Handling	48
3.10	Experimental Procedure	48
4	Replay of Data	51
4.1	Overview	51
4.2	Energy Calibrations	51
4.2.1	Si detectors	51
4.2.2	NaI detector	52
4.3	Particle Identification	55
4.4	Timing Spectra	58
4.5	Experimental Data Corrections	59
4.5.1	Gain drifts	59
4.5.2	Dead layer energy corrections	60
4.5.3	Electronic and computer dead time	60
4.5.4	Subtraction of random coincidences	60
4.5.5	NaI reaction tail	61
4.6	Data Sorting	62

4.7	Energy Spectra	63
4.7.1	Two-dimensional energy spectra	63
4.7.2	Binding energy spectra	64
4.7.3	Energy-sharing Spectra	65
4.8	Polarization Measurements	65
4.9	Absolute Cross Section	68
4.10	Analyzing Power	70
4.11	Error Analysis	71
4.11.1	Statistical errors	71
4.11.2	Systematic errors	71
5	Results and Discussion	75
5.1	Overview	75
5.2	DWIA Calculations	76
5.2.1	The effect of the two-body $\left. \frac{d\sigma}{d\Omega} \right _{p-\alpha}$ off-shell cross section	76
5.2.2	Optical model potentials	78
5.3	Experimental Results	78
5.3.1	Energy-sharing cross section and analyzing power distributions	78
5.3.2	Spectroscopic factors	81
5.4	Tests of the Reaction Mechanism: DWIA Factorization	88
5.4.1	Comparison between knockout and elastic scattering	88
5.4.2	Alpha-cluster momentum distributions	92

5.4.3 Spin-orbit effects on analyzing power angular distribution	95
5.5 Sensitivity to Distorting Potentials and Bound State Wave Function of Cross Section Distributions	95
5.6 Analyzing Power Distributions at the Non-zero Recoil Momentum Condition	99
6 Summary and Conclusions	104
Bibliography	111
A Tabulation of Experimental Energy-sharing Cross Section Data	112
B Tabulation of Experimental Energy-sharing Analyzing Power Data	124

List of Figures

2.1	<i>Schematic diagram of the kinematics for a quasifree knockout reaction . . .</i>	12
2.2	<i>First Order Knockout Diagram in the Plane-wave Impulse Approximation .</i>	14
3.1	<i>A layout of the experimental facilities at iThemba LABS.</i>	30
3.2	<i>Experimental layout of the K-line polarimeter.</i>	31
3.3	<i>Experimental layout of the P-line polarimeter.</i>	32
3.4	<i>Particle detector telescopes T1 and T2</i>	35
3.5	<i>Scattering chamber setup</i>	36
3.6	<i>A block diagram of the timing electronics for telescopes T1 and T2.</i>	41
3.7	<i>Linear electronics for telescopes T1 and T2.</i>	43
3.8	<i>A simplified block diagram of the current integrator, the pulsers and the clock.</i>	45
4.1	<i>A characteristic energy spectrum of alphas from a ^{228}Th source generated for the $100\ \mu\text{m}$ Si detector. The α energies are in MeV.</i>	52
4.2	<i>Linear calibration curve for the $100\ \mu\text{m}$ Si detector.</i>	53
4.3	<i>An example of a raw NaI detector spectrum, used for the energy calibration, illustrating the separated peaks of the ground, the 1st and 3rd excited states in ^{12}C together with the pulser peak.</i>	54

4.4	<i>A linear calibration curve for the NaI detector.</i>	54
4.5	<i>Typical two-dimensional PID spectrum with a gate set around the proton locus.</i>	55
4.6	<i>Typical two-dimensional alpha PID spectrum with a gate set around the alpha-³He locus.</i>	56
4.7	<i>Typical two-dimensional mass function spectrum with a gate set around the α-particle locus. The y-axis is in arbitrary units.</i>	57
4.8	<i>Typical spectrum used to select alpha events at the three smallest proton angles with a gate set around the alpha locus. The gate was set according to the energy deposited by alphas which stopped in the detector T1A.</i>	58
4.9	<i>Typical representation of a TAC spectrum displaying the time structure over a time range of beam bursts obtained from coincidence events. True coincidence events are selected by the one-dimensional time gate 1 and random coincidence events by gate 2. The coincident pulser signals are well separated from any of the time peaks.</i>	59
4.10	<i>A typical two-dimensional energy spectrum. The gate is set around the quasifree ground-state knockout locus.</i>	64
4.11	<i>A typical binding energy spectrum for the reaction $^{12}\text{C}(p, p\alpha)^8\text{Be}$. The ground state (g.s.) and first excited state of the residual nucleus ^8Be are clearly resolved.</i>	65
4.12	<i>Typical energy-sharing spectrum. Counts as a function of proton energy obtained for p-α coincidence events.</i>	66
5.1	<i>Comparison of the on-shell p-α cross sections calculated from the final (FEP) and initial (IEP) energy prescriptions, and the half off-shell cross section.</i>	77

5.2 *Cross section distributions projected onto the proton energy axis for the reaction $^{12}\text{C}(p, p\alpha)^8\text{Be}(g.s.)$. Statistical error bars on the experimental values are indicated. The curves represent results of DWIA calculations with the distorting potentials set I and $p\text{-}^4\text{He}$ potential set I in Table 5.1. Spectroscopic factors for the theoretical cross section distributions are listed in Table 5.3. The proton energy which corresponds to zero recoil momentum of the residual nucleus is indicated with an arrow for each angle pair.* 82

5.3 *Cross section distributions projected onto the proton energy axis for the reaction $^{12}\text{C}(p, p\alpha)^8\text{Be}(g.s.)$. Statistical error bars on the experimental values are indicated. The curves represent results of DWIA calculations with the distorting potentials set I and $p\text{-}^4\text{He}$ potential set II in Table 5.1. Spectroscopic factors for the theoretical cross section distributions are listed in Table 5.4. The proton energy which corresponds to zero recoil momentum of the residual nucleus is indicated with an arrow for each angle pair.* 83

5.4 *Analyzing power distributions projected onto the proton energy axis for the reaction $^{12}\text{C}(p, p\alpha)^8\text{Be}(g.s.)$. Statistical error bars on the experimental values are indicated. The curves represent results of DWIA calculations with the distorting potentials set I and $p\text{-}^4\text{He}$ potential set I in Table 5.1. The proton energy which corresponds to zero recoil momentum of the residual nucleus is indicated with an arrow for each angle pair.* 84

5.5 *Analyzing power distributions projected onto the proton energy axis for the reaction $^{12}\text{C}(p, p\alpha)^8\text{Be}(g.s.)$. Statistical error bars on the experimental values are indicated. The curves represent results of DWIA calculations with the distorting potentials set I and $p\text{-}^4\text{He}$ potential set II in Table 5.1. The proton energy which corresponds to zero recoil momentum of the residual nucleus is indicated with an arrow for each angle pair.* 85

5.6 *Cross section and analyzing power distributions projected onto the proton energy axis for the reaction $^{12}\text{C}(p, p\alpha)^8\text{Be}(g.s.)$ at $\theta_p/\theta_\alpha = 110^\circ / -26.6^\circ$. The curves represent results of DWIA calculations, with distorting and $p\text{-}^4\text{He}$ potentials of respectively sets I and I (top panels) and sets I and II (bottom panels). Spectroscopic factors for the theoretical cross section distributions are listed in Tables 5.3 and 5.4. The proton energy which corresponds to zero recoil momentum of the residual nucleus is indicated with an arrow.* 86

5.7 *Comparison of energy-sharing cross section distributions for the reaction at $\theta_p/\theta_\alpha = 90^\circ / -35.7^\circ$ (left-hand panel). The open circles represent the data obtained in the previous work of Roos et al. [1] and the filled circles denote the data of this work. In the right-hand panel the cross section data of Roos et al. [1] and the data of this experiment normalized to the difference of 17% are shown.* 87

5.8 *Two-body cross section values (filled circles) as a function of the centre-of-mass scattering angle extracted from the experimental $^{12}\text{C}(p,p\alpha)^8\text{Be}(g.s.)$ cross sections at the quasifree peak (zero recoil momentum), compared with free $p\text{-}^4\text{He}$ elastic scattering data (open circles) and predictions of a factorized DWIA theory (curve). The average spectroscopic factor listed in Table 5.3 was used. The optical model parameters for $p\text{-}^4\text{He}$ used in the DWIA are from set I of Table 5.1.* 90

5.9 *Two-body cross section values (filled circles) as a function of the centre-of-mass scattering angle extracted from the experimental $^{12}\text{C}(p,p\alpha)^8\text{Be}(g.s.)$ cross sections at the quasifree peak (zero recoil momentum), compared with free $p\text{-}^4\text{He}$ elastic scattering data (open circles) and predictions of a factorized DWIA theory (curve). The average spectroscopic factor listed in Table 5.4 was used. The optical model parameters for $p\text{-}^4\text{He}$ used in the DWIA are from set II of Table 5.1.* 91

5.10	<i>Analyzing power distribution for the $^{12}\text{C}(p, p\alpha)^8\text{Be}(g.s.)$ reaction displayed as a function of the two-body centre-of-mass p-α scattering angle. Experimental values at the quasifree peak are represented by filled circles with statistical error bars and open circles correspond to free p-^4He elastic scattering data of Ref. [2]. The solid curve represents the result of an unfactorized DWIA calculation performed using set I of p-^4He optical model parameters in Table 5.1.</i>	93
5.11	<i>Analyzing power distribution for the $^{12}\text{C}(p, p\alpha)^8\text{Be}(g.s.)$ reaction displayed as a function of the two-body centre-of-mass p-α scattering angle. Experimental values at the quasifree peak are represented by filled circles with statistical error bars and open circles correspond to free p-^4He elastic scattering data of Ref. [2]. The solid curve represents the result of an unfactorized DWIA calculation performed using set II of p-^4He optical model parameters in Table 5.1.</i>	94
5.12	<i>Alpha-cluster momentum distributions at the nine angle pairs extracted from the experimental cross sections for the $^{12}\text{C}(p, p\alpha)^8\text{Be}$ reaction. Statistical error bars on the experimental values are indicated. The curves represent a Gaussian fit $f(x) = A\exp[-1/2(x/\sigma)^2]$ on the momentum distribution with $\sigma = 65$ and $A \approx 0.45$. The scale on the vertical axis is in arbitrary units.</i>	96
5.13	<i>Alpha-cluster momentum distributions at three angle pairs, as indicated, extracted from the experimental cross sections for the $^{12}\text{C}(p, p\alpha)^8\text{Be}$ reaction. Statistical error bars on the experimental values are indicated. The scale on the vertical axis is in arbitrary units.</i>	97
5.14	<i>Analyzing power distributions for the reaction plotted as a function of centre-of-mass angle. Solid and dashed curves represent DWIA calculations respectively by including (SO) and excluding (NSO) spin-orbit terms in generating distorted-waves. DWIA calculations were performed using set I of distorting potentials and set II of p-^4He optical model parameters in Table 5.1.</i>	98

5.15 *Comparison of energy-sharing cross section distributions with different optical potentials, as listed in Table 5.1. Three optical potential sets I, II and III are used in the reaction channels $p+^{12}\text{C}$ (left panels), $p+^8\text{Be}$ (centre panels), and $^4\text{He}+^8\text{Be}$ (right panels). Potential identifications in the figures are followed by numerical values of the spectroscopic factor for each case . . .* 100

5.16 *Comparison of energy-sharing cross section distributions with different values of the bound state radius parameter r_R (indicated as r in the left panels) and the diffuseness parameter a_R (indicated as a in the right panels). All curves are normalized to the peak cross section values at zero recoil momentum.* 101

5.17 *Dependence of the average extracted spectroscopic factor S_α as a function of bound state radius r_R (indicated as r in the left panel) and diffuseness parameters a_R (indicated as a in the right panel).* 102

5.18 *Analyzing power distributions for the $^{12}\text{C}(p, p\alpha)^8\text{Be}$ reaction displayed as a function of the two-body centre-of-mass scattering angle. Results are shown for three values of the recoil momentum of the ^8Be residue. Statistical error bars on the experimental values are indicated. The curves represent results of DWIA calculations.* 103

List of Tables

3.1	<i>Detector geometry parameters</i>	37
3.2	<i>Angle pairs $(\theta_p, \theta_\alpha)$ and the corresponding target angles. θ_p and θ_α represent the proton and alpha angles, respectively.</i>	39
3.3	<i>Detectors and preamplifiers</i>	40
3.4	<i>NIM modules used to process timing signals.</i>	40
3.5	<i>NIM modules used to process the linear signals.</i>	44
3.6	<i>Bit pattern register and scaler input definitions.</i>	47
4.1	<i>Set of calibration parameters for the different Si detectors.</i>	52
4.2	<i>Set of NaI(Tl) detector calibration parameters for each weekend.</i>	55
4.3	<i>Legendre polynomial coefficients fitted to the experimental data to generate the NaI detector response, taken from [3].</i>	63
4.4	<i>Summary of average values of the beam polarization and unpol for different weekends.</i>	67
4.5	<i>Summary of systematic errors.</i>	74
5.1	<i>Optical potential parameters. All optical potential depths are in MeV and all lengths are in fm. Set II of $p+^4\text{He}$ optical potential parameters reported in Ref. [4] are from this work.</i>	79

5.2	<i>Angle pairs, two-body centre-of-mass scattering angle, measured cross section and analyzing power values at the quasifree peak.</i>	80
5.3	<i>Spectroscopic factors for quasifree angle pairs extracted using the set I in Table 5.1 of $p+^4\text{He}$ potential parameters. $\langle S_\alpha \rangle^{exp}$ is a statistical average of all angles.</i>	81
5.4	<i>Spectroscopic factors for quasifree angle pairs extracted using the set II in Table 5.1 of $p+^4\text{He}$ potential parameters. $\langle S_\alpha \rangle^{exp}$ is a statistical average of all angles.</i>	88

Chapter 1

Introduction

1.1 Historical Review of Alpha Clustering in Nuclei

The idea of clustering in the nucleus has a long and distinguished history. Speculations about the existence of clusters such as alpha-particles have been around since the earliest days of nuclear physics. In fact the alpha-particle model of the nucleus was introduced by Gamow in 1929 [5] for explaining the results of his alpha-decay studies long before it was found to consist of two neutrons and two protons.

After the discovery of the neutron, proton-neutron models of the nucleus became popular. For example, the paper by Hafstad and Teller [6] which combined alpha- and single particle aspects was quite influential. Also, the resonating group method (RGM) which included cluster aspects microscopically was developed in 1937 by Wheeler [7]. The RGM uses antisymmetrized wave functions and takes proper account of the Pauli principle. It also leads to approximate ways of including Pauli principle effects, and allows different cluster structures to co-exist in the same nucleus. This model was further revived in 1941 when Margenau [8] presented his work related to the Hartree-Fock method by using trial wave functions which are antisymmetrized products of parametrized single particle wave functions. Although their mathematical approaches are somewhat different, the underlying physical ideas concerning the use of clustering as a means of dealing with collective phenomena in nuclei are the same in both cases.

With the rise of the shell model during the late 1940's these concepts of microscopic alpha-

cluster models were suppressed. However, the shell model failed to justify the coexistence of clusters in nuclei with the strong independent-particle properties. This problem was solved by introducing the harmonic oscillator shell model in the mid 1950's. This not only justified the alpha-particle model but also served to attract considerable attention owing to calculational simplification that the model offered. Further experimental evidence for the existence of clusters in nuclei came forth in nuclear emulsion studies in the 1950's [9] when protons with energies from $\simeq 40\text{--}600$ MeV incident on light through heavy targets led to energy and angular distributions of emitted alpha particles which differed significantly from what was expected from statistical theory of nuclear disintegration. Such an overabundance of emitted alphas was consistently found to be especially large in the forward direction, implying consequently direct quasifree collisions (see Section 1.2.1) between incident protons and "preformed alpha clusters" in the target nuclei.

1.2 Nuclear Structure and Nuclear Reactions

The best way of studying nuclei is to "disturb" them. This is realized through an interaction with other nuclei in order to find out more about their structure and how they can break-up during nuclear reactions.

The nuclear structure is generally described by the independent particle models. In these models the nucleons are assumed to either move nearly independently in a common nuclear potential, or in the case of the strongly interacting models the nucleons are strongly coupled to one another. As examples for the first models are the Fermi gas model and the shell model, whilst the liquid drop model and collective model are used as examples of the second models.

Many different reactions may occur during a collision between two nuclear particles. In elastic scattering, the incoming and outgoing particles are the same and the direction of the wave propagation is changed. On the other hand, in inelastic scattering the target nucleus (or the projectile) is left in an excited state as a result of the collision and so the kinetic energy in the exit channel will be less than that in the entrance channel. In general, the particles emerging from a collision will not be the same as the initial ones. Examples include simple pick-up and stripping transfer reactions involving mass exchange between

particles. Many other types of reactions may occur in which one or both colliding nuclei are changed. For example, an energetic projectile may knock a piece out of the target nucleus (knockout reaction) or be broken up during the collision.

A reaction in which the projectile fuses with the target to form a compound nucleus, which later may emit one or more particles is called a compound nuclear reaction. Direct reactions on the other hand involve an interaction between the incident projectile and one nucleon or few nucleons in the target nucleus. Reactions which involve medium energy protons (100 to 1000 MeV) are expected to proceed mainly via a direct reaction mechanism. Direct reactions take place in the time it takes for the incident particle to traverse the target nucleus, which is about 10^{-22} to 10^{-23} s, depending on the incident energy and target nucleus. In compound nucleus reactions, the energy that is transferred from the projectile to the target is divided among the constituent nucleons until statistical equilibrium is established which may persist for approximately 10^{-16} to 10^{-18} s.

In the next two subsections a brief introduction to quasifree knockout (which is the basic reaction mechanism implicated in our study) and the optical model, which is used to generate distorted waves in the theory, is given. This is followed by a third subsection to summarize the shell model which is needed to postulate the structure of a cluster-core configuration.

1.2.1 Quasifree knockout

Quasifree scattering may be defined as the interaction between an incident projectile and a nucleon (or a cluster of nucleons) in a target nucleus, which proceeds in an analogous way to free scattering; the remaining nucleus has a small influence on the direct reaction. Quasifree scattering is one of the most direct ways of investigating the single particle properties of the nucleus, namely, the shell structure and the effects on the bound nucleons in the nucleus. Quasifree knockout reactions are used to probe nuclear information such as the separation energies, spectroscopic factors, medium effects, nuclear distortions.

The quasifree scattering differs from free scattering by the separation energy associated with the bound nucleon. This energy is needed to separate the bound nucleon from the nucleus while in free scattering, all the energy of the incoming particle is available as kinetic

energy of the two outgoing particles.

Nucleons are bound in the nucleus and are in ceaseless motion due to the interplay of the attractive and repulsive part of the strong nucleon-nucleon force. Information on the momentum distribution of the knocked out particle in the nucleus can be obtained experimentally by simultaneously observing a scattered high-energy projectile and the particle knocked out from a certain nuclear state. Therefore, for any given projectile energy, the binding energy spectrum of the emerging particle pairs, calculated by means of energy conservation, should show various peaks. These peaks are expected at the separation energies corresponding to the various nuclear shells from which the bound particles were ejected. The width of such peaks is related to the lifetime of the created hole through the uncertainty principle.

In nuclear shell studies, quasifree scattering experiments have an advantage to reach low momentum states in the nucleus, while transfer reactions involve high momentum nucleons of the outer shells due to increased absorption and reflection effects of the nucleus on the ejectile's wave function [10].

The theoretical formulation of the quasifree scattering process can be developed if two simplified assumptions are made. Such assumptions give rise to the plane-wave impulse approximation (PWIA) and the distorted-wave impulse approximation (DWIA) which will be clearly discussed in Chapter 2.

1.2.2 Optical model

The optical model is one of the simplest and most successful nuclear models for describing elastic scattering [11]. As described before, the simplest direct interaction between an incident particle and a target nucleus is elastic scattering. In this reaction, the particle's direction of motion is changed without loss of energy in the centre-of-mass of the system. The compound nucleus reaction can also at low energies contribute to elastic scattering. This is explained when a particle of the same type as the projectile is emitted from the compound nucleus with the full energy. Direct elastic scattering occurs only when the incident particle interacts with the nucleus as a whole. The optical potential describes such an interaction well.

The optical potential was first introduced for the purpose of describing the elastic scattering of nucleons from nuclei. In this way direct reactions are considered as a perturbation on the elastic scattering. In general, most of the reaction cross sections are small compared with the elastic cross section. In fact, charged nuclear projectiles can scatter elastically at very low bombarding energy. As the energy is increased, inelastic and reaction channels open and some flux is removed from the elastic scattering channel. This may be accounted for in allowing the potential to be complex, so in its simplest form the optical potential may be written

$$V(r) = -U(r) - iW(r) , \quad (1.1)$$

where U and W are selected to give the potential its proper radial dependence, and r represents the distance between the nucleon and the centre-of-mass of the target nucleus. The real part of the potential, $U(r)$, concerns elastic scattering. It describes the ordinary nuclear interaction between the target and projectile and is related to a single shell model potential. The imaginary part of the potential, $W(r)$, is responsible for the attenuation of the incoming wave, as part of the incident flux that is removed during the reaction process.

The potential $V(r)$ defined in Eq. (1.1) depends only on the position of the projectile relative to the centre of the nucleus, thus a mean field or local potential. However, the nucleus consists of individual nucleons that affect the mean field potential. In cases where the potential is not dependent only on the position of the nucleon whose movement is to be described, but also on the relative positions of the other nucleons in the nucleus, the potential is called a non-local potential. The simplest manner to include these non-localities in the single-particle potential approximation is to rewrite the time independent Schrödinger equation in the following way [12]

$$\left(-\frac{\hbar^2}{2m}\nabla^2 - E \right) \psi(\vec{r}) = - \int d^3r' V(\vec{r}, \vec{r}') \psi(\vec{r}') , \quad (1.2)$$

with $\psi(\vec{r})$ the local wave function and $V(\vec{r}, \vec{r}')$ the so-called non-local potential. In a

coordinate representation, a non-local potential operating on a wave function has the form

$$V\psi(\vec{r}) = \int V(\vec{r}, \vec{r}')\psi(\vec{r}')d\vec{r}'. \quad (1.3)$$

Usually the range of the non-locality is small, so that the non-local potential tends rapidly to zero as $|r - r'|$ increases. Equation (1.3) may then be expanded in a Taylor series about the point $r = r'$ such that

$$\int d^3r' V(\vec{r}, \vec{r}')\psi(\vec{r}') = \left(\int d^3r' V(\vec{r}, \vec{r}') e^{i(\vec{r}' - \vec{r}) \cdot \vec{p} / \hbar} \right) \psi(\vec{r}) = V(\vec{r}, \vec{p})\psi(\vec{r}). \quad (1.4)$$

Hence a non-local potential is equivalent to an energy-dependent local potential $V(\vec{r}, \vec{p})$. It is therefore possible to correct for the non-locality of the potential by incorporating an energy-dependent correction factor into the local optical potential.

Perey and Buck studied the consequences of employing a non-local optical potential in analyses of elastic scattering by assuming [13]

$$V(\vec{r}, \vec{r}') = U \left(\frac{1}{2} |\vec{r} + \vec{r}'| \right) H \left(|\vec{r} - \vec{r}'| \right), \quad (1.5)$$

with $H \left(|\vec{r} - \vec{r}'| \right)$ chosen to be a Gaussian function

$$H \left(|\vec{r} - \vec{r}'| \right) = \pi^{-3/2} \beta^{-3} \exp \left\{ - \left(\frac{|\vec{r} - \vec{r}'|}{\beta} \right)^2 \right\}, \quad (1.6)$$

where β is the range of the non-locality. H is normalized so that $\int H \left(|\vec{r} - \vec{r}'| \right) d\vec{r}' = 1$, and U is taken to have the conventional complex Woods-Saxon form.

Finally, the relation between the local and non-local potentials was found to be

$$V_{non-local}(r) = V_{local}(r) \exp \left[\frac{\mu \beta^2}{2\hbar^2} (E - V_{local}(r)) \right], \quad (1.7)$$

where μ is the appropriate reduced mass. Typical values for β are 0.85 fm for nucleons, 0.54 fm for deuterons, 0.2 – 0.3 fm for ^3H and ^3He particles and ~ 0.2 fm for alphas.

1.2.3 The shell model

The shell model is based on the assumption that each nucleon moves in a potential well which is an approximate representation of the interaction of that nucleon with all the other nucleons [14]. The Schrödinger equation for this potential supports the claim that nucleons can only occupy a set of discrete energy levels described by a set of four quantum numbers, namely, the principal quantum number (n), the orbital quantum number (l), the total angular momentum quantum number (j), and the projection of the total angular momentum (m_j). Nucleons being fermions, they obey the Pauli exclusion principle which states that no two nucleons with the same set of quantum numbers can be in the same energy state. The occupation number of each j -orbital of a nucleus is then $(2j + 1)$.

In order to predict the nuclear magic numbers, the potential should be modified by including a spin-orbit potential [15, 16]. The spin-orbit interaction describes the interaction between the spin (s) and the orbital momentum (l) of a single nucleon in which they combine to form a total angular momentum (j). This coupling interaction causes an energy splitting of the energy levels.

1.3 Review of the Experiments Related to the Present Work

For many decades, the cluster structure of nuclei in excited states, as well as in the ground state, has become of increasing interest in nuclear physics. Since a free alpha-particle is a particularly stable configuration, it is tempting to predict the existence of alpha-clusters in nuclei. One might ask whether these clusters are real entities or simply a way of carrying out calculations to describe observables appropriately for a many-body system.

To investigate alpha-clustering in nuclei experimentally, one needs to know whether four nucleons (two protons and two neutrons) in a nucleus can form an alpha-cluster. The most direct experimental method of studying ground-state alpha-clustering in nuclei is by means of a knockout reaction [17, 9, 18, 1, 19]. In such a reaction, the knocked out cluster is observed in coincidence with the projectile. In fact, the existence of clusters of nucleons would clearly be supported if the momentum distribution of the clusters deduced from the

coincidence spectra of emitted particles is in agreement with the expected distribution of a “preformed” cluster bound in the target nucleus. Moreover, the absolute spectroscopic factors extracted from the coincidence results should in principle be in agreement with theoretical expectation.

Previous studies for the alpha-cluster structure of the ground state wave function of light nuclei ${}^6\text{Li}$, ${}^7\text{Li}$, ${}^9\text{Be}$ and ${}^{12}\text{C}$ by means of the $(p, p\alpha)$ quasifree reaction at energies between 100 MeV and 296 MeV, gave encouraging results [1, 20, 18, 21, 22]. In these studies, good shape agreement between DWIA calculations and experimental energy-sharing differential cross section data, as well as between extracted spectroscopic factors and theoretical expectations, were observed.

Carey *et al.* investigated [9] the $(p, p\alpha)$ reaction at an incident energy of 100 MeV at quasifree kinematics for target nuclei heavier than ${}^{12}\text{C}$, specifically the nuclei ${}^{16}\text{O}$, ${}^{20}\text{Ne}$, ${}^{24}\text{Mg}$, ${}^{28}\text{Si}$, ${}^{32}\text{S}$, ${}^{40}\text{Ca}$, ${}^{48}\text{Ti}$, ${}^{54}\text{Fe}$, and ${}^{66}\text{Zn}$. Satisfactory agreement between experimental energy-sharing cross section distributions and predictions of DWIA calculations was found. Also, similar results followed from studies of the ${}^{40}\text{Ca}(p, p\alpha)$ reaction in non-coplanar kinematics [17].

With polarized proton beams, more detailed tests of the DWIA description of $(p, p\alpha)$ reactions become possible. For example, measurements of $(p, p\alpha)$ analyzing powers can be compared to analyzing powers measured in free p - α scattering and if these two quantities are in agreement, it points to a very simple reaction mechanism in the knockout process [18]. Therefore, the ability to reproduce experimental analyzing powers acts as a rigorous test of the reaction dynamics, which consequently influences conclusions drawn about the cluster structure of the studied nuclei [22]. Wang *et al.* [18] found satisfactory agreement between the energy-sharing analyzing power distribution and DWIA calculations for the ${}^9\text{Be}(p, p\alpha)$ reaction at 150 MeV. In the same way, Yoshimura *et al.* [22] confirmed the results for the $(p, p\alpha)$ reaction at 296 MeV for the targets ${}^6\text{Li}$, ${}^7\text{Li}$ and ${}^9\text{Be}$. This confirms that the reaction is largely a quasifree process for these nuclei. However, for the ${}^{12}\text{C}(p, p\alpha)$ reaction at 296 MeV, significant differences between the experimental analyzing power and DWIA calculations were observed [22]. Although only two angle pairs were investigated, it was speculated that this is due to significant contributions from processes other than quasifree scattering such as the sequential decay following the excitation of the target

nucleus and multistep processes which are kinematically indistinguishable.

The first investigation of the analyzing power on a target as heavy as ^{40}Ca for the test of the alpha-cluster knockout reaction failed to confirm the standard interpretation [23]. Consequently, this new investigation will focus on a lighter target namely ^{12}C , which is a nucleus that should in principle be less sensitive to certain ingredients of the DWIA. Another advantage is that ^{12}C has been studied more extensively than ^{40}Ca in knockout experiments [1, 24, 25].

1.4 Purpose and Scope of This Study

This study aims to investigate alpha-clustering in ^{12}C by means of a $(p, p\alpha)$ knockout reaction at an incident energy of 100 MeV. Analyzing power and cross section distributions were measured under quasifree kinematic conditions and compared with distorted-wave impulse approximation (DWIA) calculations.

The incident energy was chosen to facilitate comparison of our cross section results with the data at one of the three p - α angle pairs measured earlier by Roos *et al.* [1]. Whereas the work of Roos *et al.* was restricted to a very narrow range of p - α two-body scattering angles, the advantage of our investigation is that a much larger angular range is covered. This makes a comparison of our experimental coincidence data with free p - ^4He elastic scattering more meaningful. In addition, we studied the analyzing power, which is an observable that is more sensitive to the details of the reaction mechanism than cross sections, as we have mentioned before.

Our study is also superior to the earlier work of Yoshimura *et al.* [22] at 296 MeV, which suffers both from a lack of resolution of the knockout reaction to the ground and first excited state of the residual nucleus, as well as the limitation of exploring only two coincident angle pairs.

1.5 Layout of This Dissertation

The remaining body of this work is presented as follows: Chapter 2 describes the theoretical calculations which were performed for comparison with the experimental data. In Chapter 3 the experimental set up and the procedures followed to execute the experiment are described. This is followed by Chapter 4 describing all the procedures employed in the analysis of the measured data, while Chapter 5 presents results of the experimental data and theoretical calculations. Finally, the conclusions of the present study are summarized in Chapter 6.

Chapter 2

Theory

2.1 Overview

This chapter discusses the theoretical models which underlie the current experiment. The quasifree knockout reaction that refers to a process in which a projectile knocks the bound nucleon out of the nucleus, without any further violent interactions between the projectile and the residual nucleus, is applied. This process gives rise to two assumptions. The first is that the collision time is short and the collision may be described by an impulse approximation [26]. The second is that, no interaction, between the projectile and the target nucleus before the collision and also between the outgoing particles and the residual nucleus or between the outgoing particles, is taken into account. Therefore in this approximation, the residual nucleus recoils with the same momentum that it had before the interaction. These assumptions result in the Plane-wave Impulse Approximation (PWIA) in which the wavefunctions for the incident particle and scattered nucleons can be represented by plane-waves [27]. By taking into account the interactions before and after the quasifree event, the Distorted-wave Impulse Approximation (DWIA) is defined. However, the interactions included in this approach distort the incident and outgoing wave functions [28].

In the following sections the PWIA and DWIA formulation, and the computer code THREEDEE that is used to calculate the cross sections and analyzing powers predicted by these two models are discussed.

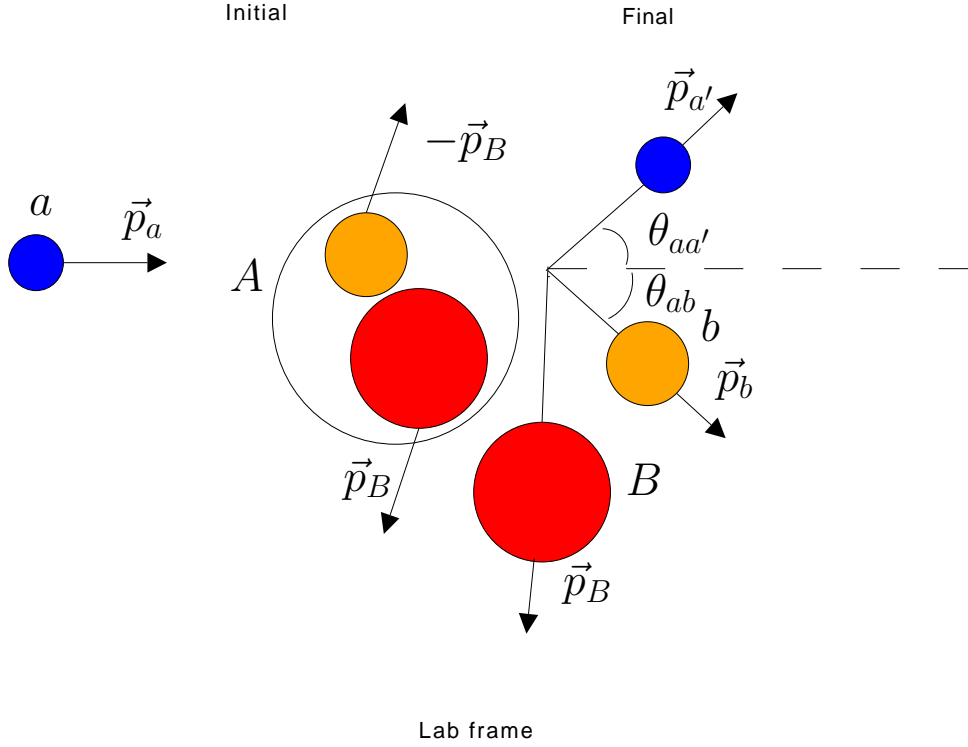


Figure 2.1. Schematic diagram of the kinematics for a quasifree knockout reaction

2.2 The Transition Amplitude and Energy Density

Consider the reaction $A(a, a'b)B$ where A is the target nucleus, a the incoming proton, a' and b the outgoing particles and B the residual nucleus. The incident proton, a , knocks out a bound nucleon, b , from a specific orbital in the target nucleus, A , resulting in three particles in the final state, namely the recoil residual nucleus, B , and two outgoing particles, a' and b (Fig. 2.1). Within the framework of this model, the residual core nucleus, B , is a spectator to the reaction, meaning that its momentum remains unchanged during the collision. The prime serves to identify the particle a in the exit channel.

The differential cross section for the knockout reaction is given by [28]

$$\sigma_{fi} = \frac{2\pi}{\hbar v} |T_{fi}|^2 \omega_f, \quad (2.1)$$

where v is the relative velocity of a and A in the entrance channel, ω_f is the energy density of final states and T_{fi} is the transition amplitude.

The reduced transition amplitude T_{fi} is given by [28]

$$T_{fi} = \langle \Phi^{(-)}(\widetilde{B}, \widetilde{a}', b) | V_{a'b} | \psi^{(+)}(\widetilde{A}, \widetilde{a}) \rangle , \quad (2.2)$$

where $\psi^{(+)}(\widetilde{A}, \widetilde{a})$ is the exact wave function for the initial system, $\Phi^{(-)}(\widetilde{B}, \widetilde{a}', b)$ represents the wave function of the exit channel in the absence of any interaction between outgoing particles a' and b and $V_{a'b}$ is the difference between the exact Hamiltonian and the Hamiltonian used to generate $\Phi^{(-)}(\widetilde{B}, \widetilde{a}', b)$. The symbol \sim serves as the reminder that both wave functions are antisymmetric with respect to interchange of any two nucleons.

Introducing the wave function $\Phi(\widetilde{A}, \widetilde{a})$ for the initial state in the absence of V_{ab} , the interaction between the projectile a and the cluster b , and defining the transition operator t_{fi} as [28]

$$V_{a'b} | \psi^{(+)}(\widetilde{A}, \widetilde{a}) \rangle = t_{fi} | \Phi^{(+)}(\widetilde{A}, \widetilde{a}) \rangle , \quad (2.3)$$

it follows that, the reduced transition amplitude can be written as [28]

$$T_{fi} = \langle \Phi^{(-)}(\widetilde{B}, \widetilde{a}', b) | t_{fi} | \Phi^{(+)}(\widetilde{A}, \widetilde{a}) \rangle . \quad (2.4)$$

Considering the problem of constructing antisymmetrised wave functions and neglecting exchange effects between the projectile a and the core B , the expression (2.4) becomes [29]

$$T_{fi} \approx \langle \psi(\widetilde{B}) \mathcal{Q}_{ab} \eta_{Ba'b}^{(-)} \psi(\widetilde{a}') \psi(\widetilde{b}) | t_{fi} | \mathcal{Q}_{ab} \eta_{Aa}^{(+)} \psi(\widetilde{a}) \psi(\widetilde{A}) \rangle , \quad (2.5)$$

where ψ are internal wave functions for the various particles, $\eta_{Aa}^{(+)}$ and $\eta_{Ba'b}^{(-)}$ describe respectively the relative motion of the centres of mass of the particles in the entrance and exit channels and the operator \mathcal{Q}_{ab} is an antisymmetrizer between nucleons in the projectile and the b nucleons which are ejected.

The energy density of final states in the laboratory system may be written as [29]

$$\omega_f = \frac{d^3 \vec{p}_{a'}}{(2\pi\hbar)^3} \frac{d^3 \vec{p}_b}{(2\pi\hbar)^3} \frac{1}{dE} , \quad (2.6)$$

where E is the total energy and p_i is the momentum of the outgoing particle i .

Substituting $E_{a'} dE_{a'} = c^2 p_{a'} dp_{a'}$ and $d^3 p_i = p_i^2 dp_i d\Omega_i$ yields

$$\omega_f = \frac{p_{a'} E_{a'} dE_{a'} d\Omega_{a'} p_b^2 dp_b d\Omega_b}{(2\pi\hbar)^6 c^2 dE} , \quad (2.7)$$

where Ω_i is the solid-angle element within which scattered particle i is detected.

Writing the total energy as

$$E = \sqrt{p_{a'}^2 c^2 + m_{a'}^2 c^4} + \sqrt{p_b^2 c^2 + m_b^2 c^4} + \sqrt{(\vec{p}_a - \vec{p}_{a'} - \vec{p}_b)^2 c^2 + m_B^2 c^4} + Q, \quad (2.8)$$

fixing $E_{a'}$ and taking the differential of E results in,

$$dE = \frac{c^2 p_b dp_b}{E_b} + \frac{c^2 (p_b - p_a \cos \theta_{ab} + p_{a'} \cos \theta_{a'b}) dp_b}{E_B}, \quad (2.9)$$

where $\theta_{a'b}$ and θ_{ab} are the angles between $\vec{p}_{a'}$, \vec{p}_b and \vec{p}_a , \vec{p}_b , respectively. The energy Q is required to remove particle b from the target nucleus A .

The substitution of Eq. (2.9) into Eq. (2.6) leads to the following expression for the energy density

$$\omega_f = \frac{v \hbar E_a E_{a'} E_b p_{a'} p_b c}{(\hbar c)^7 (2\pi)^5} \frac{p_{a'} p_b c}{p_a} \left[1 + \frac{E_b}{E_B} \left(1 - \frac{p_a}{p_b} \cos \theta_{ab} + \frac{p_{a'}}{p_b} \cos \theta_{a'b} \right) \right]^{-1} d\Omega_a d\Omega_b dE_{a'}. \quad (2.10)$$

2.3 The Plane-wave Impulse Approximation

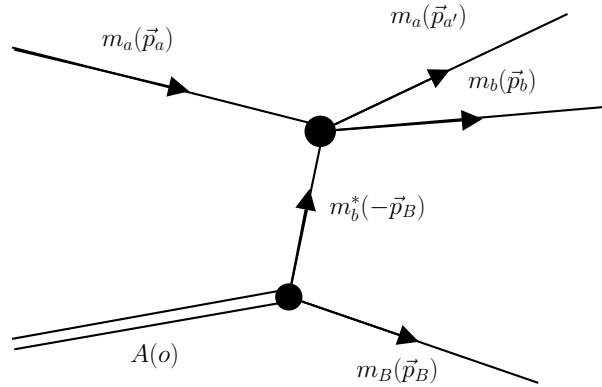


Figure 2.2. First Order Knockout Diagram in the Plane-wave Impulse Approximation

The simplest theory for knockout reactions is the plane-wave impulse approximation (PWIA), or spectator model. Figure 2.2 shows the first-order diagram representing the knockout reaction. The lower vertex represents the breakup of the target nucleus into residual nucleus and cluster b . The upper vertex shows the interaction of particles a and b which ejects the cluster from the nucleus. No interaction between the incident and emitted particles with the residual nucleus is taken into account. Since this model does not take into account aforementioned interactions, the wave functions η defined in Eq. (2.5) are replaced by asymptotic plane-waves in the form $\eta \sim e^{i\vec{p}\vec{r}}$. If spin is neglected, $\psi(\tilde{a}')$, $\psi(\tilde{b})$ and $\psi(\tilde{a})$ are ignored and T_{fi} is modified as [30]

$$T_{fi} \approx \int \int d\vec{r}_{a'} d\vec{r}_b e^{-i\vec{p}_{a'}\vec{r}_{a'}} e^{-i\vec{p}_b\vec{r}_b} t_{fi}(|\vec{r}_{a'} - \vec{r}_b|) e^{i\vec{p}_a\vec{r}_a} \psi_\alpha(\vec{r}_b), \quad (2.11)$$

where r_i is the coordinate of particle i referred to some arbitrary origin. ψ_α is the nuclear overlap integral between the internal wave function of the target nucleus and the internal wave functions for the residual nucleus and the bound particle which can be written as [31]

$$\psi_\alpha(\vec{r}_b) = \int dr \psi_B^*(r) \psi_A(r, \vec{r}_b). \quad (2.12)$$

The PWIA triple differential cross section can then be written as [1]

$$\frac{d^3\sigma}{d\Omega_{a'} d\Omega_b dE_{a'}} \propto K_F \left. \frac{d\sigma}{d\Omega} \right|_{ab} \cdot |\phi(-\vec{p}_B)|^2, \quad (2.13)$$

where :

- K_F is a kinematic factor calculated from kinematic values given by

$$K_F = \frac{E_a E_{a'} E_b}{(\hbar c)^7 (2\pi)^5} \frac{p_{a'} p_b c}{p_a} \left[1 + \frac{E_b}{E_B} \left(1 - \frac{p_a}{p_b} \cos \theta_{ab} + \frac{p_{a'}}{p_b} \cos \theta_{a'b} \right) \right]^{-1}; \quad (2.14)$$

- $\left. \frac{d\sigma}{d\Omega} \right|_{ab}$ is a half off-shell $a - b$ scattering cross section for the interaction of particles a and b (upper vertex of Fig. 2.2) given by

$$\left. \frac{d\sigma}{d\Omega} \right|_{ab} \propto |\langle \vec{p}_{a'}, \vec{p}_b | t_{fi} | \vec{p}_a, -\vec{p}_B \rangle|^2 ; \quad (2.15)$$

$\left. \frac{d\sigma}{d\Omega} \right|_{ab}$ is an off-shell or more correctly a half-off-shell cross section because particle b in the target is virtual; i.e., two-body momentum and energy conservation are not satisfied due to the binding of the cluster b to the nucleus. The invariant mass m_b^* of particle b is not m_b but rather [32]

$$m_b^* = [(m_b - BE - E_B)^2 - p_B^2] \approx m_b - \left[BE + p_B^2 \left(\frac{m_b + m_B}{2m_b m_B} \right) \right] = m_b - \left[BE + \frac{p_B^2}{2\mu} \right] ,$$

where BE is the binding energy of A against break-up into $b + B$ and E_B is the kinetic energy of B . The quantity $m_b - m_b^*$ is the distance ΔE off the mass shell and it can be seen that particle b in the target nucleus A is always off the mass shell by at least BE ;

- and $\phi(-\vec{p}_B)$ represents the momentum distribution of the knocked out particle in the nucleus. It is the Fourier transform of the overlap integral between the internal wave function of the target nucleus and the internal wave functions for the residual nucleus and the bound particle; i.e. [33],

$$\phi(-\vec{p}_B) = \frac{1}{(2\pi)^{1/2}} \int e^{i\vec{p}_B \vec{r}_b} \psi_\alpha(\vec{r}_b) d\vec{r}_b . \quad (2.16)$$

Since the core nucleus B is treated as a spectator, its momentum \vec{p}_B after the collision is the same as it was before the collision. Hence the momentum of the bound particle inside the nucleus is $-\vec{p}_B$ because the target nucleus was initially at rest. The quantity $|\phi(-\vec{p}_B)|$ is thus the probability density of finding the particle b in the target A in a state of momentum $-\vec{p}_B$.

The PWIA unfortunately fails to explain the details of the data if the projectile energy is not large enough. This inadequacy comes from the fact that, this model totally ignores the effect of the core nucleus on the scattered particles. One possible extension is to a multiple scattering theory, where one explicitly includes double scattering, triple scattering, etc. However, this procedure is too difficult to carry out any very realistic calculation [34].

2.4 The Distorted-wave Impulse approximation

In the DWIA, the interaction between the incoming and outgoing particles with the target nucleus and recoiling nucleus are taken into account. The wave functions for relative motion η are replaced by distorted-wave functions χ generated from optical potentials.

A factorized form for T_{fi} is obtained by making the additional assumption that the resultant two-body t_{fi} matrix varies sufficiently slowly with momenta that its arguments may be replaced by their asymptotic values, giving [28]

$$T_{fi} = C \sum_{\alpha L J \sigma_b \Lambda M} S_{\alpha L J}^{1/2}(J M J_B M_B | J_A M_A)(L \Lambda s_b \sigma_b | J M)(2L + 1)^{1/2} \\ \times T_{fi}^{\alpha L \Lambda} \langle \vec{k}_f, \sigma'_a, \sigma'_b | t_f^+ | \vec{k}_i, \sigma_a, \sigma_b \rangle, \quad (2.17)$$

where J_A and J_B are respectively the angular momentum quantum numbers for the target nucleus and residual nucleus, the corresponding quantities for the incident and emitted particles are s_i (projection σ_i), the relative angular momentum of b and B is L (projection Λ), and any other quantum numbers needed to specify the motion are in α . \vec{k}_i and \vec{k}_f are the initial and final relative momenta of particles a and b respectively. C is the isospin coupling (Clebsch-Gordan) coefficient and $t_f^{(+)}$ is the two-body operator for the free $a + b$ scattering process by assuming that the incident particle interacts with only one target nucleon (impulse approximation).

$T_{fi}^{\alpha L \Lambda}$ is the so-called distorted momentum distribution evaluated as follows [28]

$$T_{fi}^{\alpha L \Lambda} = (2L + 1)^{-1/2} \langle \eta_{Ba'b}^{(-)} | \delta(\vec{r}_a - \vec{r}_b) | \eta_{Aa}^{(+)} \phi_{L\Lambda}^{\alpha}(\vec{r}_{bB}) \rangle, \quad (2.18)$$

where $\phi_{L\Lambda}^{\alpha}(\vec{r}_{bB})$ describes the motion of the centre-of-mass of b with respect to the centre-of-mass of B .

Averaging over initial spin projections and summing over final spin projections, and making the further assumption that the two-body t matrix is independent of σ_b and $T_{fi}^{\alpha L\Lambda}$ is independent of α , the DWIA triple differential cross section for specific values of L and J can be written as [28]

$$\frac{d^3\sigma^{LJ}}{d\Omega_{a'}d\Omega_b dE_{a'}} = K_F C^2 S_{LJ} |\overline{\langle t \rangle}|^2 \sum_{\Lambda} |T_{fi}^{\alpha L\Lambda}|^2, \quad (2.19)$$

where

$$|\overline{\langle t \rangle}|^2 = \frac{1}{(2s_a + 1)(2s_b + 1)} \sum_{\sigma_a \sigma_b \sigma'_a \sigma'_b} \left| \langle \vec{k}_f, \sigma'_a, \sigma'_b | t_f^{(+)} | \vec{k}_i, \sigma_a, \sigma_b \rangle \right|^2, \quad (2.20)$$

is the square of the two-body $a - b$ free scattering t -matrix averaged over initial spin states of $a + b$ and summed over the final spin states of $a' + b$. $C^2 S_{LJ}$ is the spectroscopic factor which represents the probability to reach a single particle-hole state LJ when a nucleon is removed from the target nucleus.

More simply, the DWIA triple differential cross section, ignoring spin-orbit terms in the optical potentials for $A(a, a')B$ reaction, is given by the following factorized expression [1]

$$\frac{d^3\sigma^{LJ}}{d\Omega_{a'}d\Omega_b dE_{a'}} = K_F C^2 S_{LJ} \sum_{\Lambda} |T_{fi}^{\alpha L\Lambda}|^2 \left(\frac{d\sigma}{d\Omega} \right)_{a-b}, \quad (2.21)$$

with $\left(\frac{d\sigma}{d\Omega} \right)_{a-b}$, the two-body $a - b$ cross section.

Assuming that $V_{aA} - V_{ab} = V_{aB}$ where V_{aB} is the optical potential for $a + B$ scattering averaged over the target nucleus A , $\eta_{Aa}^{(+)}$ satisfies the wave equation

$$(T_{aA} + V_{aB} - \varepsilon_{aA})\eta_{Aa}^{(+)} = 0, \quad (2.22)$$

where

$$T_{aA} = -\frac{\hbar^2}{2\mu_{aA}} \nabla_{aA}^2 ,$$

is the relative kinetic operator between particles a and A , μ_{aA} is the reduced mass of a and A and ε_{aA} is the relative kinetic energy defined by

$$\varepsilon_{aA} = \frac{p_{aA}^2}{2\mu_{aA}} ,$$

with

$$\vec{p}_{aA} = \hbar k_{aA} \frac{A}{a+A} \vec{p}_a ,$$

and \vec{p}_a is the laboratory momentum of the incident particle. Remembering that the total Hamiltonian in the entrance channel can be written in the form [28]

$$H = H_a + H_A + T_a + T_A + V_{aA} = H_a + H_A + T_{cm} + T_{aA} + (V_{aA} - V_{ab}) + V_{ab} , \quad (2.23)$$

where H_i and T_i are the internal Hamiltonian and the kinetic energy operator for particle i , V_{ij} is the interaction between particles i and j , T_{cm} is the total c.m. kinetic energy operator for the system and T_{ij} is the kinetic energy operator of the relative motion (corresponding to \vec{r}_{ij}).

Considering the interactions of the outgoing particles a' and b with the residual nucleus in addition to the interaction between a' and b for the exit channel, the Hamiltonian can be written as,

$$H = H_{a'} + H_b + H_B + T_{a'} + T_b + T_B + V_{a'b} + V_{bB} + V_{a'B} . \quad (2.24)$$

Passing from the coordinates $(\vec{r}_{a'}, \vec{r}_b, \vec{r}_B)$ to $(\vec{r}_{a'B}, \vec{r}_{bB}, \vec{R})$ and $(\vec{r}_{a'-bB}, \vec{r}_{bB}, \vec{R})$ and eliminating the c.m. kinetic energy, the Hamiltonian is re-expressed as,

$$H - V_{a'b} - T^{c.m.} = H_{a'} + H_b + H_B + T_{a'B} + T_{bB} + V_{a'B} + V_{bB} + T_{coup}. \quad (2.25)$$

$\vec{r}_{a'B}(\vec{r}_{bB})$ is the relative distance between $a'(b)$ and B , \vec{R} represents (overall) centre-of-mass position, and $\vec{r}_{a'-bB}$ is the distance between particle a' and the centre-of-mass of the $b - B$ system. $T_{coup} = -\hbar^2 \vec{\nabla}_{a'B} \cdot \vec{\nabla}_{bB} / m_B$ is a coupling operator which should have little effect, provided $m_B \ll \mu_{a'B}$ and/or $m_B \ll \mu_{bB}$.

If T_{coup} is neglected, the exit channel wave function factorises [28]

$$\eta_{Ba'b}^{(-)} = \chi_{a'B}^{(-)}(\vec{k}_{a'B}, \vec{r}_{a'B}) \chi_{bB}^{(-)}(\vec{k}_{bB}, \vec{r}_{bB}), \quad (2.26)$$

where the χ 's are solutions of the wave equations

$$(T_{a'B} + V_{a'B} - \varepsilon_{a'B}) \chi_{a'B}^{(-)}(\vec{k}_{a'B}, \vec{r}_{a'B}) = 0 \quad (2.27)$$

and

$$(T_{bB} + V_{bB} - \varepsilon_{bB}) \chi_{bB}^{(-)}(\vec{k}_{bB}, \vec{r}_{bB}) = 0. \quad (2.28)$$

The potentials $V_{a'B}$ and V_{bB} are taken to be optical potentials which describe the $a' + b$ and $b + B$ scattering at the relative energies $\varepsilon_{a'B}$ and ε_{bB} where,

$$\varepsilon_{a'B} = \frac{p_{a'B}^2}{2\mu_{a'B}}$$

and

$$\varepsilon_{bB} = \frac{p_{bB}^2}{2\mu_{bB}}$$

with,

$$\vec{p}_{a'B} = \hbar\vec{k}_{a'B} = \vec{p}_{a'} - \frac{m_{a'}}{m_{a'} + m_b + m_B}\vec{p}_a$$

and,

$$\vec{p}_{bB} = \hbar\vec{k}_{bB} = \vec{p}_b - \frac{m_b}{m_b + m_b + m_B}\vec{p}_a.$$

The bound wave function $\phi_{L\Lambda}^\alpha(\vec{r}_{bB})$ of b is found by introducing a phenomenological real Woods-Saxon potential V_{WS} which is adjusted to reproduce the empirical $A \rightarrow B + b$ separation energy S_{bB} [28]

$$(T_{bB} + V_{WS} - S_{bB})\phi_{L\Lambda}^\alpha(\vec{r}_{bB}) = 0, \quad (2.29)$$

where, $T_{bB} = \frac{\hbar^2}{2\mu_{bB}}\nabla_{bB}^2$ is the kinetic energy operator of the $b - B$ relative motion.

The principal quantum number N for the bound cluster wave function was chosen on the basis of conservation of harmonic oscillator shell model quanta in the transformation from independent-particle to cluster-model wave functions. Thus, for a given L of the cluster wave function [9]

$$2(N - 1) + L = \sum_{i=1}^{n_c} [2(n_i - 1) + l_i],$$

where n_c is the number of particles in the cluster. Note that the values n_i and l_i correspond to the filling of independent-particle shell model orbitals above the residual core.

Substituting $\eta_{Aa}^{(+)}$ and $\eta_{Ba'b}^{(-)}$ and integrating over \vec{r}_{ab} (zero-range approximation), Eq. (2.18) gives

$$T_{fi}^{\alpha L\Lambda} = \frac{1}{(2L+1)^{1/2}} \int \chi_{a'B}^{(-)*}(\vec{k}_{a'B}, \vec{r}) \chi_{bB}^{(-)*}(\vec{k}_{bB}, \vec{r}) \chi_{aA}^{(+)}(\vec{k}_{aA}, \gamma\vec{r}) \phi_{L\Lambda}^{\alpha}(\vec{r}) d\vec{r}, \quad (2.30)$$

where $\vec{r}_{a'B} = \vec{r}_{a'b} + \vec{r}_{bB}$, $\vec{r}_{aA} = \vec{r}_{ab} + \gamma\vec{r}_{bB}$ and $\gamma = B/(B+b)$.

χ 's are expressed as partial wave expansions in the form

$$\chi_{aA}^{(+)}(\vec{k}_{aA}, \gamma\vec{r}) = \frac{4\pi}{\gamma k_{aA} r} \sum_{l_a \lambda_a} u_{l_a}(k_{aA}, \gamma r) i^{l_a} Y_{l_a \lambda_a}^*(\hat{r}) Y_{l_a \lambda_a}(\hat{k}_{aA}), \quad (2.31)$$

$$\chi_{a'B}^{*(-)}(\vec{k}_{a'B}, \vec{r}) = \frac{4\pi}{k_{a'B} r} \sum_{l'_a \lambda'_a} u_{l'_a}(k_{a'B}, r) i^{-l'_a} Y_{l'_a \lambda'_a}(\hat{r}) Y_{l'_a \lambda'_a}^*(\hat{k}_{a'B}), \quad (2.32)$$

$$\chi_{bB}^{*(-)}(\vec{k}_{bB}, \vec{r}) = \frac{4\pi}{k_{bB} r} \sum_{l_b \lambda_b} u_{l_b}(k_{bB}, r) i^{-l_b} Y_{l_b \lambda_b}(\hat{r}) Y_{l_b \lambda_b}^*(\hat{k}_{bB}), \quad (2.33)$$

and the solution of Eq. (2.29), the bound state cluster wave function is written as [28]

$$\phi_{L\Lambda}^{\alpha}(\vec{r}) = R_{\alpha L}(r) i^L Y_{L\Lambda}(\vec{r}). \quad (2.34)$$

Choosing the z -axis along \vec{k}_{aA} and y -axis along $\vec{k}_{aA} \times \vec{k}_{a'B}$ ($\hat{k}_{aA} = (0, 0)$, $\hat{k}_{a'B} = (\theta_a, 0)$ and $\hat{k}_{bB} = (\theta_b, \phi_b)$), a final expression for $T_{fi}^{\alpha L\Lambda}$ is obtained as

$$T_{fi}^{\alpha L\Lambda} = \frac{\sqrt{4\pi}}{\gamma k_{aA} k_{aB} k_{bB}} \sum_{l_a l_{a'} l_b \lambda_b k_b} i^{l_a + L - l_{a'} - l_b} \frac{(2l_a + 1)(2l_{a'} + 1)(2l_b + 1)}{(2k + 1)} (l_b \lambda_b L \Lambda | k q) \\ \times (l_b 0 L 0 | k 0) (l_a 0 l_{a'} q | k q) (l_a 0 l_{a'} | k 0) I_{l_a l_{a'} l_b}^L d_{q0}^{l_{a'}}(\theta_a) d_{\lambda_b 0}^{l_b}(\theta_b) e^{-i\lambda_b \phi_b}, \quad (2.35)$$

where $d_{mn}^l(\theta)$ are reduced rotation matrices, $(l_1\lambda_1l_2\lambda_2|l_3\lambda_3)$ is a Glebsch-Gordan coefficient and the radial integral

$$I_{l_a l_{a'} l_b}^L = \int_0^\infty u_{l_a}(k_{aA}, \gamma r) u_{l_{a'}}(k_{a'B}, r) u_{l_b}(k_{bB}, r) R_{\alpha L}(r) dr / r .$$

The incoming and outgoing distorted-waves, defined above, were found by omitting the spin-orbit terms in the optical potentials which generate them. As a result, simplification of the spin summations lead to the appearance of the two-body cross section as a multiplicative factor. If they are included and the incident beam is polarized, distorted-waves $\chi^{(\pm)}$ become matrices in spin space $\chi_{\sigma\rho}^{(\pm)}$ and cross section calculations become more complex. The differential cross section is given by [35]

$$\frac{d^3\sigma}{d\Omega_{a'} d\Omega_b dE_{a'}} = K'_F C^2 S \sum_{\substack{\rho_a \rho_{a'} \rho_b'' \\ JM}} \frac{|\langle \rho_{a'} \rho_b'' | T | \rho_a JM \rangle D_{\rho_a \rho_{a'}}^{1/2}(R_{ap})|^2}{(2J+1)}, \quad (2.36)$$

where

$$\begin{aligned} \langle \rho_{a'} \rho_b'' | T | \rho_a JM \rangle D_{\rho_a \rho_{a'}}^{1/2}(R_{ap}) &= \sum_{\substack{\rho_a \sigma_a \sigma_{a'} \sigma_{a'}' \\ \sigma_b'' \sigma_b \sigma_b' \Lambda}} (2L+1)^{1/2} (L\Lambda s_b \sigma_b | JM) \\ &\times D_{\rho_a \rho_{a'}}^{1/2}(R_{ap}) \times D_{\sigma_{a'} \sigma_{a'}'}^{1/2*}(R_{aa'}) \times D_{\sigma_b \sigma_b''}^{1/2*}(R_{ab}) \times T^{L\Lambda} \\ &\quad \begin{matrix} \sigma_a \sigma_{a'} \sigma_b'' \\ \rho_a \rho_{a'} \rho_b'' \end{matrix} \langle \sigma_{a'} \sigma_b | t | \sigma_a \sigma_b \rangle, \quad (2.37) \end{aligned}$$

where $D_{mn}^{1/2}(R)$ are rotation matrices which describe the transformation of spin projections from n to m through a rotation R_{ai} into sets of axes in which are, respectively, defined the

incident particle polarization axis and the directions of propagation for particles a' and b . T is the transition operator and t is the two-body operator for the free $a - b$ scattering process. C^2S is the spectroscopic factor for the final state in B , K_F is the kinematic factor, L is the relative angular momentum (projection Λ) of b and B , J is the angular momentum (projection M) of the target and S_i are the spins with projections ρ_i and σ_i for particles i ; the primes indicate quantities which are expressed with respect to different sets of axes.

The quantity $T^{L\Lambda}$ is defined by [35]

$$T_{\sigma_a \sigma_{a'} \sigma_b''}^{L\Lambda} = (2L + 1)^{-1/2} \int \chi_{\sigma_{a'} \rho_{a'}}^{(-)*}(\vec{r}') \chi_{\sigma_b'' \rho_b''}^{(-)*}(\vec{r}'') \phi_{L\Lambda}(\vec{r}) \chi_{\sigma_a \rho_a}^{(+)}(\gamma \vec{r}) d\vec{r}, \quad (2.38)$$

where the χ_{ij} are distorted-waves, ϕ is the spatial part of the bound-state wave function of particle b , and $\gamma = B/A$.

2.5 Calculations with the Computer Code THREE-DEE

THREEDDEE code is a computer program written by Chant [36] to calculate DWIA cross sections and polarization observables.

Equations (2.36) and (2.19) for when the spin-orbit effects are and are not taken into account respectively, were employed for the cross section calculations.

The following subsections discuss the various quantities which were used by THREEDDEE to obtain the final results.

2.5.1 The two-body scattering amplitude

The two-body scattering amplitude that appeared in Eqs. (2.19) and (2.36) is off-shell. In general this quantity is taken to be an on-shell amplitude although some nuclear reactions are sensitive to the off-shell effects. Roos *et al.* [1] investigated the importance of off-energy

shell effects by calculating the half-shell p - α cross section for various α -particle binding energies using optical model potentials from an analysis of 85 MeV p - α elastic scattering and claimed that with the exception of the region near the minimum, the off-shell effects are quite small.

The on-shell amplitude is determined by using two different prescriptions for the effective energy E at which this approximation is made : final energy prescription (FEP) and initial energy prescription (IEP).

In the FEP E is taken to be the relative centre-of-mass energy of the emitted particles in the exit channel, while in the IEP, E is the relative centre-of-mass energy of the incident and struck particles in the entrance channel.

The effective energies calculated in the two prescriptions IEP and FEP are respectively given by [37] :

$$E_{IEP} = E_a + \sqrt{p_b^2 + m_b^2}$$

and

$$E_{FEP} = \sqrt{m_{a'}^2 + m_b^2 + 2E_{a'}E_b - 2p_{a'}p_b \cos \theta} ,$$

where E_i , p_i and m_i are respectively, the energy, the momentum and the rest mass of particle i while θ is the angle between the two outgoing particles.

2.5.2 The bound state wave function

The general form of the potential used to generate the bound-state consists of a central potential term, a spin-orbit term and a Coulomb term [36] :

$$U(r) = -\frac{V_0}{1 + e^x} - \left(\frac{\hbar}{m_\pi c} \right)^2 \vec{l} \cdot \vec{\sigma} \frac{V_{so} e^{x_s}}{r a_{so} (1 + e^{x_s})^2} + U_{bB}^{coul}(r) , \quad (2.39)$$

where $x = (r - r_0 A^{1/3})/a_0$, $x_s = (r - r_{so} A^{1/3})/a_{so}$, and $U_{bB}^{coul}(r)$ is the Coulomb potential produced by a uniform sphere of charge with radius $R_c = r_c A^{1/3}$,

$$U_{bB}^{coul}(r) = Z_b Z_B e^2 \times \begin{cases} \frac{1}{r} & r \geq R_c \\ \frac{1}{2R_c} \left(3 - \frac{r^2}{R_c^2}\right) & r < R_c \end{cases}, \quad (2.40)$$

- V_0 is the strength of the central potential,
- V_{so} is the strength of the spin-orbit potential,
- r_0 is the radius parameter of the central potential,
- r_{so} is the radius parameter of the spin-orbit potential,
- a_0 is the diffuseness parameter of the central potential,
- a_{so} is the diffuseness parameter of the spin-orbit potential,
- A is the atomic mass of the recoil nucleus,
- $(\hbar/m_\pi c)^2 = 2fm^2$ is the pion Compton wavelength factor,
- $\vec{l} \cdot \vec{\sigma} = l$ or $-(l+1)$ for $j = l \pm 1/2$ with \vec{l} the orbital angular momentum of the relative motion of scattered particle and nucleus and $\vec{\sigma}$ the operator defined in terms of the spin angular momentum \vec{s} .

- $\vec{s} = (\hbar/2)\vec{\sigma}$ for neutrons, protons, 3He and 3H ,
- $\vec{s} = 1\hbar\vec{\sigma}$ for 2H , and
- $\vec{s} = 0$ for α particles.

2.5.3 The distorted-wave functions

Distorted-wave functions are generated by solving the Schrödinger equation with a complex optical potential. The real part of the potential describes the average potential energy of the incident nucleon inside the nucleus potential and the imaginary part describes absorption effects.

The total optical potential used includes a Coulomb potential, a complex central potential term, a complex spin-orbit term and a complex exchange term and is given by [36]

$$U(r) = U(r)_{central} - \left(\frac{\hbar}{m_{\pi}c} \right)^2 \frac{\vec{l} \cdot \vec{\sigma} (V_{so} + iW_{so})e^{x_s}}{ra_{so} (1 + e^{x_s})^2} - (-)^l \frac{V_{ex}}{1 + e^{x_{ex}}}, \quad (2.41)$$

with

$$x_s = \frac{r - r_{so}A^{1/3}}{a_{so}}$$

and

$$x_{ex} = \frac{r - r_{ex}A^{1/3}}{a_{ex}},$$

where,

- V_{so} is the strength of the real part of the spin-orbit potential,
- W_{so} is the strength of the imaginary part of the spin-orbit potential,
- V_{ex} is the strength of the exchange potential,
- r_{so} is the radius parameter of the spin-orbit potential,
- r_{ex} is the radius parameter of the exchange potential,
- a_{so} is the spin-orbit diffuseness parameter,
- a_{ex} is the diffuseness parameter of the exchange potential and the remaining parameters are defined as above.

$U_{central}$ is the central optical potential given by [36]

$$U(r)_{central} = -\frac{V_0}{1 + e^x} - \frac{iW_V}{1 + e^{x'}} - \frac{4iW_S e^{x'}}{(1 + e^{x'})^2} + U_{coul}^{ij}, \quad (2.42)$$

with

$$x = \frac{r - r_R A^{1/3}}{a_R}$$

and

$$x' = \frac{r - r_I A^{1/3}}{a_I}$$

where,

- V_0 is the strength of the real part of the central potential,
- W_V is the strength of the volume part of the central potential,
- W_S is the strength of the surface absorptive part of the potential,
- r_R is the radius parameter of the real part of the central potential,
- r_I is the radius parameter of the imaginary part of the central potential,
- a_R is the real central potential diffuseness parameter,
- a_I is the imaginary central potential diffuseness parameter,
- A is the atomic number of the recoil nucleus and
- $U_{coul}^{ij}(r)$ is the Coulomb potential due to a sphere of radius $R_{coul} A_T^{1/3}$ as mentioned before, provided the subscripts i and j are taken to refer to the interacting particles. A_T is the mass in a.m.u. of the target nucleus A or the residual nucleus B as selected.

2.6 Analyzing Power

The analyzing power is the effect on the differential cross section of having the incident particle polarized. It may be also regarded as a measure of the effect on scattering cross sections of changes in the polarization of the beam or the target nuclei. The polarization is used to mean the non-random orientation of nuclear spins [38].

The analyzing power is calculated in THREEDEE by making use of the following expression

$$A_y = \frac{\sigma^\uparrow - \sigma^\downarrow}{\sigma^\uparrow + \sigma^\downarrow}, \quad (2.43)$$

where $\sigma^{\uparrow(\downarrow)} \equiv \left[\frac{d^3\sigma}{d\Omega_{a'} d\Omega_b dE_{a'}} \right]^{\uparrow(\downarrow)}$ given by Eq. (2.36), representing here the triple differential cross section for an incident beam of spin-up (spin-down) polarized particles, as calculated with THREEDEE.

Chapter 3

Experimental Details

3.1 Overview

This chapter contains a description of the experimental setup, the data acquisition and the experimental procedure. In this experiment a ^{12}C target was bombarded with a proton beam of 100 MeV incident energy while the scattered protons and alpha particles were detected in coincidence with two detector telescopes, mounted coplanar on opposite sides of the beam. The standard ΔE - E method was used to identify the various charged particles that were detected.

The next section presents the accelerator facility at iThemba LABS followed by sections which describe the polarimeters used to measure the beam polarization, the scattering chamber, the targets, the detector telescopes used during the experiment and the electronics required for signal processing.

Finally, Section 3.9 discusses the hardware and software used for data acquisition, and the last section describes the procedure followed for conducting the experiment successfully.

3.2 The Facility

The experiment was performed at the separated sector cyclotron facility of iThemba Laboratory for Accelerator based Sciences (LABS), Faure, South Africa. iThemba LABS is a

multidisciplinary facility which provides particle beams used in radioisotope production, proton and neutron therapy and basic research. The layout of the facility is shown in Fig. 3.1. A polarized ion source (PIS) fed with hydrogen gas provides a proton rich plasma. Protons from this source are accelerated by a solid pole injector (SPC2) to an energy of about 4.5 MeV and after being injected into the separated sector cyclotron (SSC) they are accelerated to the desired energy of 100 MeV. The beam was transferred via the X and P beam-lines in order to be directed to the scattering chamber in experimental vault A (represented by a circle to the right side of the SSC in Fig. 3.1). The proton beam from the PIS was polarized in a plane normal to the scattering plane, with the polarization direction flipped every 10 seconds.

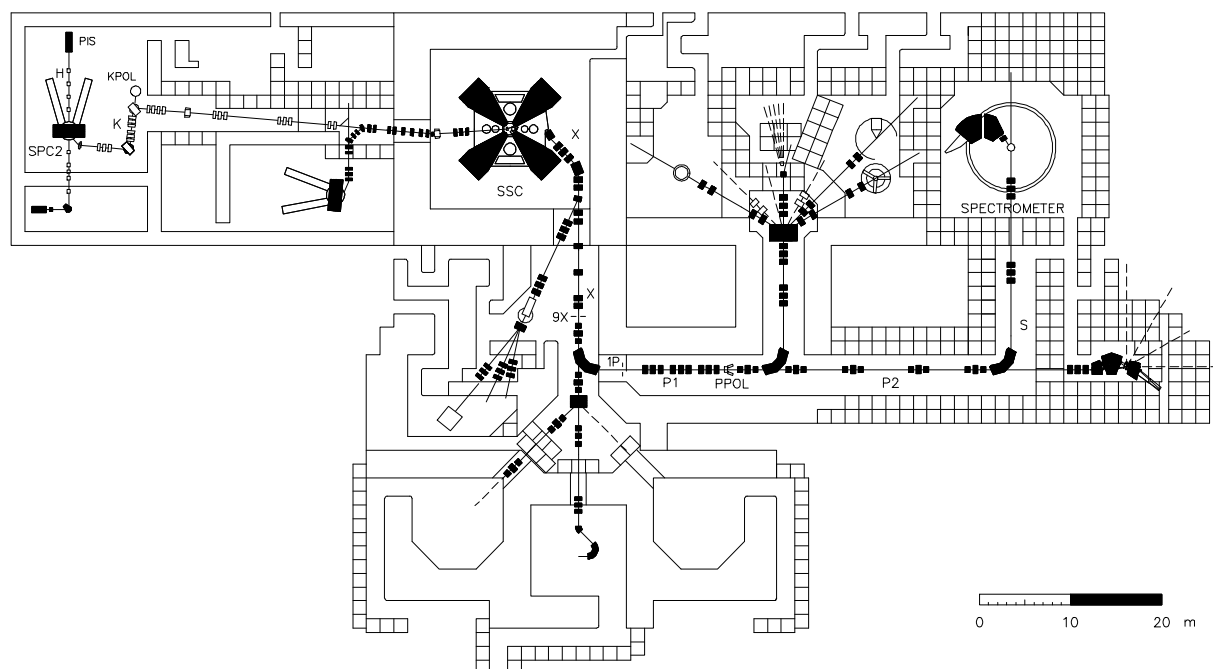
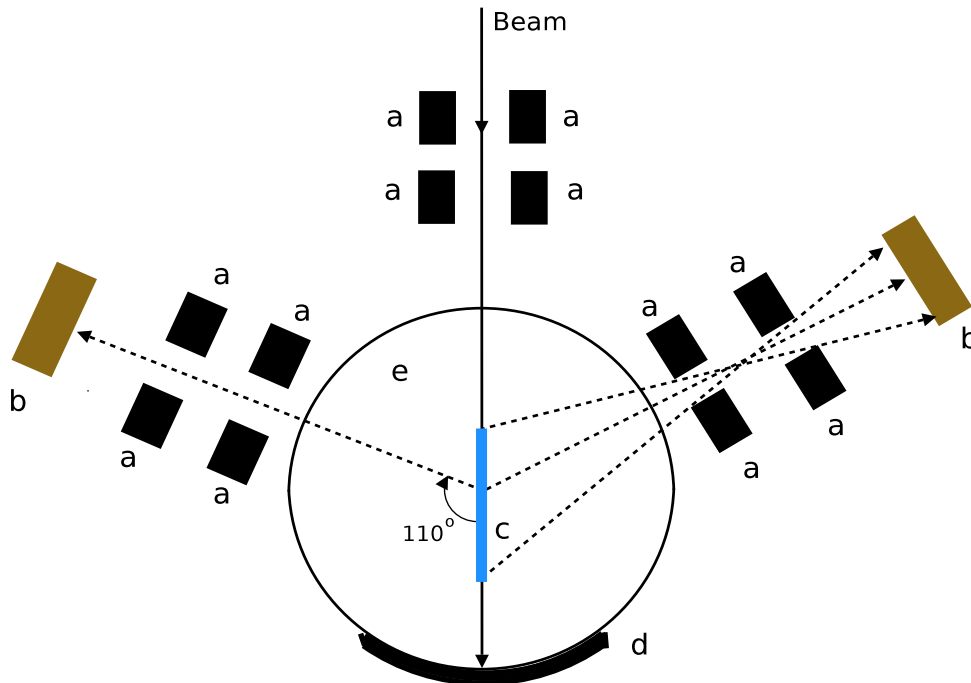


Figure 3.1. A layout of the experimental facilities at *iThemba LABS*.

3.3 Polarimeters

Two types of polarimeters were used during the experiment to measure the beam polarization. These include a low-energy polarimeter used by the beam operators to optimize the degree of polarization prior to the experiment, and a high-energy polarimeter to periodically determine the beam polarization during experimental runs.

3.3.1 K-line polarimeter



a = Ta collimators, b = 150 μm Si detector, c = Effective target area, d = Beam stop and current integrator, e = ^4He gas.

Figure 3.2. *Experimental layout of the K-line polarimeter.*

The low-energy polarimeter, referred to as KPOL in Fig. 3.1, was set up in the K-line between the injector cyclotron (SPC2) and the main cyclotron (SSC). The polarimeter consisted of two 150 μm Silicon (Si) surface-barrier detectors, a He gas target operated at about 1 bar, two sets of passive tantalum collimators to collimate the proton beam onto the target and two sets of additional tantalum collimator slits in front of each detector which defined the effective gas target area [34]. The gas cell target contained a high-purity He gas with entrance and exit windows of 6 μm Havar. The two Si-detectors are positioned at $\theta_{lab} = 110^\circ$ with respect to the beam direction.

The 100 MeV proton beam delivered by the SSC for this experiment corresponds to an energy of 4.551 MeV produced in the SPC2. The energy loss in the 6 μm Havar of the 4.551 MeV proton beam incident on the He-target results in 4.308 MeV effective proton incident energy. The analyzing power for the scattering of 4.308 MeV protons off ^4He at $\theta_{cm} = 123.7^\circ$ ($\theta_{lab} = 110^\circ$) is known to be 0.942 [39]. Figure 3.2 shows the layout of the

low-energy polarimeter which was used for measuring polarization in the K-line.

3.3.2 P-line polarimeter

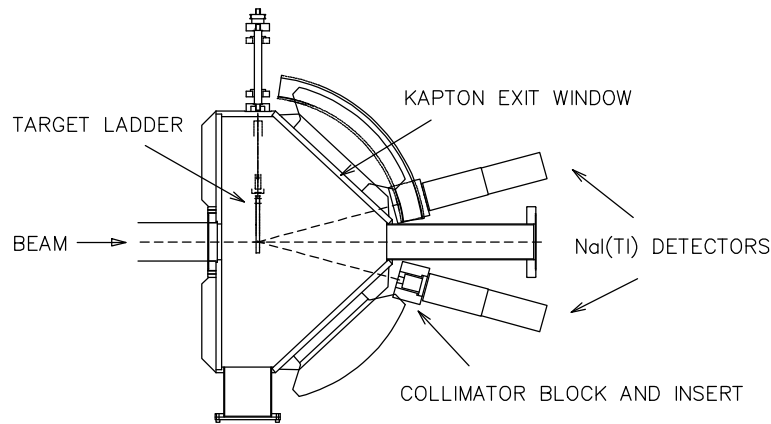


Figure 3.3. *Experimental layout of the P-line polarimeter.*

The high-energy polarimeter, referred to as PPOL in Fig. 3.1, was set up in the P-line, the high-energy beam line leading from the SSC to various vaults. The P-line polarimeter consisted of a $75 \mu\text{m}$ thick $(\text{CH}_2)_n$ foil mounted on the target ladder that can be driven into the P-line chamber (Fig 3.3). Two NaI(Tl) detectors, collimated with 5 cm thick brass collimator blocks and appropriate inserts, are positioned at $\theta_{lab} = 40^\circ$ on opposite sides of the beam direction. Both detectors are separated from the scattering chamber vacuum by Kapton exit windows. The analyzing power of 0.74 of the $^{12}\text{C}(p, p)$ elastic scattering reaction at 100 MeV ($\theta_{lab} = 40^\circ$) [40], measured experimentally at iThemba LABS during the 1999 (p, α) experiment, was used to determine the beam polarization (discussed in Section 4.8).

3.4 Scattering Chamber

The scattering chamber measures 1.5 m in diameter and 0.76 m in height. It contained a target ladder on which 5 different targets were mounted. Any one of these targets could be selected by changing the vertical position of the target ladder. The target ladder can also be rotated around its vertical axis in order to change the target angle with respect to the

incident beam. The chamber is also equipped with two movable arms which can support a variety of complex detector systems and which can be remotely positioned within certain angular ranges with respect to the beam direction. All movable components (target ladder and detector arms) of the scattering chamber can be remotely positioned according to digital readouts from the data room.

Different ports of the scattering chamber, equipped with BNC feedthroughs, were used for high voltage (HV) power supply, 50 Ω and 93 Ω cables. The 50 Ω and 93 Ω cables were used for logic signals (timing signals) and linear signals, respectively. All cables used were connected to a patch panel situated inside the vault which is linked to a similar patch panel in the data room.

The incident beam strikes the target on the target ladder at the centre of the chamber and is stopped 6 meters from the exit of the scattering chamber by a heavily shielded beam stop that measures the total amount of charge deposited.

One of the ports situated just above the beam entrance is used to monitor the beam spot produced by a scintillating ruby target, by means of a closed circuit television camera, while the beam is focussed by the operators. The vault was kept in darkness during operation to minimize light entering the chamber and affecting the Si detectors.

The scattering chamber was kept at a pressure of about 10^{-5} mbar during the experiment. This vacuum was obtained by pumping down the chamber in the following three stages: First the valve between the scattering chamber and the rotary and turbo-molecular pumps was opened. A pressure of 1 mbar was obtained with the rotary pump followed by the turbo-molecular pump to lower the pressure to 10^{-3} mbar. At this pressure the valve to the cryogenic pump could be opened. This pump can remove remaining molecules inside the chamber by trapping these on a cold surface at 12 K. Note that the valve of the first stage was opened slowly to protect the detectors and targets against any possible damage.

3.5 Targets

The targets were mounted perpendicular to the proton beam inside the scattering chamber on the target ladder which can hold five different targets. Two carbon targets, the ruby

crystal (Al_2O_3), a $(\text{CH}_2)_n$ polythene plastic foil and an empty frame. The two ^{12}C targets of 1.1 mg/cm^2 and 2.2 mg/cm^2 thicknesses were used for data acquisition. The experiment was planned to use a thin target as in the earlier work from Roos *et al* [1], but due to beam intensity limitations we decided to use a thicker one without compromising the energy resolution. A $(\text{CH}_2)_n$ polythene plastic foil was used for calibration purposes (discussed in Subsection 4.2.2) and for fine-tuning the electronics which is described in Section 3.10.

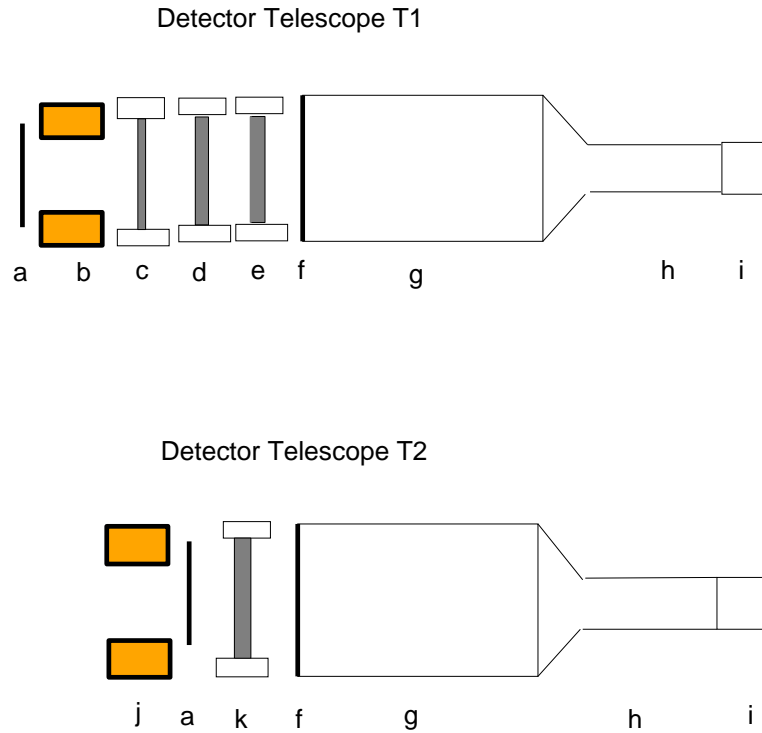
The beam was aligned and adjusted with the aid of the ruby crystal target. The ruby target has a 3 mm diameter hole in the centre. This helps the operators to focus the beam. In the case where the beam collides with the ruby around the hole, visible light is produced. This light is then observed with a closed circuit television camera in the cyclotron control room allowing the beam to be adjusted.

The empty frame in the target ladder was employed to check the beam halo which comprises mainly secondary particles originating from the scattering of the beam off beam-line components. This enabled us to define the beam of sufficient quality, i.e. the count rate with the empty target amounted to less than 5-7% of the value obtained with the ^{12}C target. The targets were remotely positioned in the incident proton beam direction by selecting and changing the vertical position of the ladder. Whenever an angle pair corresponding to a larger angle ($|\theta| > 65^\circ$) of one telescope was selected, the target ladder was rotated slightly towards the second telescope in order to prevent the target frame from obscuring the line of flight of particles from the centre of the target to the detector (see Table 3.2).

3.6 Detector Telescopes

The two detector telescopes used in the coincidence measurements were conventional 3- and 2-element charged-particle telescopes and were mounted coplanar on opposite sides of the incident beam. These detector telescopes are illustrated in Fig. 3.4.

The first telescope, labelled T1, used primarily for alpha-particle detection consisted of a $100 \mu\text{m}$ Silicon (Si) surface-barrier ΔE detector, followed by two 2 mm Silicon (Si) surface-barrier E detectors. A $76 \text{ mm} \times 51 \text{ mm}$ NaI(Tl) was mounted behind the Si detectors to



a = $8 \mu\text{m}$ Kapton foil, b = 48.10 mm thick brass collimator, c = $100 \mu\text{m}$ thick Si detector, d, e = 2 mm thick Si detector, f = $7 \mu\text{m}$ Havar entrance foil, g = $76 \text{ mm} \times 51 \text{ mm}$ NaI(Tl) crystal, h = Photomultiplier tube, i = Phototube base, j = 42.0 mm thick brass collimator, k = $1022 \mu\text{m}$ thick Si detector.

Figure 3.4. Particle detector telescopes T1 and T2

veto energetic protons.

The second ΔE - E telescope, labelled T2, was primarily applied for proton particle detection and consisted of a $1022 \mu\text{m}$ Silicon (Si) surface-barrier ΔE detector followed by a $76 \text{ mm} \times 51 \text{ mm}$ stopping NaI(Tl) scintillation E detector.

The purpose of the detector telescopes was firstly, to identify particles emitted from the target nucleus, and secondly, to accurately measure the energy of the emitted particles of interest.

In telescope T1, the two forward Si detectors were mounted so that their entrance gold surfaces faced one another. This was done to minimize the dead layer between the Si detectors, and thus improve the particle identification resolution of low-energy alpha particles.

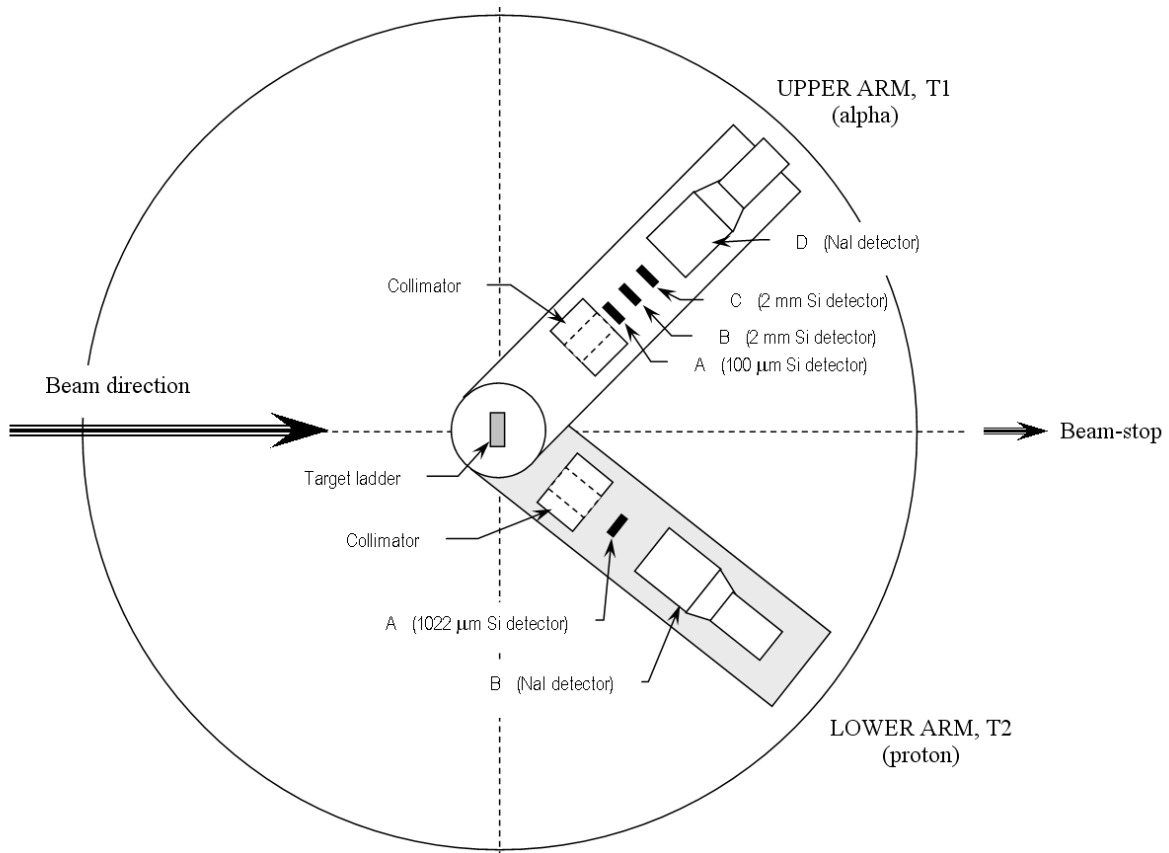


Figure 3.5. *Scattering chamber setup*

The Si ΔE detector thicknesses were selected with the aim of obtaining sufficient separation in the energy deposited by various charged particles scattered from the reaction. A thicker Si detector will enhance energy separation of emitted particles while at the same time will increase the minimum detectable energy at which particle identification is possible. The Si detectors have also the ability to operate at room temperature without excessive leakage current and thin dead layers. The basic characteristic of NaI(Tl) detectors, however, shows different responses to various charged particles, which is essentially the efficiency for converting ionization energy to photons. The light output is then different for different charged particles. Si detectors were chosen in T1 because of their better energy resolution. We intended to resolve the ground state from the first excited state of ^8Be .

The solid brass collimators needed to be thick enough so that energetic protons or alpha particles cannot pass through. In telescope T1, a solid brass collimator was mounted immediately in front of the first Si detector. The brass insert of this collimator was fitted

Detector Telescope	Distance between the target centre and the rear hole of collimator (mm)	Diameter of collimator slit (mm)	Solid angle (msr)
T1	342.5 ± 1.0	14.01 ± 0.02	1.31 ± 0.01
T2	229.7 ± 1.0	18.80 ± 0.02	5.26 ± 0.05

Table 3.1. *Detector geometry parameters*

with a 2 mm Tantalum (Ta) disc with circular aperture which defined the solid angle subtended by T1. The Tantalum disc was chosen to reduce chances of alpha particles to undergo slit scattering. In telescope T2 a solid brass collimator was mounted in front of the Si detector. The brass collimator insert had a 20 mm circular aperture used to define the solid angle of T2.

The solid angle $\Delta\Omega$ was calculated as follows:

$$\Delta\Omega = \frac{\pi r^2}{D^2}, \quad (3.1)$$

where r is the radius of the collimator opening and D is the distance from the target centre to the back of the collimator. The subtended solid angles were 1.31 ± 0.01 msr for telescope T1 and 5.26 ± 0.05 msr for telescope T2. The respective geometry parameters are listed in Table 3.1.

Kapton foils with a thickness of 8 μm were placed over the front and the rear hole of the brass collimators of T1 and T2, respectively, to decrease the flux of low energy electrons, emitted from the target, reaching the front detectors of the telescopes. Teflon frames were mounted behind the brass collimator on each telescope arm to house different Si detectors.

The NaI thickness of 51 mm was able to stop 100 MeV protons, as the range of 100 MeV protons in NaI is only 35.76 mm.

The NaI(Tl) detector consists of a 7 μm thick Havar entrance window which protects the NaI crystal cylinder against moisture and is viewed by a photomultiplier tube which is exposed to possible gain drifts (discussed in Section 4.5.1). In order to monitor possible gain drifts a light-emitting diode (LED) is embedded into the crystal. Light coming from

the LED when triggered at a constant rate is collected by the photomultiplier, a variation in the position of the pulser peak in the measured spectrum indicates gain drifts of the photomultiplier tube.

At a pressure of 10^{-4} mbar and lower the detectors could be biased. The bias supply was fed directly (via HV cables) to the photomultiplier bases of the NaI(Tl) detectors, while the Si detectors were biased via the SHV-input of the charge-sensitive preamplifiers. The NaI(Tl) detectors required an operating bias of +800 V while the Si detectors were operated at +30 V (100 μ m Si), +330 V (1mm Si) and +350 V (2mm Si). The depletion depth of a semiconductor detector is determined by its bias voltage. Bias voltages on the Si detectors were applied slowly to allow the detectors to settle and stabilize. Radiation damage of the semiconductors can lead to an increase in the leakage current as well as a deterioration in energy resolution. This was monitored by regularly recording and keeping the count rates of the detectors below 10^4 Hz. In the case of any increase of the leakage current in the detector, the operating voltage was increased.

3.7 Telescope positions

The two detector telescopes were positioned at quasifree angles where the residual undetected nucleus in the coincidence measurement is left with zero or small recoil momentum ($|p| \lesssim 11$ MeV/c). This was done using a computer program *KINMAT* available at iThemba LABS. This program is used to approximate the three-particle knockout reaction at zero recoil momentum by taking the Q -value of the knockout reaction into account. For the $^{12}\text{C}(p, p\alpha)^8\text{Be}$ reaction the Q -value is -7.37 MeV which is calculated as follows:

$$Q = 931.5 \times (M_A - (M_b + M_B)) ; \quad (3.2)$$

where 931.5 represents the energy mass equivalence of the proton and M_A , M_b and M_B are respectively the masses of the target nucleus, knocked out particle and residual nucleus. This value is less than zero because of the threshold energy of the reaction, part of the incident energy is needed to remove an alpha-particle from the target nucleus. The 10

Angle pair (θ_p, θ_α)	Target angle
(25°, -68.8°)	340°
(30°, -66.6°)	340°
(37°, -63.1°)	0°
(52°, -55.1°)	0°
(60°, -50.9°)	0°
(70°, -45.6°)	10°
(80°, -40.5°)	20°
(90°, -35.7°)	30°
(100°, -31.0°)	40°
(110°, -26.6°)	40°

Table 3.2. Angle pairs (θ_p, θ_α) and the corresponding target angles. θ_p and θ_α represent the proton and alpha angles, respectively.

different angle pairs chosen for the coincidence measurements and the corresponding target angles are listed in Table 3.2.

3.8 Electronics

3.8.1 Preamplifiers

The basic function of the preamplifiers is to amplify small signals from the detectors and to drive these through the cables that connect the preamplifier with the electronic setup. Charge-sensitive preamplifiers produce fast timing and slow linear signals. As timing and linear signals carry very different information, they have to be treated separately. In order to reduce noise pick-up, the preamplifiers were placed in the scattering chamber as close as possible to the detectors. Details related to the various preamplifiers are summarized in Table 3.3.

Test pulser signals were fed to the test-input of the preamplifiers of the Si detectors via 93 Ω cables, while in the case of the NaI(Tl) detectors, the pulser signals were fed via 50 Ω cables directly to the LED's embedded in the NaI crystals of the detectors (see Subsection 3.8.5).

The output of the scintillation preamplifiers of the NaI(Tl) detector was used for timing

Detector				Preamplifier	
	Type	Dimension	Model	Type	Model
T1A	Si surface-barrier	100 μm	ORTEC	Charge-sensitive	B-type
T1B	Si surface-barrier	2 mm	ORTEC	Charge-sensitive	CANBERRA
T1C	Si surface-barrier	2 mm	ORTEC	Charge-sensitive	CANBERRA
T1D	NaI(Tl)	76 mm \times 51 mm	BICRON	Scintillation	ORTEC 113
T2A	Si surface-barrier	1022 μm	ORTEC	Charge-sensitive	A-type
T2B	NaI(Tl)	76 mm \times 51 mm	BICRON	Scintillation	ORTEC 113

Table 3.3. *Detectors and preamplifiers*

Module	Model
Timing Filter Amplifier (TFA)	ORTEC 474
Constant Fraction Discriminator (CFD)	ORTEC 934
4-Fold Logic unit	LeCroy 365AL
Quad Discriminator	LeCroy 821
Time-to-Analog Converter (TAC)	ORTEC 567
Timing Single Channel Analyzer (TSCA)	ORTEC 551
Timer	ORTEC 719
Tail Pulse Generator (TPG)	BNC BH-1

Table 3.4. *NIM modules used to process timing signals.*

and logic signals.

3.8.2 Timing signals

The fast output signals from the preamplifiers of the Si detectors were fed into separate timing filter amplifiers (TFA's), each followed by a constant fraction discriminator (CFD) which produced fast logic pulses with a fixed shape in order to carry the only two possible logic states (0 or 1). A block diagram of the timing electronics used during the experiment is shown in Fig. 3.6. A summary of the various NIM modules used to process the timing signals is given in Table 3.4.

The first requirement for the detection of an event of interest in a particular telescope was the generation of the signal logic in coincidence between the ΔE and E detectors of telescopes T1 and T2 with no veto signal in the case of telescope T1. The signals from the

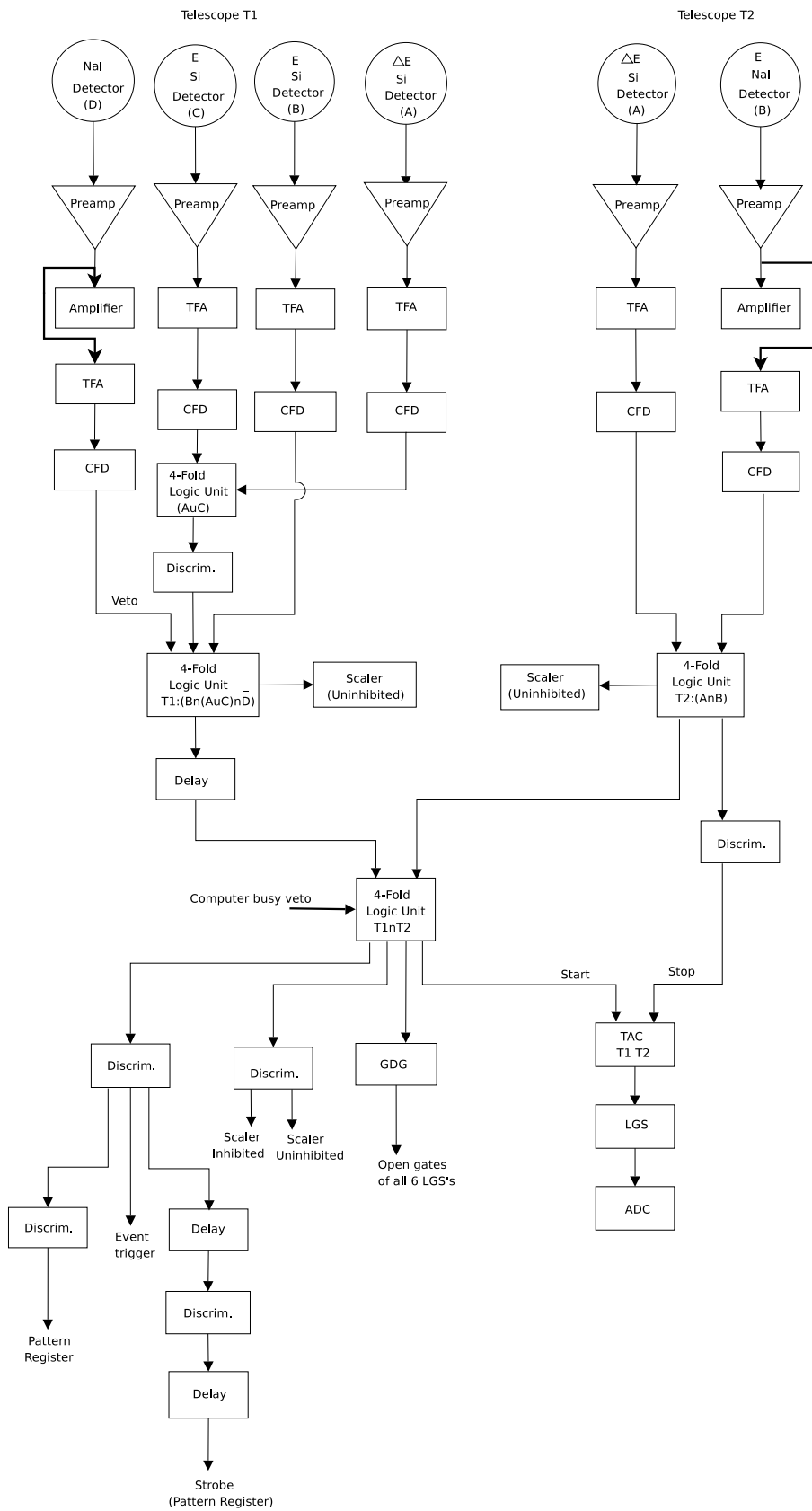


Figure 3.6. A block diagram of the timing electronics for telescopes T1 and T2.

CFD were delayed in order to synchronize the timing of the signals respectively from two elements (ΔE and E detectors for T2) and from three elements (ΔE , E and NaI detectors for T1). A valid event of telescope T1 is denoted by $[(A \cap B) \cup (B \cap C)] \cap \bar{D}$ with A, B, C and D representing signals from detectors T1A, T1B, T1C and T1D, respectively. A telescope T2 event, is denoted by $A \cap B$ with A and B signals coming from detectors T2A and T2B, respectively. It should be pointed out that, for the three smallest proton angles where the alpha particles of interest were stopped in the ΔE detector of T1, the hardware coincidence requirement for telescope T1 was turned off in the 4-fold logic unit. The valid event for telescope T1 was then merely generated by element T1A. All these logic operations, ANDing function for T2, OR and vetoing functions for T1, were performed by 4-fold logic units.

The second requirement for an acceptable event was a coincidence between an event in telescope T1 and telescope T2. This operation was performed by a 4-fold logic unit. The logic outputs from this 4-fold logic unit were fed to discriminators and to gate and delay generators (GDG). The outputs from the discriminators were fed to the pattern register to distinguish among others between data originating from telescope T1 and telescope T2, respectively. $T1 \cap T2$ coincidences were also used as the event trigger and to strobe the pattern register (see Subsections 3.8.7 and 3.8.9). Also, the outputs from the same 4-fold logic unit were fed to another discriminator which was used to increment the inhibited and uninhibited scalers as described in Subsection 3.8.10. The output signals from the 4-fold logic unit $T1 \cap T2$, fed to the GDG, were used as inputs to gate the linear signals.

The timing spectrum of $T1 \cap T2$ coincidences was measured by a time-to-amplitude converter (TAC). The $T1 \cap T2$ and telescope T2 event signals were used as the start and stop signals of the TAC, respectively. In the timing spectrum different peaks were observed. These peaks refer to different types of coincidences, notably prompt and delayed coincidences. Prompt coincidences contain real and accidental events, whereas delayed coincidences are purely accidental events. Furthermore, accidental coincidences mainly originate from two different beam packets.

The analog output signals from the TAC was fed via LGS modules to an ADC which passed the coincidence time information on for computer processing. Event trigger, scalers and Pattern register are described in Subsections 3.8.7, 3.8.10 and 3.8.9, respectively.

3.8.3 Linear signals

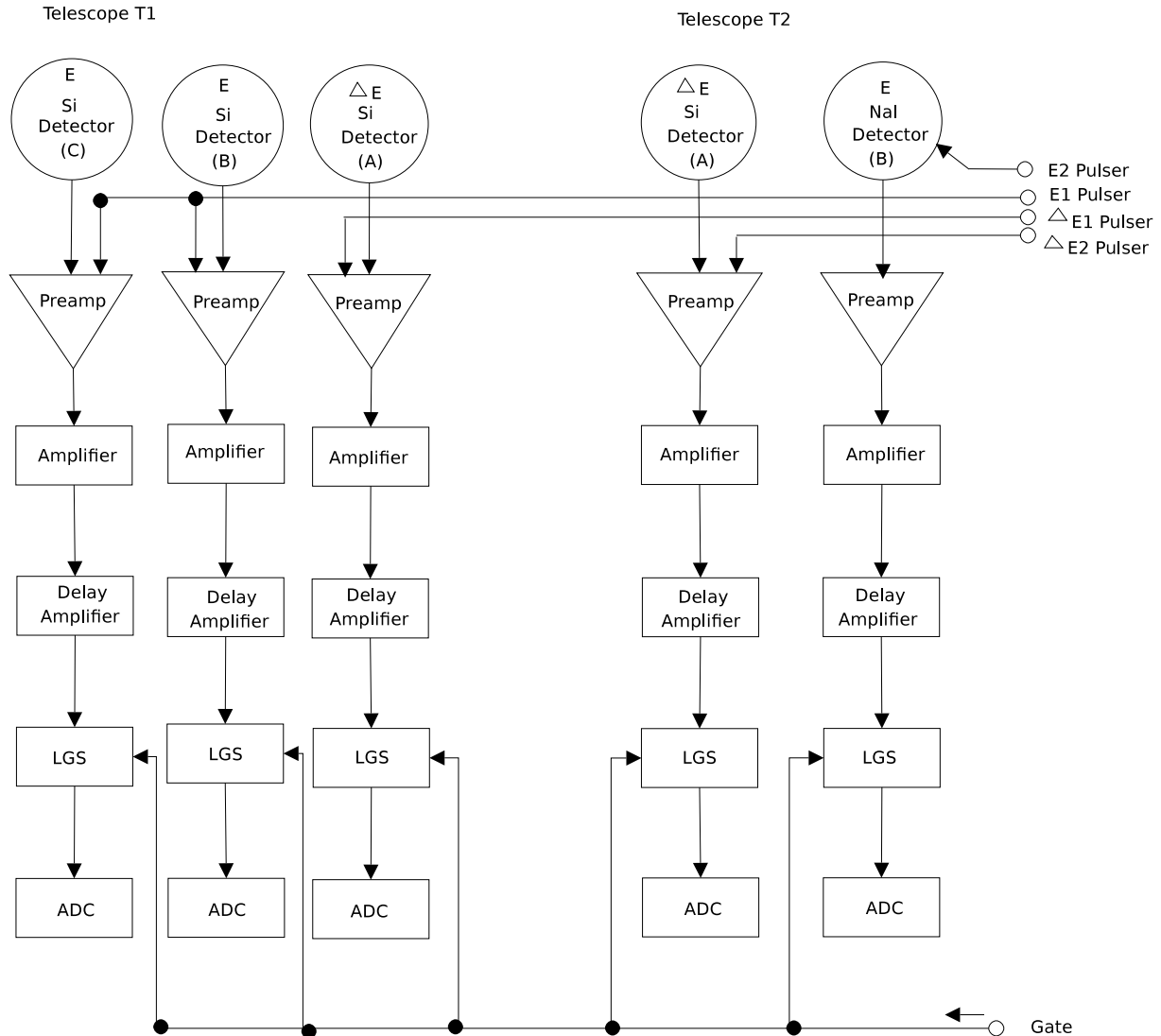


Figure 3.7. Linear electronics for telescopes T1 and T2.

The linear signals from the preamplifiers contain information on the amount of energy deposited in the respective detectors in form of the amplitude of the linear signal. The signal then passed through an amplifier, a delay amplifier and a linear gate and stretcher (LGS) to the analog-to-digital converter (ADC). The signal was fed into a LGS where a logic timing signal was required to open the gate for an event of interest. Such an event was a coincidence event between telescopes T1 and T2. The linear signals for such an event were then digitized by means of an ADC. The gate signals were inhibited by the

Module	Model
Preamplifier	ORTEC 113
Amplifier	ORTEC 575
Delay Amplifier	ORTEC 427A
Linear Gate and Stretcher (LGS)	ORTEC 542
Analog-to-digital converter (ADC)	CANBERRA 8077

Table 3.5. *NIM modules used to process the linear signals.*

computer busy signal (see Subsection 3.8.8) to ensure that only events that were able of being processed by the data acquisition system were passed to the ADC's for digitization. A block diagram of the linear circuit of the Si and NaI(Tl) detectors is shown in Fig. 3.7. The NIM modules used to process the linear signals are listed in Table 3.5.

3.8.4 Current Integrator

The current from the beam stop was fed into the current integrator situated in the data room in order to determine the accumulated charge. The current integrator linearly associates a number of pulses per second to the current, with a full-scale value of 1000 pulses per second for a given range.

3.8.5 Pulsers

Each detector element was provided with a pulser signal which is essentially triggered at a rate proportional to the beam current. The purpose of the pulser system was to perform offline corrections for gain drifts in the photomultiplier tubes of the NaI(Tl) detectors and electronic dead time. The ratio of pulser events accumulated in the ADC spectrum to the equivalent inhibited pulser scaler reading determines the electronic dead time.

To generate the pulser signals for each detector element, the following procedure was used. The digital output of the current integrator was fed into a timing single channel analyzer (TSCA) from which the positive output was fed into the external input of a constantly running timer of which the start-input was connected to the stop-output (see Fig. 3.8).

3.8.6 Clock

A continuously running timer, was linked to the timing single channel analyzer (TSCA) and served as an electronic clock. The clock was fed to both an uninhibited and inhibited scaler. The difference between the two scaler readings gives an indication of the computer dead time. A simplified block diagram which illustrates the electronic setup of the pulsers and the clock circuitry for a double telescope setup is shown in Fig 3.8.

3.8.7 Event trigger

Any event which passed the logic requirements as an event of interest ($T1 \cap T2$) was accepted in the event trigger module. This trigger signal enters the computer via a CAMAC module.

3.8.8 Computer busy

The computer busy signal was generated for every event accepted by the CAMAC event trigger module. This signal was fanned out in order to veto the $T1 \cap T2$ coincidences and also inhibit the scalers (see Fig. 3.6).

3.8.9 Pattern registers

The pattern register module was used to register the type of event. A certain event such as a coincidence event, contains data from the different T1 detector elements, data from a pulser and is associated with the beam polarization of up or down orientation. Such information was registered by this unit. The strobe signal which is a delayed event trigger initiated the readout of the pattern register latching all the bit pattern inputs as defined in Table 3.6.

3.8.10 Scalers

The function of a scaler is simply to count the number of certain event types. Every event of interest for which a logic signal was generated (see Fig. 3.6) was counted by two CAMAC

Bit	Pattern Register	Scalers	
		Uninhibited	Inhibited
1	–	Current Integrator	Current Integrator
2	–	Clock	Clock
3	$T1 \cap T2$	Pulser trigger	Pulser trigger
4	T1A event	$T1 \cap T2$	Current Integrator (spin-up)
5	T1B event	–	Current Integrator (spin-down)
6	T1C event	–	T2 (all events)
7	Pulser event	–	–
8	Spin-up	–	$T1 \cap T2$
9	Spin-down	–	T1 (all events)

Table 3.6. *Bit pattern register and scaler input definitions.*

multi-scaler modules. As described in Subsection 3.8.8, one of these modules was inhibited by the computer busy signal. Different scaler input definitions are also listed in Table 3.6.

Inhibited and uninhibited scalars read into inputs 1 to 3 kept count of the current integrator, clock and pulser trigger, respectively. Inputs 4 and 8 counted events which resulted from the coincidence condition ($T1 \cap T2$). However, the inhibited scalars read into inputs 4 and 5 kept track of the current integrator with spin-up and spin-down respectively while inputs 6 and 9 provided scaler readings for all events in telescope T2 and telescope T1 respectively.

3.8.11 Computer interface

CAMAC is a modular system which is the interface between the outputs of the nuclear instrument module (NIM) and the computer which activates and controls the data acquisition program. The processed electronic signals arrive at the computer interface via CAMAC crates which provide slots for the necessary interface modules. In the current coincidence experiment, the analog signals of every accepted event were digitized by the ADC's. The digital data output of each of these ADC's was connected to a CAMAC interface module which controlled (enabled, disabled and cleared) the ADC and read the digitized data as a 16-bit word.

Moreover, the CAMAC crate also accommodated the modules for the event trigger, pattern registers and scalars.

3.9 Data Handling

Linear and timing signals of accepted events were processed using NIM and CAMAC electronic hardware. The VME was used as an interface between the VAX data acquisition computer and the CAMAC system made up of ADC's, scalers, bit pattern registers, event trigger modules and current integrator readout module.

The data readout code is executed on the VME processor which reads out the event data from the CAMAC system, stores the event into multi-event buffers, and when full, these buffers are transferred over the ethernet network to the back-end sorting workstation. The readout code is configured for a particular experiment by means of C code header files (VME files) which are then compiled into the readout image which is loaded into the VME processor.

The software XSYS which operates on a VAX computer was used for data acquisition and for event-by-event data replay [41]. The subprocess XSORT which makes use of the event analysis language program (EVAL) initiated the data sorting process. A command procedure (COM) file defines data areas for various histograms to be stored and data areas for gates. The EVAL program sorts data either from the online ADC's or from event-by-event files which are written on tapes.

3.10 Experimental Procedure

After mounting and aligning the collimators and detectors in the scattering chamber, the cables were patched between the detectors and the ports of the scattering chamber in such a way that the arms would have maximum freedom to move over the angular range covered (see Section 3.7). After completing the setup inside the scattering chamber and the electronics, the scattering chamber was pumped down to the required vacuum ($\sim 10^{-5}$ mbar).

In the data room the necessary NIM modules were set up according to the linear and logic timing circuits (see Figs. 3.4 and 3.7), which were linked to the corresponding CAMAC interfaces. Prior to the experiment the required ADC's were zeroed, that is, the zero

intercept of the ADC conversion function was adjusted so that a dc level of 0 volt at the analog input of the ADC would result in a digitized binary output value of 0. This procedure was performed by using a precision pulser. Pulses with different amplitudes were converted by the ADC's to calibrate these linearly.

On the target ladder in the scattering chamber five targets were mounted. Two ^{12}C targets were used for quasifree data acquisition and calibration purposes, while a $(\text{CH}_2)_n$ target was used for the setup procedure of the electronics. An empty target frame was used for beam halo tuning and a ruby crystal scintillation target was used for beam positioning. The $(\text{CH}_2)_n$ target was chosen for the timing of the coincidence setup. This was done by setting the two detector telescopes at symmetric angles such as scattered protons could be in coincidence with recoil protons in the $\text{H}(p,p)\text{H}$ reaction. The thresholds of the corresponding CFD's of the different detectors were set above the noise making sure that no events were lost in the different particle identification spectra.

The Si detectors were calibrated after the experiment by using alpha emitting ^{228}Th radioactive sources which were placed a few centimeters from the gold surface of each Si detector. The energy calibration of the NaI detectors were based on elastic and inelastic proton scattering off the ^{12}C target at proton angles of 40° and 60° , and at the angles of the coincidence runs. These particular runs were performed at the beginning of each of the four weekends.

The beam halo was checked with the empty target frame on the target ladder. The count rate due to halo interactions was obtained and could consequently be compared to the true count rate, i.e, with the target, to estimate the effect of the background. Therefore, in the cases where the effect of the halo was unacceptable, the halo was reduced by the operators with the use of various slits. Beam positioning was considered successful when the beam passed cleanly through the 3 mm diameter hole of the ruby target.

At the beginning of each weekend the beam offset was regularly determined. This was performed by scattering elastically unpolarized protons off the $(\text{CH}_2)_n$ target. Count rates in the $^{12}\text{C}(p,p)$ elastic scattering peak in the spectrum were taken with the same detector arm at equal angle to the left and to the right of the beam direction, usually at an angle of 20° . By comparing the count rates to the left and to the right of the beam, the beam offset could then be determined. A minimum beam offset of $\sim 0.2^\circ$ was tolerated. The

beam intensities varied between 60 nA and 100 nA depending on the detector count rate which was mainly determined by the target thickness and the scattering angle, and also according to random coincidence event (see Section 4.4).

Typical experimental runs lasted two hours and were only interrupted by the P-line polarization measurement runs. The polarization measurements in the P-line polarimeter were very sensitive to excessive background events caused by the collision of the beam and beam-line components upstream from the polarimeter scattering chamber. Since such events could completely obscure the elastic $^{12}\text{C}(p,p)$ events, a lower beam current (~ 6 nA) was used. The asymmetry of the polarimeter setup due mainly to an off-centre beam-spot was checked by means of an unpolarized beam and this was corrected for in the polarization measurement (see Section 4.8).

The data from all experimental runs were collected with XSYS, as the VME, COM and EVAL files were executed in real time on a VMS computer while the experiment was in progress. While acquiring data, the computer and electronic dead time were also monitored regularly. By keeping then track of all the scalers and the various contents of the analyzers while the experiment was running, we were able to ensure that the measurements were progressing well. The data was acquired over a period of four weekends. The online event-by-event data were written to hard disks. The data analysis was performed offline on a VMS computer to which a magnetic tape drive was linked. The offline analysis of the data is discussed in the next chapter.

Chapter 4

Replay of Data

4.1 Overview

This chapter describes the data analysis procedure which transformed the raw coincidence data into triple differential cross sections and analyzing power spectra. The data analysis procedure discusses the energy calibration of the detectors, the particle identification, the energy spectra used to extract different experimental events, the beam polarization measurements and certain corrections made to the data. Statistical errors propagated throughout the calculations and systematic errors introduced in the experiment are also discussed. The results of the analyzed experimental data are shown and further discussed in Chapter 5.

4.2 Energy Calibrations

4.2.1 Si detectors

Energy calibrations of the four Si detectors were carried out with alphas emitted from ^{228}Th sources. ^{228}Th and its decay products emit α -particles of energies of 5.34054 MeV, 5.42333 MeV, 5.658856 MeV, 6.05098 MeV, 6.22829 MeV, 6.7785 MeV and 8.78437 MeV, respectively. All Si detectors were thick enough to stop these α -particles. Figure 4.1 illustrates the typical energy spectrum of alphas from a ^{228}Th source for one of the silicon detectors.

Linear calibration (MeV): $y=m \times \text{bin} + c$			
Telescope	Element	m (MeV/bin)	c (MeV)
1	A	1.41485×10^{-2}	3.06311×10^{-2}
	B	7.62675×10^{-2}	0.12878
	C	4.95592×10^{-2}	7.22642×10^{-2}
2	A	1.38467×10^{-2}	-8.6015×10^{-2}

Table 4.1. Set of calibration parameters for the different Si detectors.

The calibration was done by identifying the channel numbers of the different peaks in the spectra and their corresponding energies. Calibration parameters were extracted by means of the least square fit method for a straight line. An example of a linear calibration curve is shown in Fig. 4.2 and a set of calibration parameters of the different Si detectors is listed in Table 4.1. Only four peaks were used for the calibration, other peaks could not clearly be identified from the known α -energy spectrum.

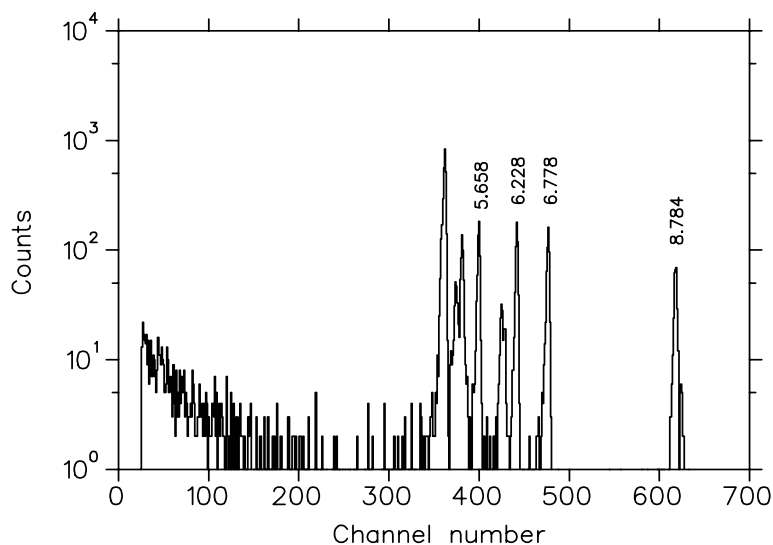


Figure 4.1. A characteristic energy spectrum of alphas from a ^{228}Th source generated for the $100 \mu\text{m}$ Si detector. The α energies are in MeV.

4.2.2 NaI detector

Protons scattered from ^{12}C provided the means for the energy calibration of the NaI(Tl) detector of the proton telescope (T2). Peaks from elastic scattering off carbon, and inelastic scattering to the first excited state of carbon were used. Similar spectrum gated on p - α

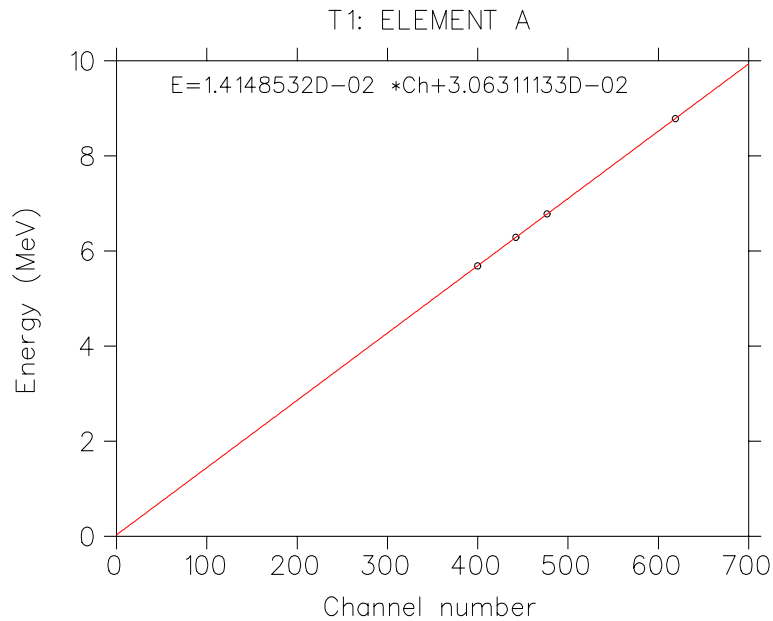


Figure 4.2. *Linear calibration curve for the 100 μm Si detector.*

coincidences (first coincidence run of each weekend) was also used for such purposes in order to extract good calibration parameters. The calibrations were done at proton angles of 40° and 60° for the raw spectrum and 30° , 60° and 70° proton angles for the spectrum gated on $p\text{-}\alpha$ coincidences depending on the weekend.

The corresponding energies of the ground state and the first excited state for the reaction were calculated using the computer code *KINMAT*. This was done by taking into account the respective amount of energies lost by the particle in the respective dead layers ($8\ \mu\text{m}$ kapton foil and $7\ \mu\text{m}$ Havar window) and the Si detector before reaching the stopping detector.

Figure 4.3 shows an example of the peak positions of the ground state, the 1^{st} and 3^{rd} excited states. The calibration was based on the ground and first excited states of ^{12}C measured at two scattering angles. For this work at an incident energy of 100 MeV, the energy calibration for protons performed by means of the least square fit method for a straight line (Fig. 4.4), was assumed to be sufficient. It was assumed that in all calibration lines, channel zero corresponds to zero energy.

The gain of the photomultiplier (PM) tube of the NaI(Tl) detector not only drifts as a result of a change in count rate but also tends to drift in time [42]. Therefore the energy

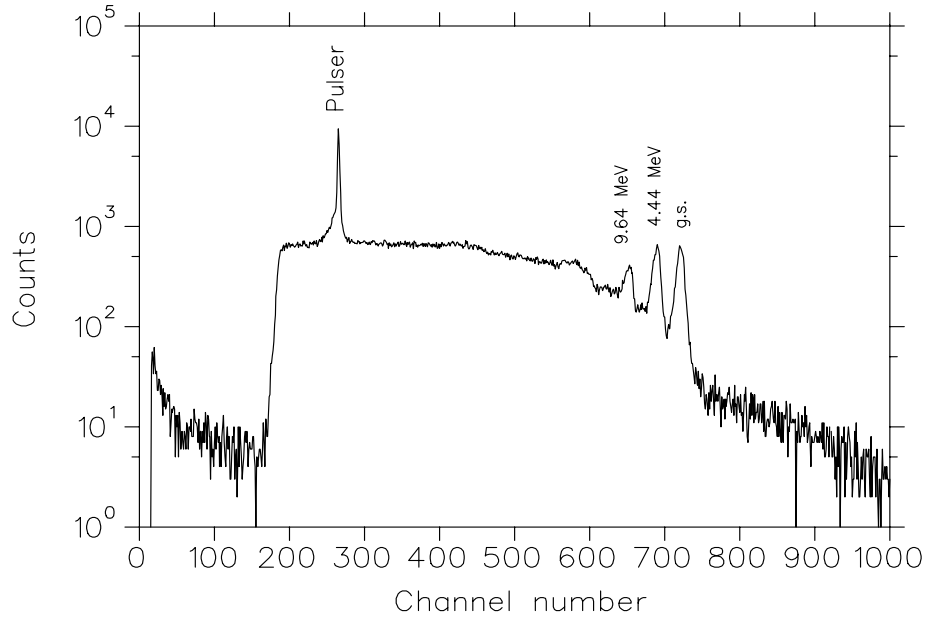


Figure 4.3. An example of a raw NaI detector spectrum, used for the energy calibration, illustrating the separated peaks of the ground, the 1st and 3rd excited states in ^{12}C together with the pulser peak.

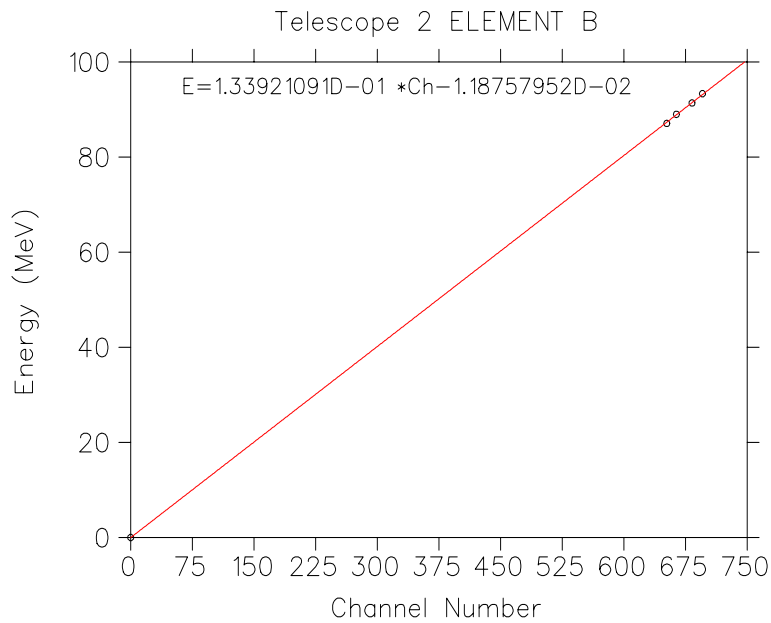


Figure 4.4. A linear calibration curve for the NaI detector.

calibration was performed for each weekend. The set of detector calibration parameters for each weekend with the corresponding beam energy is tabulated in Table 4.2.

Linear calibration (MeV): $y=m \times \text{bin} + c$			
Weekend	Beam energy (MeV)	m (MeV/bin)	c (MeV)
1	101.51	0.13392	-1.18758×10^{-2}
2	101.56	0.13315	-2.97969×10^{-3}
3	101.45	0.13526	-8.75339×10^{-2}
4	101.97	0.13714	-5.44586×10^{-2}

Table 4.2. Set of NaI(Tl) detector calibration parameters for each weekend.

4.3 Particle Identification

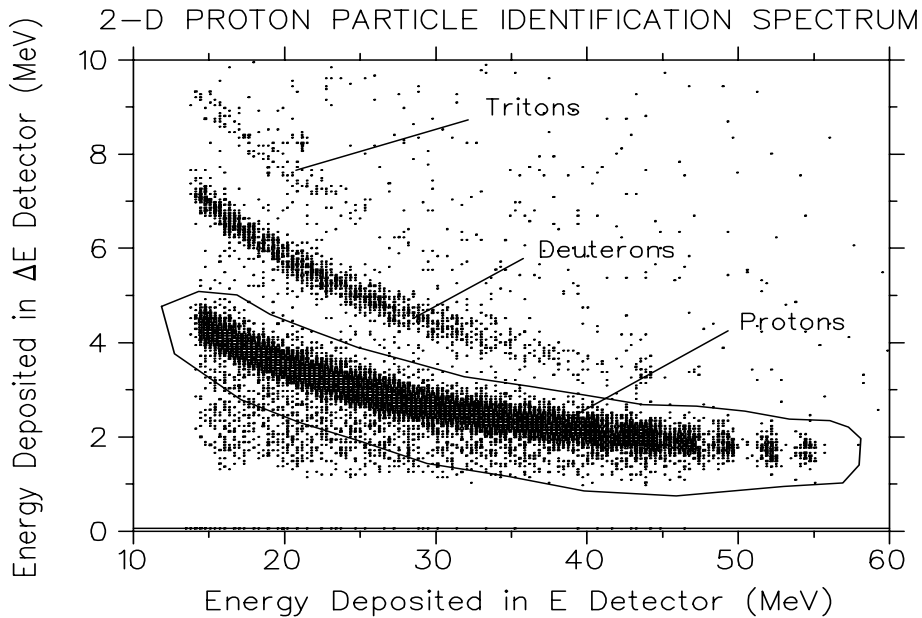


Figure 4.5. Typical two-dimensional PID spectrum with a gate set around the proton locus.

Particle identification (PID) was achieved with the standard ΔE - E technique in which combinations of the detectors in the telescopes were used to measure energy loss and total energy of ejectiles. The energy loss of charged particles is determined by making use of the Bethe-Bloch approximation [43]

$$\Delta E \propto \frac{Z^2}{v^2}, \quad (4.1)$$

where ΔE denotes the energy loss, Z and v are the atomic number and the velocity of the

particle, respectively. Equation (4.1) becomes

$$\Delta E \propto \frac{mZ^2}{E}, \quad (4.2)$$

at non-relativistic velocity, where E is the kinetic energy and m is the mass of a charged particle.

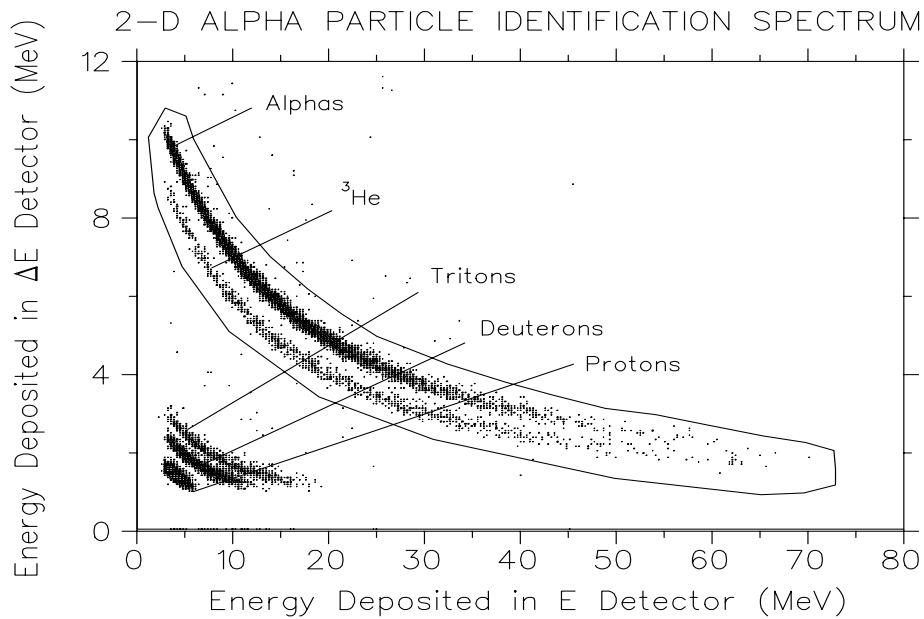


Figure 4.6. Typical two-dimensional alpha PID spectrum with a gate set around the alpha-³He locus.

Figures 4.5 and 4.6 show examples of PID spectra used to select particles of interest.

In order to allow for a reliable separation of alphas from adjacent ³He a mass function was generated. The mass function was generated using the following equation

$$MF = [(E_{\Delta E} + E_E)^p - E_E^p] \times MS + MO, \quad (4.3)$$

where $E_{\Delta E}$, E_E denote the energies of the ΔE and E detectors, respectively, and p , MS and MO are constants. The separation was optimised by changing MS and MO . This was obtained with the values of 1.75, 2.0 and 0.0 for p , MS and MO , respectively. In Fig.

4.7 the mass function spectrum is displayed with the gate set around the alpha particle locus.

Protons and alpha particles were selected by setting a gate around their corresponding loci in the PID (Fig. 4.5) and mass function (Fig. 4.7) spectra, respectively.

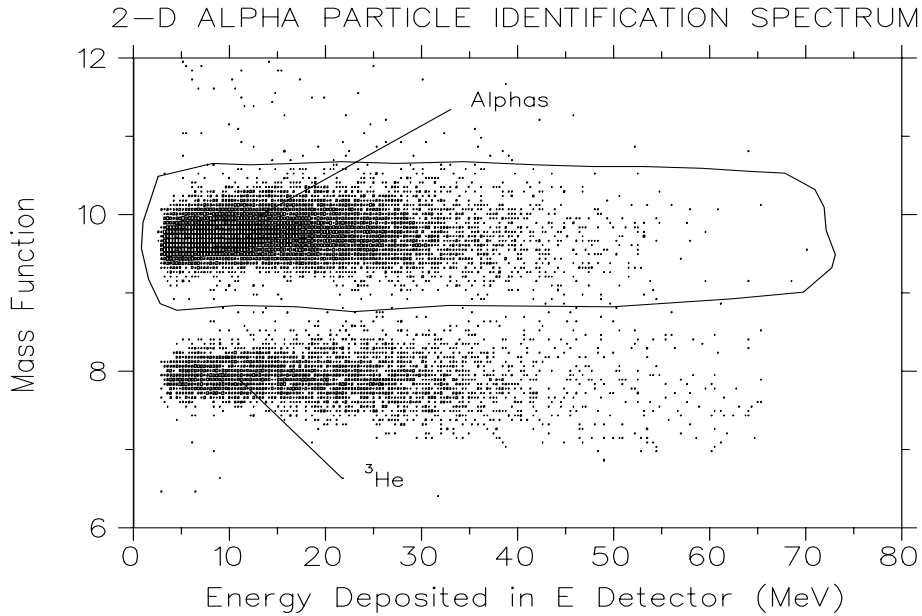


Figure 4.7. Typical two-dimensional mass function spectrum with a gate set around the α -particle locus. The y -axis is in arbitrary units.

In addition it should be pointed out that, at the three smallest proton angles, the coincident alpha particles that satisfy the quasifree condition were stopped in the first detector of T1. Thus a particular PID spectrum which combines protons and alphas, detected in the corresponding T1B and T1A detectors, was used for selecting the coincident quasifree alpha-events. Figure 4.8 shows a typical example where x - and y -axes represent the deposited energy of protons in detector T2B and alphas in detector T1A, respectively. The locus in the spectrum indicates the p - α quasifree locus from which alphas were selected by setting a gate around it. The gate was set according to the energy deposited by alphas which stopped in the detector T1A. Of course, this gate did not include the high-energy alphas which punch through to the second detector (T1B). However, those alpha events were nevertheless selected using the standard method.

Apart from the α -locus of interest in Fig. 4.8, random coincidences between protons scat-

tered from ^{12}C and other particles are observed (line parallel to the y-axis approximately at channels 177, 170 and 162). The locus of events between the threshold and channel ~ 50 on T1A is mainly due to evaporation α -particles in coincidence with all protons in T2.

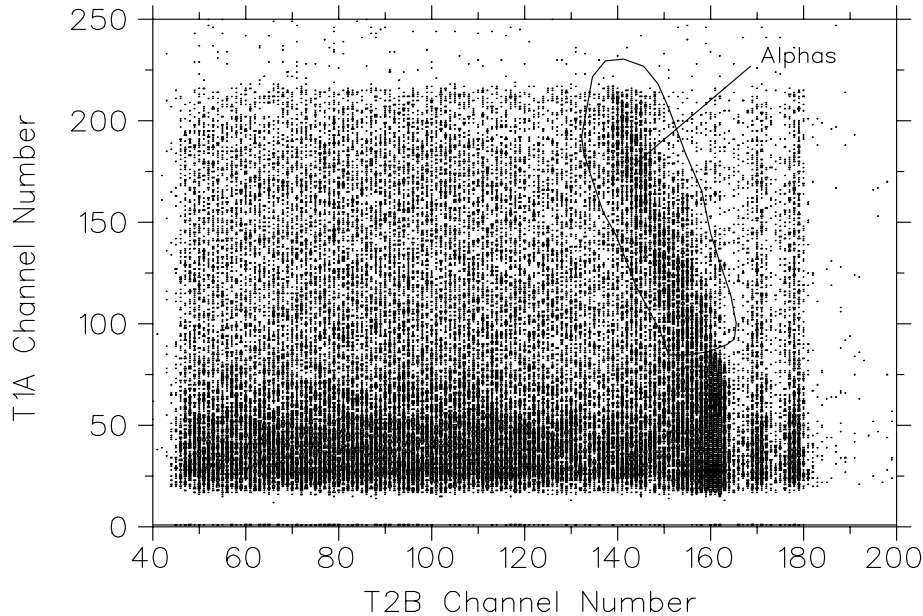


Figure 4.8. Typical spectrum used to select alpha events at the three smallest proton angles with a gate set around the alpha locus. The gate was set according to the energy deposited by alphas which stopped in the detector T1A.

4.4 Timing Spectra

In coincidence measurements, the $T1 \cap T2$ and T2 events generate the start and stop signals for the TAC, respectively. The TAC stop signal was delayed with respect to the TAC start signal (~ 50 ns) to permit acquisition of data on background random coincidences over a span of several beam bursts. The TAC time range was about 500 ns.

Random coincidences consider particles that are generated through interactions of incident protons coming from different beam packets or from two different incident protons in the single beam packet. However, coincidences which refer to signals from the same beam packet are defined to be true. In order to extract data for true coincidences only, the random coincidence events, i.e. different events in the same beam packet which are buried underneath the true peak, are normally subtracted from coincidence events. This could

be done by setting two gates which represent random and true coincidences in the TAC spectrum as displayed in Fig. 4.9 (see Subsection 4.5.4).

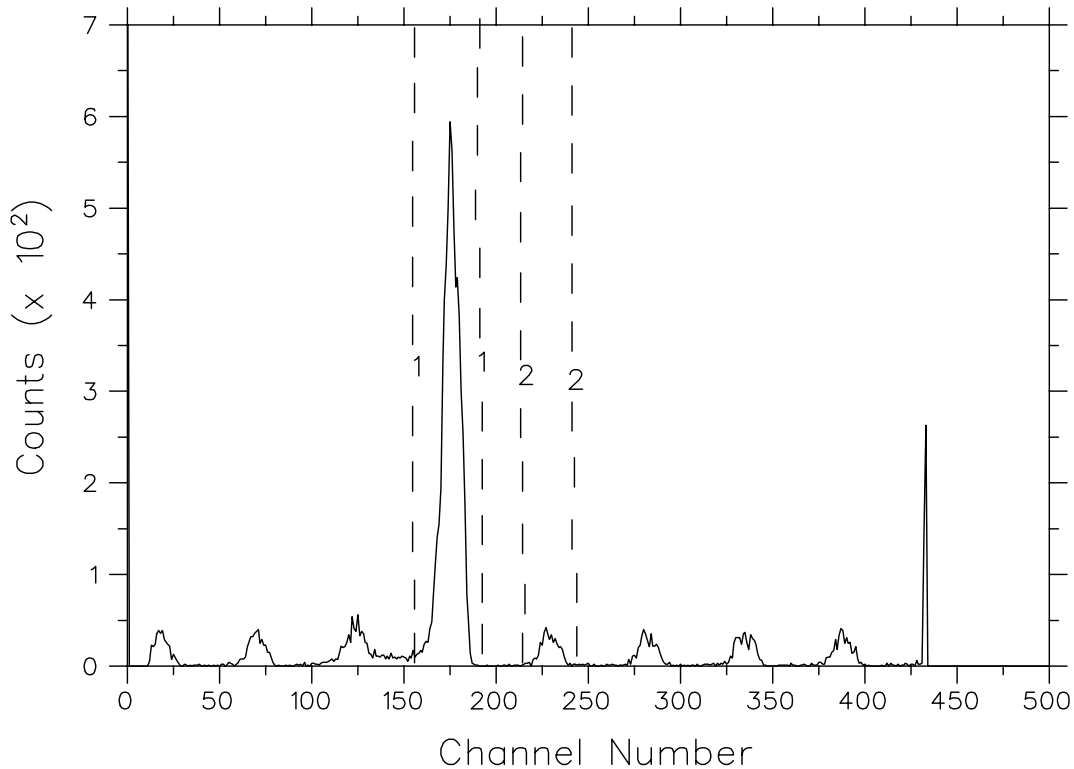


Figure 4.9. Typical representation of a TAC spectrum displaying the time structure over a time range of beam bursts obtained from coincidence events. True coincidence events are selected by the one-dimensional time gate 1 and random coincidence events by gate 2. The coincident pulser signals are well separated from any of the time peaks.

4.5 Experimental Data Corrections

4.5.1 Gain drifts

Since the gain of the photomultiplier tube of the NaI(Tl) detector changes with count rate and time, it was of great importance to maintain the initial gain on the detector for all measurements over one weekend. This was done by monitoring changes in the pulser spectrum generated by a fixed, calibrated light source such as a light-emitting diode (LED) embedded in the crystal of the detector. The position of the pulser peak in the energy spectrum at the beginning of the weekend was used as a reference point for calibration.

A separate gate was set around this initial pulser position. At any drifting of the pulser position, a drift-correction factor was automatically calculated and applied to the centroids of peaks recorded in the NaI detector by the routine *EV AL* code. This correction was also applied to the calibration parameters used by *EV AL*.

4.5.2 Dead layer energy corrections

Particles detected lost a certain amount of energy in energy absorbing material (dead layers) and ΔE detectors before stopping in the E detectors. The true energy of the particle was calculated by adding the total energy loss in the dead layers and ΔE detectors to the E measured energy. This was done using the computer program *KINMAT* which calculates the total energy loss of particles in the respective dead layers (kapton foil and Havar window) and ΔE detector. These corrections were taken into account when calibrating the NaI E detector of T2.

4.5.3 Electronic and computer dead time

The electronic dead time was determined according to Subsection 3.8.5 and was typically 1% to 2% during the experimental measurements. Therefore, a dead time correction was included in the experimental cross section determination.

Computer dead time was automatically corrected for by means of a busy output (see Subsection 3.8.8) which was used as a veto signal in the electronic signal processing.

4.5.4 Subtraction of random coincidences

It is very important to determine to what extent particles coming from random coincidences contribute to the spectra of interest when dealing with coincidence measurements. Usually the data for true coincidence events are extracted by subtracting events from random coincidences from the total amount of events. Therefore, an estimate of the random events falling within a true coincidence peak in the time distribution has to be made. This is done by considering events from gate 2 (see Fig. 4.9) on a random peak and estimate

the contributions of regions which can be populated only by random coincidences on the two-dimensional energy spectra. The contribution of the random coincidences to the true coincidences was found to be in the range of 2 – 3%. This is a very small percentage, and it suffers from a large statistical uncertainty. Therefore, due to the risk that subtraction of random coincidences could distort the spectra, albeit by an insignificant amount, we did not perform such a correction.

4.5.5 NaI reaction tail

The detection of charged particles in scintillator detectors relies on the following process. The detectors, when exposed to a certain form of radiation exhibit first of all their luminescence property, i.e. absorb and reemit the energy in the form of visible light. Usually the process, called fluorescence, takes place when the reemission occurs immediately after absorption. However, very often this is delayed because of the excitation of the crystal material via Coulomb interaction between the charged particles and the electrons of the atoms in the crystal of the detector. The photomultiplier tube then converts the weak light output of the scintillation pulse into an electrical signal.

However, it is possible that these Coulomb interactions can be preceded or followed by inelastic interactions between the charged particles and the nuclei of the detector material. In this case, a particle may lose energy through these interactions and then deposit a smaller amount of energy in the detector than a particle of the same energy that had only undergone multiple electronic scattering. As a consequence, these events will fall out of the full-energy peak, and appear as so-called reaction tail events at lower energies [44].

During data analysis, reaction tail corrections were performed. Such corrections are made according to the efficiency of the NaI(Tl) detector for detecting protons. The efficiency of the NaI(Tl) detector is determined by the ratio of the amount of events in the tail region to the number of events in the full-energy peak.

Green *et al.* [45] performed a functional fit to the data, and obtained the following tail-to-peak ratio :

$$f(E_p) = \left(\frac{E_p}{354} \right)^{1.8}, \quad (4.4)$$

where E_p is the full energy of a proton in MeV.

For the coincidence experiment, the corrected number of counts N_c is given by

$$N_c = (1 + f(E_p)) N , \quad (4.5)$$

where N is the number of counts before the tail correction.

Although this method estimated the ratio to be about 5.4% for 70 MeV protons, an improved accuracy can be obtained by using a model developed at iThemba LABS [3]. The number of counts in the reaction tail T can be expressed as a function of the observed energy E and the peak energy E_p , parametrized in terms of Legendre polynomials P_i of odd order. It can then be written in the form

$$T(E, E_p) = E_p a_1 P_1(E/E_p) + \sum_{i=3}^7 a_i P_i(E/E_p) . \quad (4.6)$$

The factor E_p in the first term was included to reproduce a slope that is independent of the peak energy, as suggested by the experimental data [3]. The constants a_i obtained in a simultaneous least-squares fit to all the data are listed in Table 4.3.

From Eq. (4.6), by integrating over the full energy range, the tail-to-peak ratio was found to be

$$f(E_p) = (8.55E_p^2 + 157E_p) \times 10^{-6} . \quad (4.7)$$

This expression was therefore applied to the number of counts in a bin (see Section 4.9) in order to correct for the reaction tail as described above.

4.6 Data Sorting

A signal from the ion source alternating between spin-up and spin-down was fed among others into a bit pattern register module (see Subsection 3.8.9). Based on the value in the pattern register, the data acquisition system was able to sort the data either as a spin-up or spin-down event.

Parameter	Value
a_1	1.1×10^{-5}
a_3	-1.39×10^{-3}
a_5	-7.51×10^{-4}
a_7	-7.47×10^{-4}

Table 4.3. Legendre polynomial coefficients fitted to the experimental data to generate the NaI detector response, taken from [3].

4.7 Energy Spectra

4.7.1 Two-dimensional energy spectra

For a particular angle pair of emitted particles, a two-dimensional coincidence spectrum of total energy (E_{Tot}) versus proton energy (E_p) was generated. E_{Tot} is defined as

$$E_{Tot} = E_p + E_\alpha + E_R - Q, \quad (4.8)$$

where the subscripts p , α and R refer to proton, alpha and recoil particles, respectively, and Q is the ground state Q -value of the reaction. For every p - α coincident event E_R was calculated from the measured energies of the proton and alpha particle and from the given reaction parameters such as particle mass, incident proton energy and angles of detection. This was performed using a routine linked to the *EVAl* code. Since E_{Tot} is constant for any particular state of the residual nucleus, the corresponding events should appear as a straight locus in the two-dimensional energy spectrum. An example of such a spectrum is displayed in Fig. 4.10.

Below the locus corresponding to knockout to the ground state in Fig. 4.10 we see events associated with the first excited state of the residual nucleus (see next Subsection). Events which are probably due to sequential decay are also observed at lower total energy close to the maximum proton energy.

The subpanel in Fig. 4.10 shows a part of the two-dimensional spectrum with lower resolution which actually displays the main features slightly better.

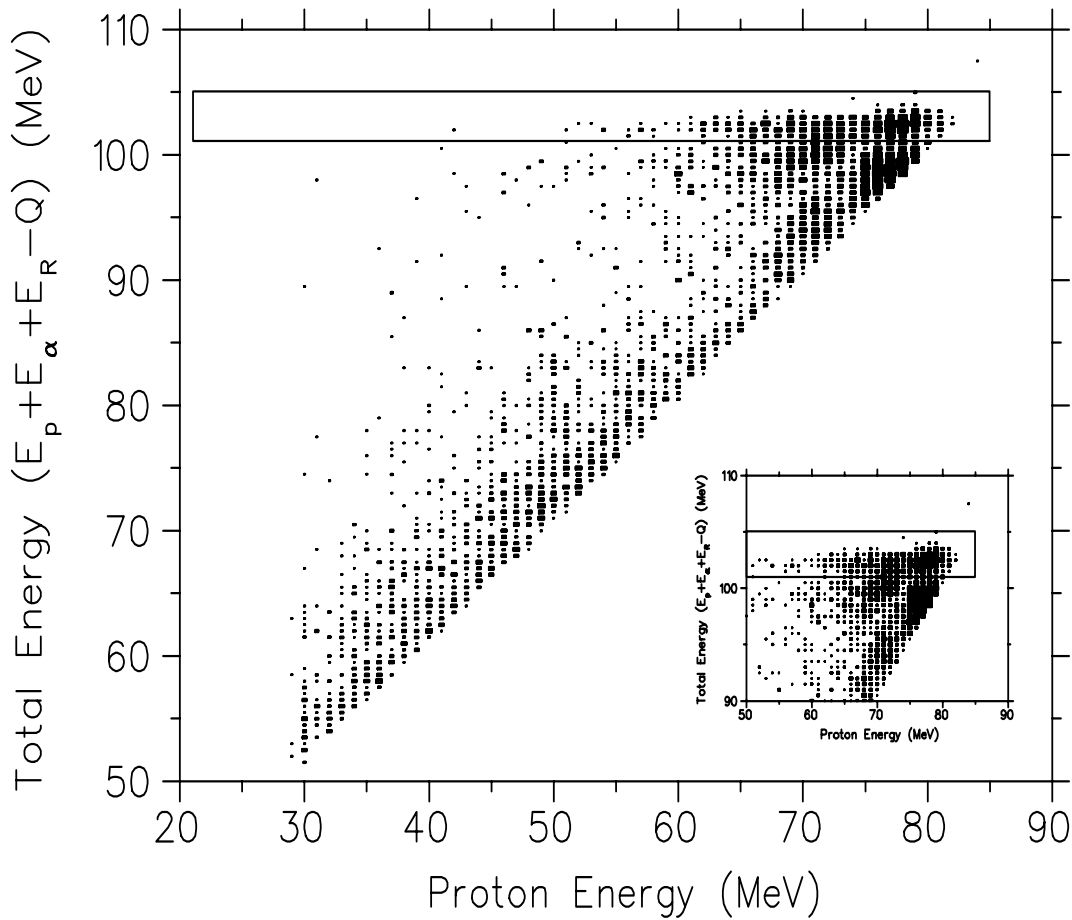


Figure 4.10. A typical two-dimensional energy spectrum. The gate is set around the quasifree ground-state knockout locus.

4.7.2 Binding energy spectra

The binding energy spectrum for the reaction is obtained by projecting the data of two-dimensional energy spectrum onto the E_{Tot} axis. In such a spectrum, the extent of the quasifree knockout locus could be clearly identified. This was then used to select the coincidence events of interest by accurately setting the gate on the two-dimensional total energy spectrum. A typical binding energy spectrum, with a missing-mass resolution of approximately 1.5 MeV is presented in Fig. 4.11.

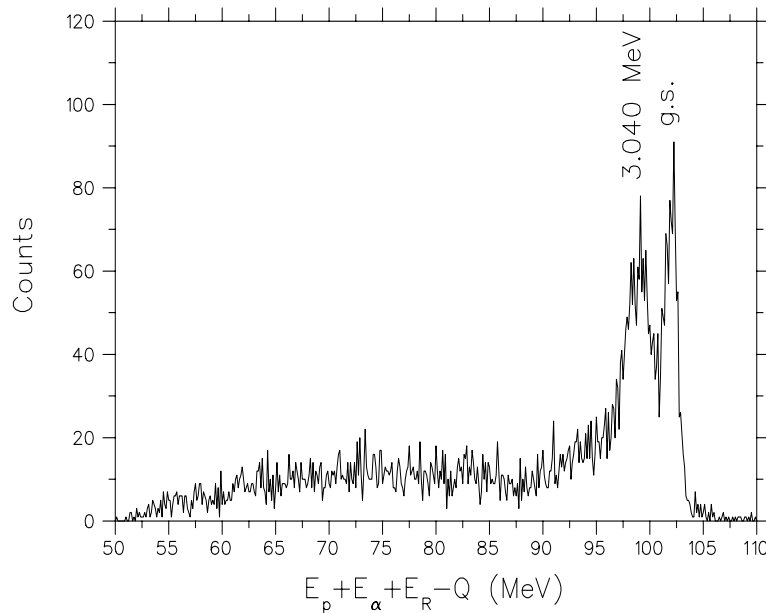


Figure 4.11. A typical binding energy spectrum for the reaction $^{12}\text{C}(p, p\alpha)^8\text{Be}$. The ground state (g.s.) and first excited state of the residual nucleus ^8Be are clearly resolved.

4.7.3 Energy-sharing Spectra

Energy-sharing spectra were extracted by projecting the data inside the two-dimensional gate of the quasifree knockout locus onto the proton energy axis. The histogram in Fig. 4.12 represents a typical extracted energy-sharing spectrum. These energy-sharing spectra were therefore used to extract energy-sharing cross section and analyzing power distributions (see Sections 4.9 and 4.10). The energy-sharing spectra for proton angles from 52° to 110° were binned in 4 MeV size to increase the statistics. However, because of sufficient statistics, the energy-sharing spectra for the three smallest proton angles could be binned in 1 MeV size.

4.8 Polarization Measurements

The beam polarization up (p^\downarrow) and the polarization down (p^\uparrow) are determined independently with the P-line polarimeter, based on the known analyzing power value at the set detector angle taking into account the left/right asymmetry contributions of the detector

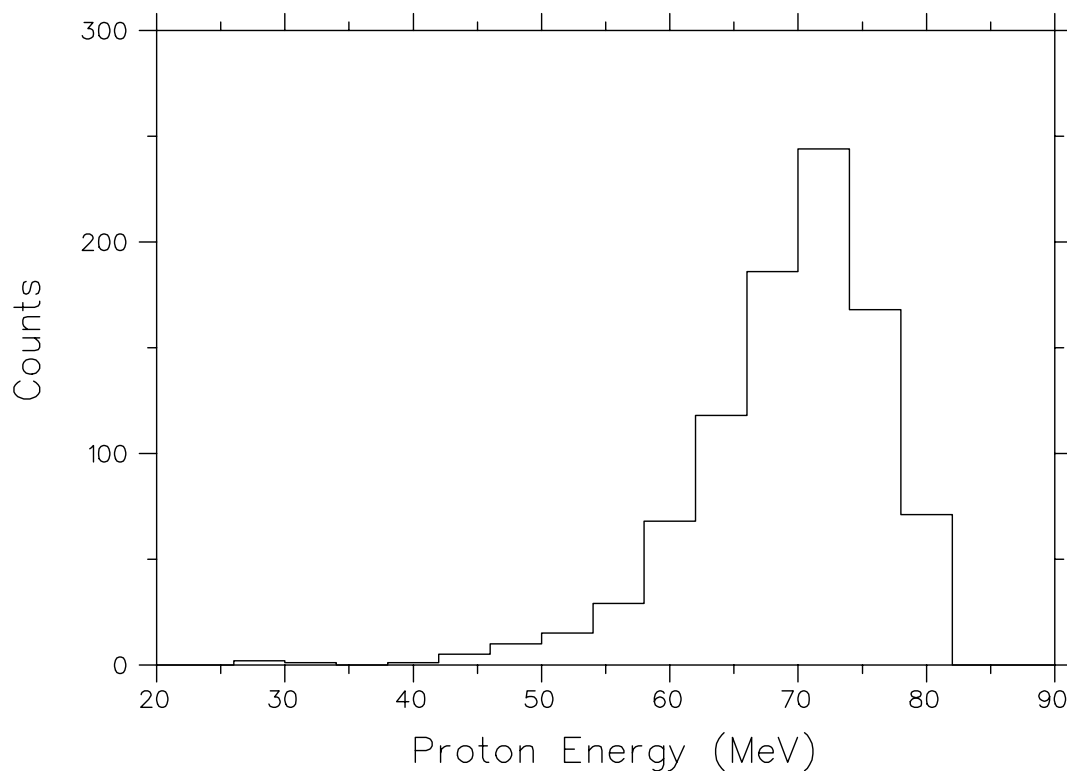


Figure 4.12. *Typical energy-sharing spectrum. Counts as a function of proton energy obtained for p-α coincidence events.*

efficiency, from [46]

$$p^{\uparrow(\downarrow)} = \frac{1}{A_y} \left(\frac{L^{\uparrow(\downarrow),unpol} - R^{\uparrow(\downarrow)}}{L^{\uparrow(\downarrow),unpol} + R^{\uparrow(\downarrow)}} \right), \quad (4.9)$$

where $L^{\uparrow(\downarrow)}$ and $R^{\uparrow(\downarrow)}$ refer respectively to the number of elastic scattered events recorded in the two detectors (set in the polarimeter P-line) positioned at symmetric angles to the left and right of the incident beam direction when the beam is in the spin-up/spin-down orientation. The parameter $unpol = R_{unpol}/L_{unpol}$, where $R(L)_{unpol}$ is the number of events in the right/left detector for an unpolarized beam. This is a measure of the asymmetry of the polarimeter setup due to a possible off-centre beam-spot.

In the special case where $p^{\uparrow} = p^{\downarrow} = p$, the beam polarization is extracted from the known analyzing power using the symmetric setup of the two detectors by means of the super-ratio technique [46]

	<i>unpol</i>	p^\uparrow (%)	p^\downarrow (%)
Weekend 1	0.93	64±2	84±2
Weekend 2	0.94	66±2	75±2
Weekend 3	0.88	67±2	80±2
Weekend 4	0.91	69±2	77±2

Table 4.4. Summary of average values of the beam polarization and *unpol* for different weekends.

$$p = \frac{1}{A_y} \left(\frac{r-1}{r+1} \right), \quad (4.10)$$

where

$$r = \left(\frac{L^\uparrow R^\downarrow}{L^\downarrow R^\uparrow} \right)^{1/2}. \quad (4.11)$$

However, during this experiment this kind of situation was not experienced. The polarization of spin-up and spin-down beams were then determined independently from each other. The average values of beam polarization (p^\uparrow, p^\downarrow) and *unpol* determined from polarized and unpolarized beams, respectively, are listed in Table 4.4.

The error in the average beam polarization as defined in Eqs. (4.10) and (4.11), neglecting uncertainty of A_y , is given by [46]

$$\frac{\Delta P}{P} = \frac{1}{A_y} \cdot \frac{r}{r^2 + 1} \cdot \left[\frac{1}{L^\uparrow} + \frac{1}{R^\uparrow} + \frac{1}{L^\downarrow} + \frac{1}{R^\downarrow} \right]^{1/2}. \quad (4.12)$$

This value was taken to approximate the polarization error in p^\uparrow and p^\downarrow .

4.9 Absolute Cross Section

The number of p - α events in each energy bin which corresponds to spin-up and spin-down incident beam polarization (C^\uparrow and C^\downarrow), respectively, can be expressed as [46]

$$d^3\sigma \propto C^\uparrow = I_0(1 + p^\uparrow A_y), \quad (4.13)$$

$$d^3\sigma \propto C^\downarrow = I_0(1 - p^\downarrow A_y), \quad (4.14)$$

where I_0 represents the coincidence yield at the same kinematics but for an unpolarized incident beam. p^\uparrow and p^\downarrow are the spin-up and spin-down beam polarizations while A_y is the analyzing power for the reaction.

The triple differential cross sections (in $\text{mb sr}^{-2} \text{MeV}^{-1}$) are calculated using the conversion of the number of events in each energy bin of the energy-sharing distribution to an absolute value. This is done by multiplying the number of events with a conversion factor.

Using the two equations defined above, the coincidence yield I_0 for the unpolarized incident beam is given as [46]

$$I_0 = \frac{C^\uparrow + C^\downarrow}{2 + A_y(p^\uparrow - p^\downarrow)}. \quad (4.15)$$

The number of coincidence events recorded for the unpolarized incident beam can be converted as follows

$$d^3\sigma_0 = \frac{d^3\sigma^\uparrow + d^3\sigma^\downarrow}{2 + A_y(p^\uparrow - p^\downarrow)}, \quad (4.16)$$

where $d^3\sigma_0$, $d^3\sigma^\uparrow$ and $d^3\sigma^\downarrow$ represent the triple differential cross sections for unpolarized, polarized spin-up or polarized spin-down incident beam, respectively.

According to the energy-sharing distribution spectrum, the number of events for the unpolarized beam I_0 was found to be

$$I_0 = \frac{C^\uparrow + C^\downarrow}{2}, \quad (4.17)$$

which permits to express the unpolarized differential cross sections as

$$d^3\sigma_0 = \frac{d^3\sigma^\uparrow + d^3\sigma^\downarrow}{2}. \quad (4.18)$$

The absolute triple differential cross sections in the laboratory coordinate system are given by [42]:

$$\frac{d^3\sigma}{d\Omega_p d\Omega_\alpha dE_p} = \frac{N_c}{\Delta\Omega_p \Delta\Omega_\alpha \Delta E_p N_0 \rho D}, \quad (4.19)$$

where

- N_c is the number of counts in a bin,
- $\Delta\Omega_p, \Delta\Omega_\alpha$ are the solid angles (in sr) subtended by the telescopes T2 and T1, respectively,
- ΔE_p is the width of the energy bin (in MeV),
- N_0 is the total number of incident protons on the target,
- ρ is the density of target nuclei (in mb^{-1}) and
- D is the electronic dead time correction factor.

The number of incident protons on the target N_0 is given by :

$$N_0 = \frac{C}{e},$$

where

- e is the proton charge (in Coulomb)

- C is the total integrated charge as measured by the current integrator at the beam stop (in Coulomb) which was calculated from

$$C = CI.R.10^{-12} ,$$

where

- CI is the inhibited scaler reading of the current-integrator,
- R is the selected range (in nA) which represents 1000 counts per second for a full-scale current read-out.

The density of target nuclei is given by :

$$\rho = \frac{\lambda_T N_A}{\cos \theta_T A} \times 10^{-30} ,$$

where

- λ_T is the target thickness expressed in mass per unit area (mg/cm^2),
- N_A is Avogadro's number,
- θ_T is the angle between the direction normal to the target and the beam direction, and
- A is the atomic mass of the target (in g/mol).

4.10 Analyzing Power

The analyzing power of the reaction is extracted using the Eqs. (4.13) and (4.14) and is given by :

$$A_y = \frac{C^\uparrow - C^\downarrow}{p^\downarrow C^\uparrow + p^\uparrow C^\downarrow}, \quad (4.20)$$

where $C^{\uparrow(\downarrow)}$ represents the total number of events per energy bin for the proton beam polarized in the upwards (downwards) direction, and $p^{\uparrow(\downarrow)}$ represents the degree of polarization for the polarized beam.

4.11 Error Analysis

4.11.1 Statistical errors

The statistical error bars shown in the energy-sharing distributions were calculated from the real coincidence events assuming that the yield per unit time in each bin followed a Poisson distribution. These errors are given by

$$\sigma = \sqrt{N}, \quad (4.21)$$

where N denotes the number of counts in an energy bin.

Considering

$$A_y = \frac{C^\uparrow - C^\downarrow}{p^\downarrow C^\uparrow + p^\uparrow C^\downarrow}, \quad (4.22)$$

the statistical error of the analyzing power is calculated by applying the error propagation formula [43] which gives

$$\sigma_{A_y} = \left[\frac{C^\uparrow + C^\downarrow}{(p^\downarrow C^\uparrow + p^\uparrow C^\downarrow)^2} + (C^\uparrow - C^\downarrow)^2 \cdot \frac{(p^{\downarrow 2} C^\uparrow + p^{\uparrow 2} C^\downarrow)}{(p^\downarrow C^\uparrow + p^\uparrow C^\downarrow)^4} \right]^{1/2}. \quad (4.23)$$

Note that this takes the denominator and numerator of Eq. (4.22) as totally uncorrelated. This is not strictly true, but it provides a reasonable way of taking the statistical error in the polarization into account.

4.11.2 Systematic errors

Systematic errors are biases in a measurement which lead to the situation where, even though many separate measurements are combined, the result differs markedly from the

actual value of the measured attribute [44]. All measurements are prone to systematic errors, often of several different types. Sources of systematic errors may be uncertainties for determining solid angles, target thicknesses, energy calibration, electronic dead time, degree of polarization and gates on particle identification and energy spectra.

These systematic errors clearly affect the number of knockout events of interest and therefore the extracted cross sections and calculated analyzing power values.

These errors were assumed to be uncorrelated, consequently a more realistic approach to estimate of the total systematic error would be to add the individual errors in quadrature. In Table 4.5 are listed the systematic errors that are assumed to contribute to the cross section. Where applicable, some of these errors also apply to the analyzing power.

(i) Solid angle

The uncertainty in the solid angles arise from the uncertainties of determining the radius of the respective collimator openings, the distances between the target centre and the centre of exit collimator openings. The uncertainty in the solid angle is given by [47]

$$\frac{\Delta(\Delta\Omega)}{\Delta\Omega} = \left[\left(2\frac{\Delta r}{r} \right)^2 + \left(2\frac{\Delta D}{D} \right)^2 \right]^{1/2}. \quad (4.24)$$

From the uncertainties in the respective geometry parameters listed in Table 3.1, the uncertainties in the solid angles were found to be $\sim 0.65\%$ for telescope T1 and $\sim 0.9\%$ for telescope T2.

(ii) Degree of polarization

The uncertainty in the degree of polarization spin-up or down of the incident beam was in the range of 1.5– 2% (see Section 4.8).

(iii) Energy calibration

This uncertainty comes from the way of determining the peak position in the calibration detector spectrum, which consists of fitting a Gaussian to determine the centroid. Because of the energy resolution of the NaI detector, only the ground state and the first excited

state were taken into account in the calibration of the NaI detector. The final energy calibration was obtained after the effect of dead layer energy losses had been taken into account. The program used to calculate the energy loss, ELOSS, has a 2% accuracy [48]. The uncertainty in energy calibration eventually resulted in a combined error in the energy scale of a particular spectrum. The effect of this uncertainty on the absolute normalization of each energy-sharing distribution is estimated to be 4% [49].

(iv) Particle identification

The gates set in the different particle identification spectra could introduce some uncertainties if some protons or alphas might fall outside these gates. The uncertainty caused by the alpha gates was very small because of the mass function PID generated which clearly separated alphas from ^3He . However, in the case of the proton gate a larger uncertainty existed in the particle identification because of the reaction tails that might partially fall outside the PID gate. This uncertainty due to the setting of the gates in the PID constitutes an error of $\sim 5\%$.

(v) Energy spectrum gate

The ground state knockout locus in the two-dimensional total energy spectrum was not clearly separated from the first excited state knockout locus for most of the quasifree angle pairs. Three different types of gates were set in order to minimize the error. The choice of one instead of others introduced a systematic uncertainty in the data extracted. This was estimated to be about 5.5% in extracting the cross section value and 5% in calculating the analyzing power value at zero recoil momentum. The total uncertainty in setting the gate on the two-dimensional energy spectrum was therefore estimated to be about 5.5%.

(vi) Target thickness

The thicknesses of the carbon targets were measured with 8.78 MeV alpha particles from a ^{228}Th source. The energy loss of the alpha particles was measured by means of a Si surface-barrier detector. The target thickness was then calculated using range-energy curves for ^{228}Th [50]. The uncertainty in the target thickness was found to be less than 1%. The target uniformity was typically 1%/mm.

(vii) Subtraction of random coincidences

Sources of systematic errors	Error in (%)
Target thickness	< 1
T1 solid angle	0.65
T2 solid angle	0.9
Particle identification	5
Energy spectrum gate	5.5
Degree of polarization	< 2
Electronic dead time	< 2
Energy calibration	4
Random coincidences	3
Linear sum	24
Total systematic error	< 10

Table 4.5. *Summary of systematic errors.*

As described in Subsection 4.5.4, an error due to the inclusion of random coincidences was introduced in the experimental data. This error was determined from an average over several independent sets of data. It varied from 2% in the two-dimensional energy spectra where coincidence events were selected, to a maximum of 3%. We assign an overall uncertainty of 3% to this procedure.

Chapter 5

Results and Discussion

5.1 Overview

In this chapter the results of the experimental cross section and analyzing power measurements for the $^{12}\text{C}(p, p\alpha)^8\text{Be}$ knockout reaction to the ground state in ^8Be at an incident energy of 100 MeV are presented. Firstly, a comparison between experimental and theoretical results is made. Extracted spectroscopic factors are compared with values obtained from an earlier experiment and theoretical predictions. Secondly, the validity of the DWIA factorization approximation, used in the theory, is investigated through the comparison between knockout and elastic scattering, and the alpha-cluster momentum distribution. The issue of including or excluding spin-orbit terms in the distorting optical potentials and the sensitivity of cross section distributions to distorting potentials and bound state wave function are discussed. Finally, analyzing power angular distributions measured at the kinematic condition other than quasifree (non-zero recoil momentum) are also investigated.

In the DWIA calculations, the optical parameters for the two-body proton-cluster interaction were first taken from the work of Comparat *et al.* [51]. However these are not actually appropriate because they were derived from elastic cross section angular distribution only. However, an improved set of optical model parameters, adjusted to reproduce the experimental cross section as well as analyzing power observables from $p+^4\text{He}$ elastic scattering, was generated to reproduce both experimental distributions moderately well.

5.2 DWIA Calculations

In their previous work, Chant and Roos [35] observed that PWIA calculations were completely inadequate for the interpretation of $(p, p\alpha)$ reaction for which distortion effects were found to be large. Such PWIA calculations not only seriously overestimated cross sections, i.e. extracted spectroscopic factors were too small, but also underestimated the width of cross section distributions and predicted a pronounced minimum which was not observed experimentally. Because of these reasons, it has been decided to use only DWIA calculations to interpret our experimental data.

5.2.1 The effect of the two-body $\left. \frac{d\sigma}{d\Omega} \right|_{p-\alpha}$ off-shell cross section

As mentioned in Section 2.5.1 of Chapter 2, the two-body scattering amplitude which appeared as a multiplicative factor in the theoretical triple differential cross section when spin-orbit interactions in generating distorting potentials are neglected, is off-shell. This comes from the fact that the incoming particle is on-shell as its energy and momentum are related through the free-particle relation, and the bound particle is off-shell because of its interaction with the residual nucleus. Furthermore, because the alpha particle in the entrance channel is off the mass shell, there is some ambiguity in choosing the values of the centre-of-mass energy and angle of the two interacting particles to evaluate the two-body amplitude. This results in two energy prescriptions, namely the initial and final energy prescriptions. The differences between the two curves of two-body cross section, either considering the initial or final energy prescription, are found to be quite small (see Fig. 5.1). Nevertheless, the use of a half off-shell two-body cross section will merely decrease the calculated three-body DWIA cross section and increase the extracted spectroscopic factor for the knockout reaction discussed in the following section. Although it is possible to calculate the off-shell cross section, this requires an approximation in the treatment of the Coulomb interaction. We finally decided to make use of the two-body on-shell cross section corresponding to the final two-body energy. This arbitrary choice is discussed and motivated by Roos *et al.* [1].

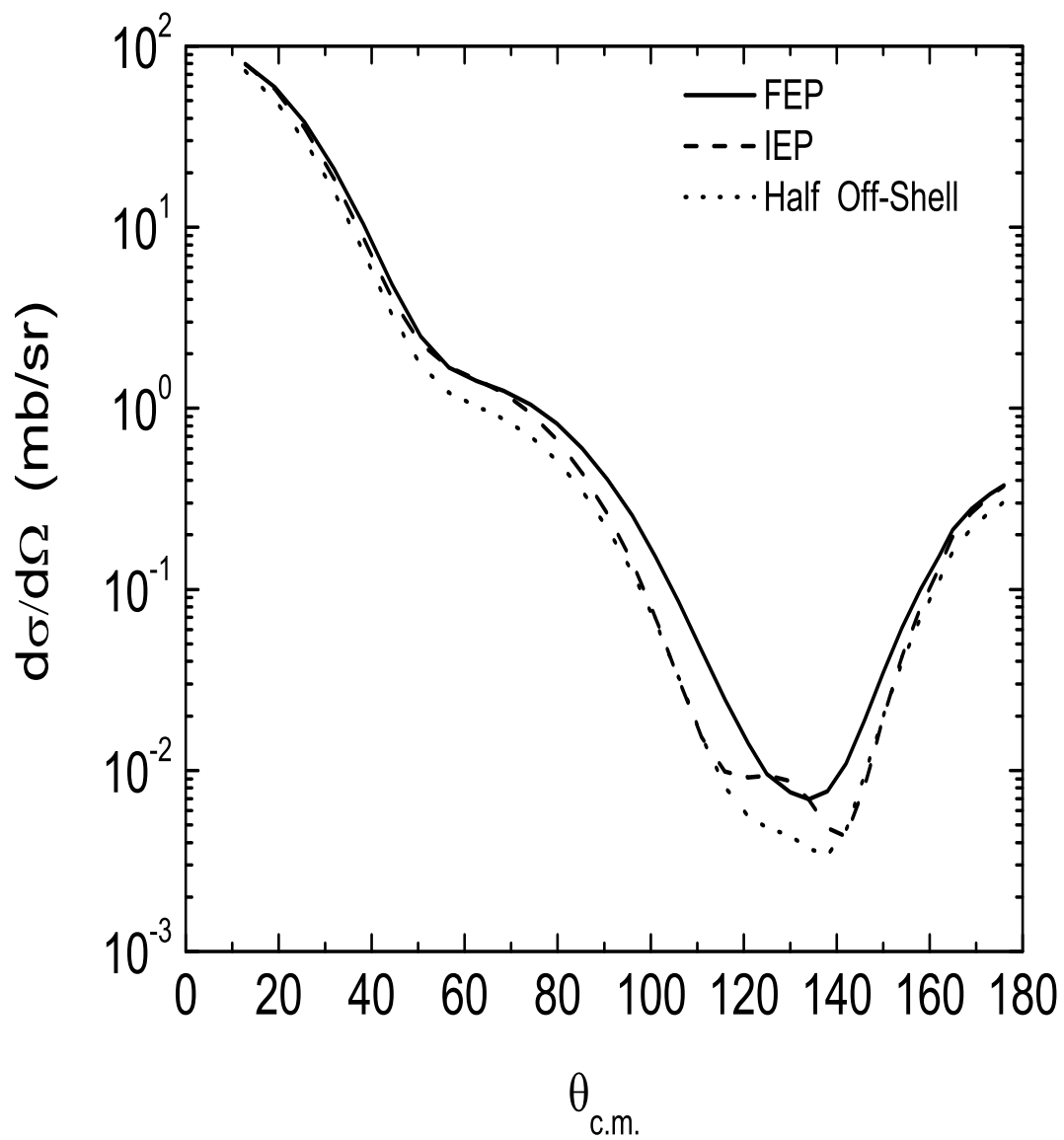


Figure 5.1. Comparison of the on-shell p - α cross sections calculated from the final (FEP) and initial (IEP) energy prescriptions, and the half off-shell cross section.

5.2.2 Optical model potentials

Optical model parameter sets for the distorted waves and bound state wave function were taken from references listed in Table 5.1. Note that since our calculations were not restricted to a factorized DWIA formalism, spin-orbit terms were included in the distorted waves.

The two-body proton-cluster system potential parameters were first taken from the work of Comparat *et al.* [51] (with the *imaginary* spin-orbit potential strength set to zero), whereby we found that the DWIA prediction of the analyzing power followed the trend of the experimental values only qualitatively (shown later in Fig. 5.10). However, improved set of parameters were obtained by adjusting the set of Comparat *et al.* in order to get a better agreement between $p+{}^4\text{He}$ elastic scattering and ${}^{12}\text{C}(p, p\alpha){}^8\text{Be}$ knockout reaction cross section as well as analyzing power angular distributions. These parameter sets were used for the rest of the discussion.

5.3 Experimental Results

Cross sections and analyzing powers were measured at ten coplanar angle pairs $(\theta_p, \theta_\alpha)$ ranging from $(25^\circ, -68.8^\circ)$ to $(110^\circ, -26.6^\circ)$ (Table 5.2). These angles were chosen to permit zero recoil momentum of the undetected nucleus ${}^8\text{Be}$.

5.3.1 Energy-sharing cross section and analyzing power distributions

Energy-sharing cross section and analyzing power distributions, i.e., triple differential cross sections and analyzing powers for ${}^{12}\text{C}(p, p\alpha){}^8\text{Be}$ knockout reaction, plotted as functions of the kinetic energy of the detected proton, are shown in Figs. 5.2–5.6 for the ten ¹ angle pairs. The error bars on each data point represent statistical uncertainties only. We find that most of the cross section distributions are characterized by a smooth broad

¹For better display only results of nine angle pairs are shown in Figs. 5.2–5.5; results of the largest proton angle are displayed in Fig. 5.6

System	Set	V_R	r_R	a_R	r_c	W_V	W_S	r_I	a_I	V_{so}	W_{so}	r_{so}	a_{so}	V_{ex}	r_{ex}	a_{ex}	Ref.
$p+^{12}\text{C}$	I	21.2	1.33	0.65	1.33	6.5	0.0	1.46	0.44	3.86	0.0	0.85	0.43				[52]
	II	22.6	1.25	0.55	1.33	4.4	0.0	1.91	0.21	4.30	0.0	0.96	0.49				[52]
	III	21.6	1.30	0.51	1.33	0.0	5.4	1.40	0.52	3.30	0.0	0.97	0.40				[52]
$p+^8\text{Be}$	I	32.3	1.26	0.63	1.30	0.0	2.3	1.31	0.96	4.90	0.0	1.20	0.56				[53]
	II	38.3	1.18	0.62	1.30	3.6	1.0	1.69	0.96	5.60	0.0	1.10	0.58				[53]
	III	38.3	1.20	0.61	1.30	4.8	0.0	1.79	0.66	4.90	0.0	1.12	0.56				[53]
$^4\text{He}+^8\text{Be}$	I	88.9	0.99	0.81	1.20	4.9	0.0	3.01	0.58								[54]
	II	94.6	0.97	0.73	1.20	3.05	2.3	2.9	0.48								[54]
	III	65.9	1.48	0.65	1.20	34.9	0.0	1.06	1.05								[54]
$p+^4\text{He}$	I	13.1	1.53	0.10	1.23	0.0	8.8	1.34	0.40	7.53	0.0	0.74	0.36	-10.24	0.13	0.7	[51]
	II	16.3	1.53	0.5	1.36	4.5	4.0	1.7	0.30	10.5	-2.4	0.88	0.26	-10.24	0.13	0.7	[4]
Bound state		89.9	1.23	0.75	1.23												[1]

Table 5.1: Optical potential parameters. All optical potential depths are in MeV and all lengths are in fm. Set II of $p+^4\text{He}$ optical potential parameters reported in Ref. [4] are from this work.

θ_p/θ_α (deg)	$\theta_{p-\alpha}^{c.m.}$ (deg)	$d^3\sigma/d\Omega_p d\Omega_\alpha dE_p$ (mb sr ⁻² MeV ⁻¹)	A_y
25/-68.8	31.9	$(1.35 \pm 0.054) \times 10^{-1}$	0.39 ± 0.03
30 /-66.6	38.2	$(1.52 \pm 0.046) \times 10^{-1}$	0.43 ± 0.04
37.0/-63.1	46.8	$(1.36 \pm 0.073) \times 10^{-1}$	0.24 ± 0.04
52.0/-55.1	64.9	$(1.66 \pm 0.741) \times 10^{-2}$	-0.11 ± 0.06
60.0/-50.9	74.1	$(1.82 \pm 0.106) \times 10^{-2}$	-0.39 ± 0.09
70.0/-45.6	85.3	$(1.70 \pm 0.051) \times 10^{-2}$	-0.26 ± 0.04
80.0/-40.5	96.0	$(0.89 \pm 0.035) \times 10^{-2}$	-0.55 ± 0.06
90.0/-35.7	106.2	$(4.06 \pm 0.200) \times 10^{-3}$	-0.41 ± 0.07
100.0/-31.0	115.9	$(3.15 \pm 0.311) \times 10^{-3}$	-0.16 ± 0.14
110.0/-26.6	125.2	$(4.31 \pm 0.440) \times 10^{-4}$	0.22 ± 0.14

Table 5.2. Angle pairs, two-body centre-of-mass scattering angle, measured cross section and analyzing power values at the quasifree peak.

distribution reaching a maximum near the energy corresponding to zero recoil momentum for the residual nucleus, showing clearly that the reaction is dominated by a quasifree α -cluster knockout. However, we noticed that from $\theta_p = 70^\circ$ to $\theta_p = 110^\circ$, contributions, that are probably due to sequential α -particle emission after target excitation, can be seen at higher proton energies².

The DWIA calculations were performed using the sets labeled I in Table 5.1 of the distorting potentials and bound state wave functions (and $p+^4\text{He}$ for either set I of Comparat *et al.* or set II from this work), which give a fairly good reproduction of the experimental energy-sharing cross section distributions, except at proton energies below approximately 40 MeV for the three smallest proton angles. The analyzing power distributions, on the other hand, are not well reproduced by DWIA calculations from $\theta_p = 25^\circ$ to $\theta_p = 52^\circ$ for the two $p+^4\text{He}$ potential sets. For the $p+^4\text{He}$ parameter set of Comparat *et al.*, for example, this is because of the poor agreement between experimental and theoretical analyzing power distribution as shown in Fig. 5.10. However, one should keep in mind that these energy-sharing analyzing power distributions offer a very sensitive test, and it draws attention to a proton energy range far from zero recoil momentum where the energy-sharing cross section distributions are also poorly reproduced by the DWIA calculations.

²Note that the dips in the cross section distributions at ~ 75 MeV at the three smallest proton angles are artefacts of the matching condition for α -particles that are either stopped in the ΔE detector or not.

θ_p/θ_α (deg)	S_α	$\langle S_\alpha \rangle^{exp}$	S_α^{theory} (Ref. [55])	$\langle S_\alpha \rangle^{exp}$ (Ref. [1])
25/-68.8	1.04			
30/-66.6	1.58			
37/-63.1	1.58			
52/-55.1	0.44			
60/-50.9	0.44	0.89 ± 0.49	0.56	0.59 ± 0.05
70/-45.6	0.63			
80/-40.5	0.57			
90/-35.7	0.63			
100/-31.0	1.52			
110/-26.6	0.47			

Table 5.3. Spectroscopic factors for quasifree angle pairs extracted using the set I in Table 5.1 of $p+^4\text{He}$ potential parameters. $\langle S_\alpha \rangle^{exp}$ is a statistical average of all angles.

In Fig. 5.7 the present cross section data at $\theta_p/\theta_\alpha = 90^\circ / -35.7^\circ$ are compared with data of the previous work of Roos *et al.* [1]. It is clearly seen in the left-hand panel plot that the difference is approximately 17%. This is within the combined systematic uncertainty of both experiments. The right-hand panel of Fig. 5.7 shows the plotted cross section data of Roos *et al.* [1] and the data of this experiment normalized to the difference of 17%.

5.3.2 Spectroscopic factors

The spectroscopic factors S_α were extracted by normalizing the DWIA calculations to the experimental data. The values of spectroscopic factors are presented in Tables 5.3 and 5.4 for each quasifree angle pair.

Large variations are found in the extracted spectroscopic factors for different angle pairs, but there is no systematic trend. We assign an estimated error to the average value by calculating the standard deviation. Note that the average spectroscopic value obtained in both parametrizations are consistent with both the shell model prediction [55] and the average value extracted by Roos *et al.* [1] for the same type of experiment, suggesting a good agreement between experiment and theory on the α -cluster preformation probability.

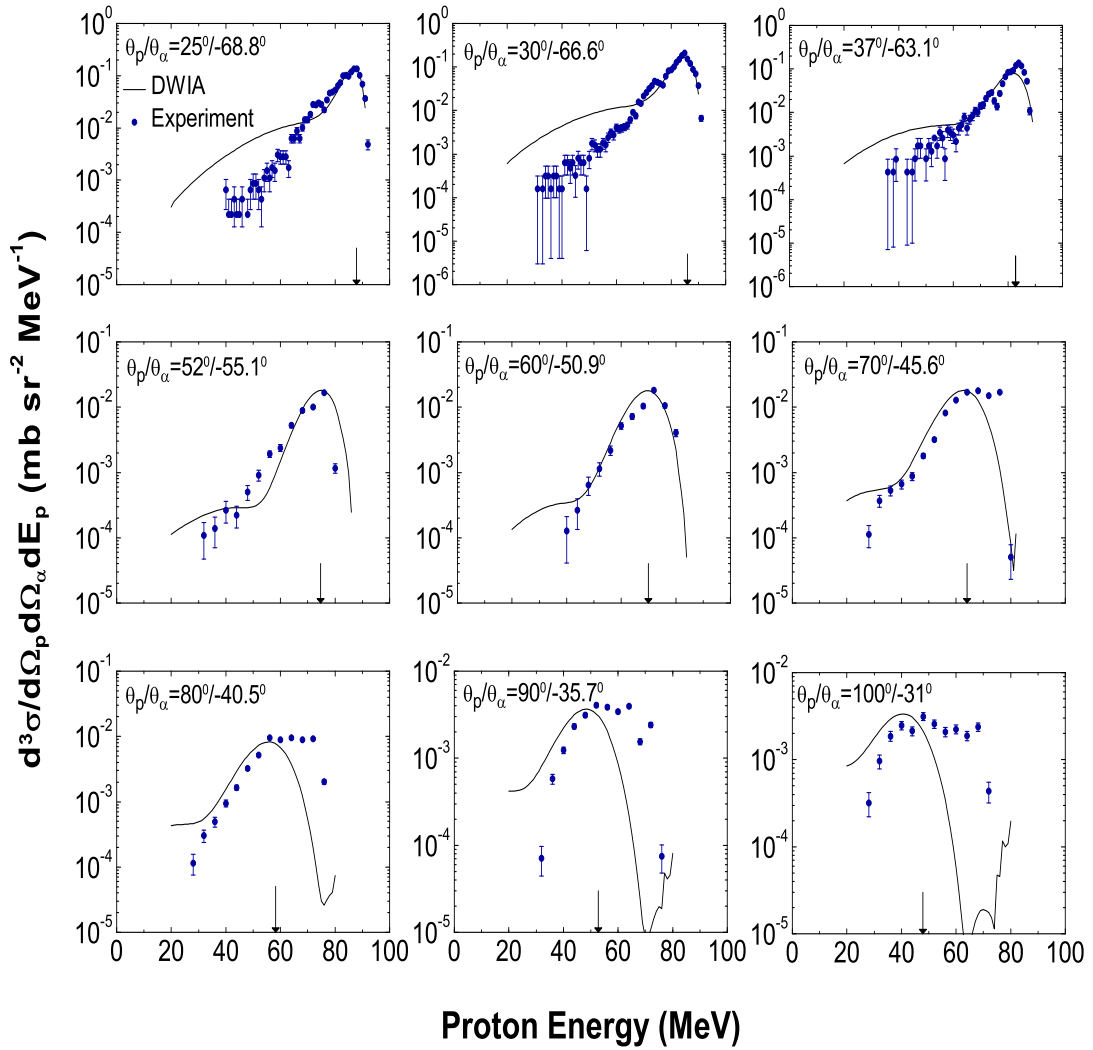


Figure 5.2. Cross section distributions projected onto the proton energy axis for the reaction $^{12}\text{C}(p, p\alpha)^8\text{Be}(g.s.)$. Statistical error bars on the experimental values are indicated. The curves represent results of DWIA calculations with the distorting potentials set I and $p\text{-}^4\text{He}$ potential set I in Table 5.1. Spectroscopic factors for the theoretical cross section distributions are listed in Table 5.3. The proton energy which corresponds to zero recoil momentum of the residual nucleus is indicated with an arrow for each angle pair.

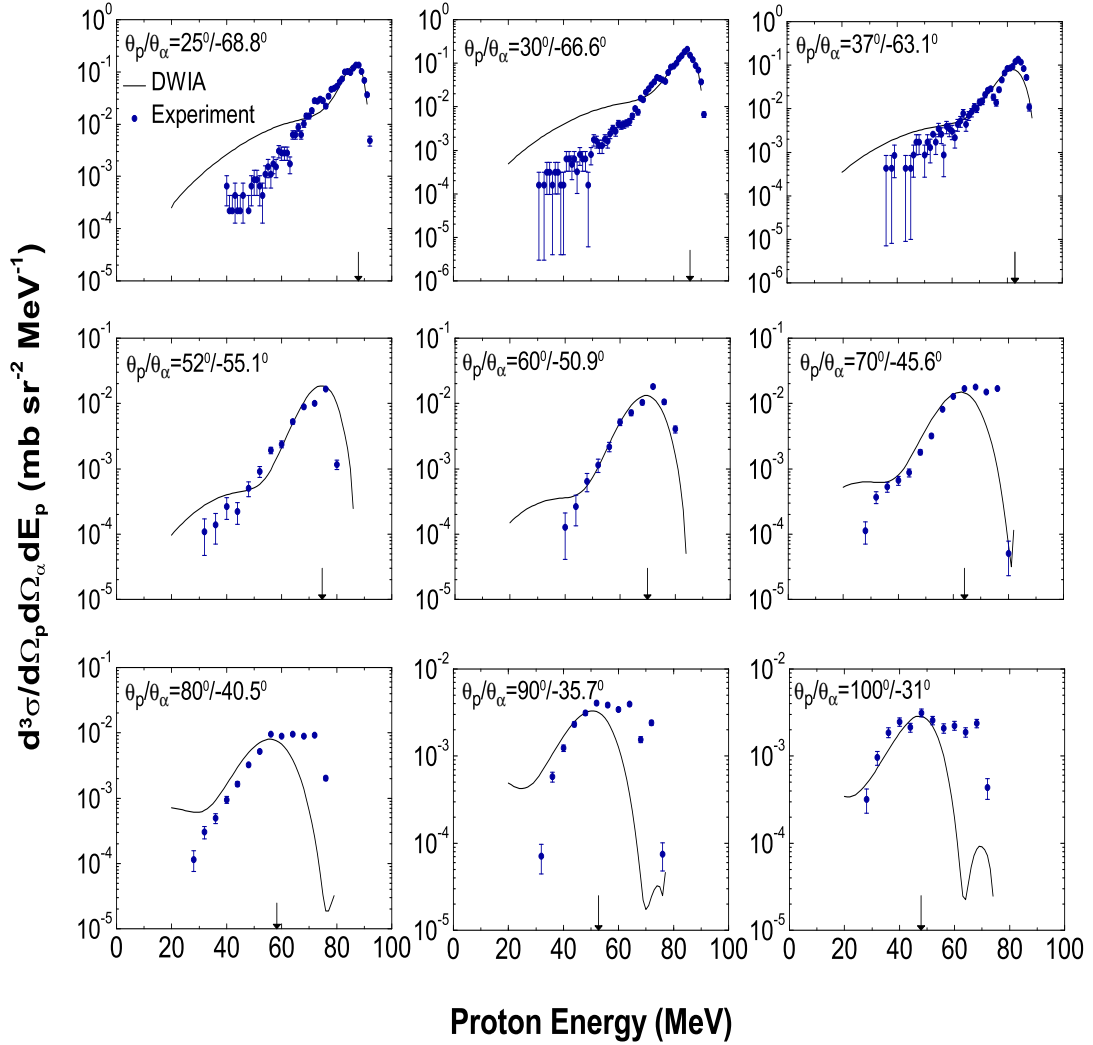


Figure 5.3. Cross section distributions projected onto the proton energy axis for the reaction $^{12}\text{C}(p, p\alpha)^8\text{Be}(g.s.)$. Statistical error bars on the experimental values are indicated. The curves represent results of DWIA calculations with the distorting potentials set I and p - ^4He potential set II in Table 5.1. Spectroscopic factors for the theoretical cross section distributions are listed in Table 5.4. The proton energy which corresponds to zero recoil momentum of the residual nucleus is indicated with an arrow for each angle pair.

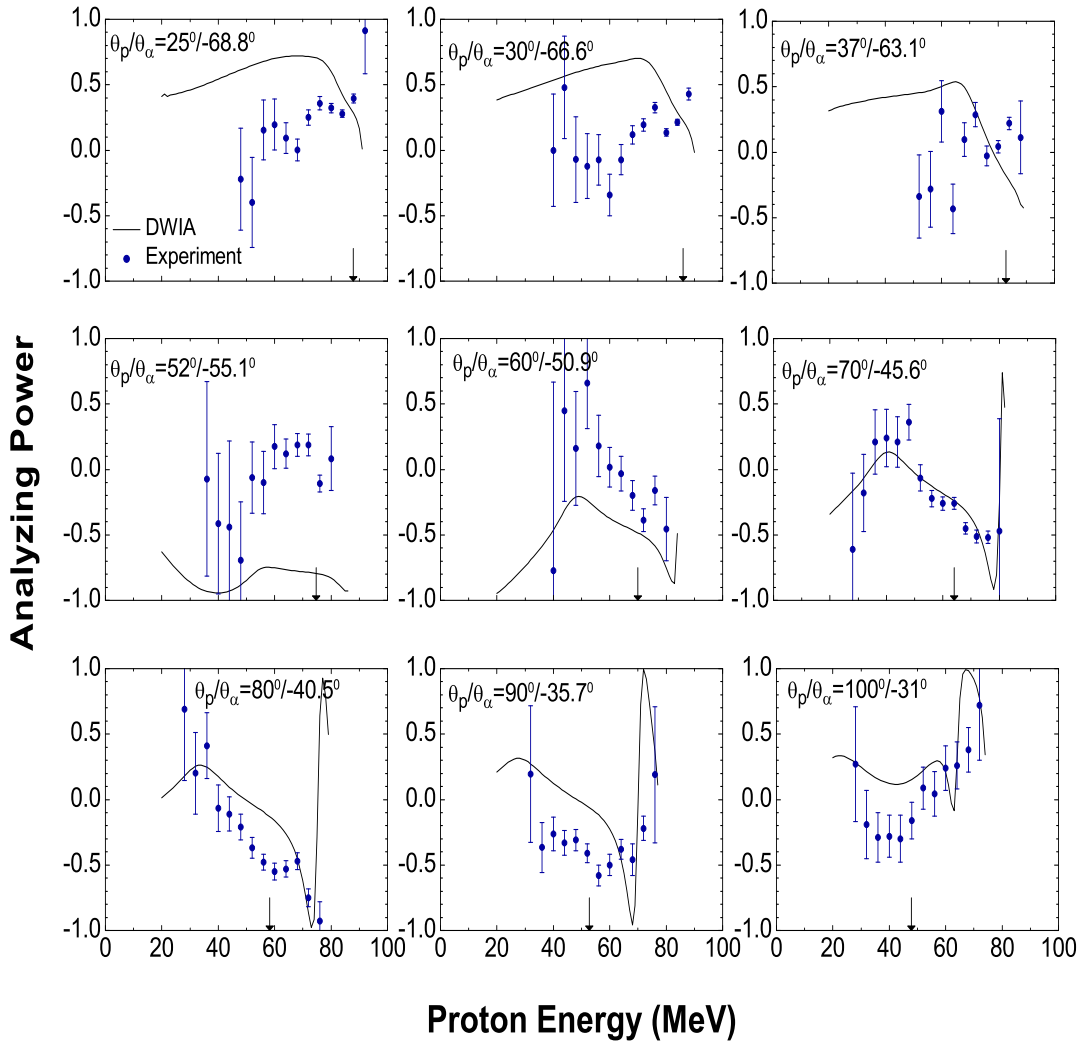


Figure 5.4. Analyzing power distributions projected onto the proton energy axis for the reaction $^{12}\text{C}(p, p\alpha)^8\text{Be}(g.s.)$. Statistical error bars on the experimental values are indicated. The curves represent results of DWIA calculations with the distorting potentials set I and p - ^4He potential set I in Table 5.1. The proton energy which corresponds to zero recoil momentum of the residual nucleus is indicated with an arrow for each angle pair.

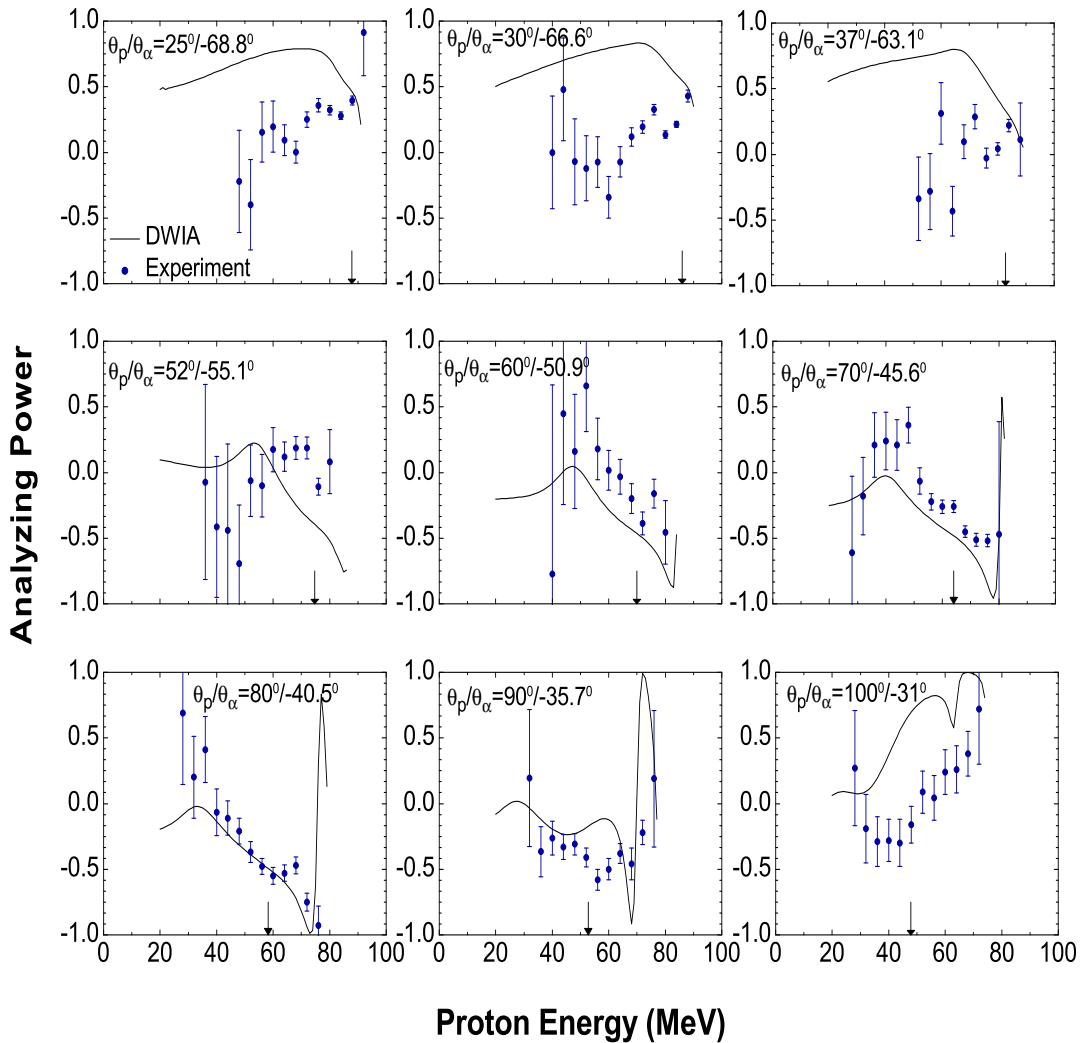


Figure 5.5. Analyzing power distributions projected onto the proton energy axis for the reaction $^{12}\text{C}(p, p\alpha)^8\text{Be}(g.s.)$. Statistical error bars on the experimental values are indicated. The curves represent results of DWIA calculations with the distorting potentials set I and p - ^4He potential set II in Table 5.1. The proton energy which corresponds to zero recoil momentum of the residual nucleus is indicated with an arrow for each angle pair.

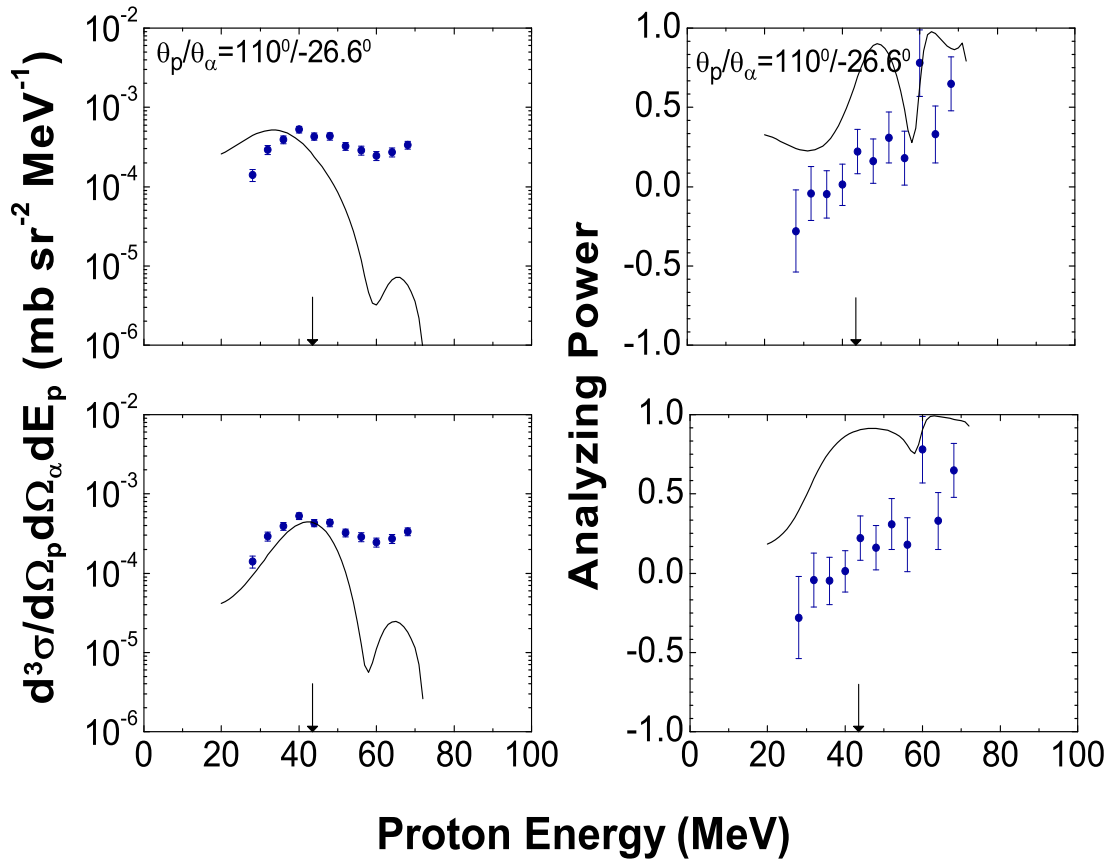


Figure 5.6. Cross section and analyzing power distributions projected onto the proton energy axis for the reaction $^{12}\text{C}(p, p\alpha)^8\text{Be}(g.s.)$ at $\theta_p/\theta_\alpha = 110^\circ/-26.6^\circ$. The curves represent results of DWIA calculations, with distorting and $p\text{-}^4\text{He}$ potentials of respectively sets I and I (top panels) and sets I and II (bottom panels). Spectroscopic factors for the theoretical cross section distributions are listed in Tables 5.3 and 5.4. The proton energy which corresponds to zero recoil momentum of the residual nucleus is indicated with an arrow.

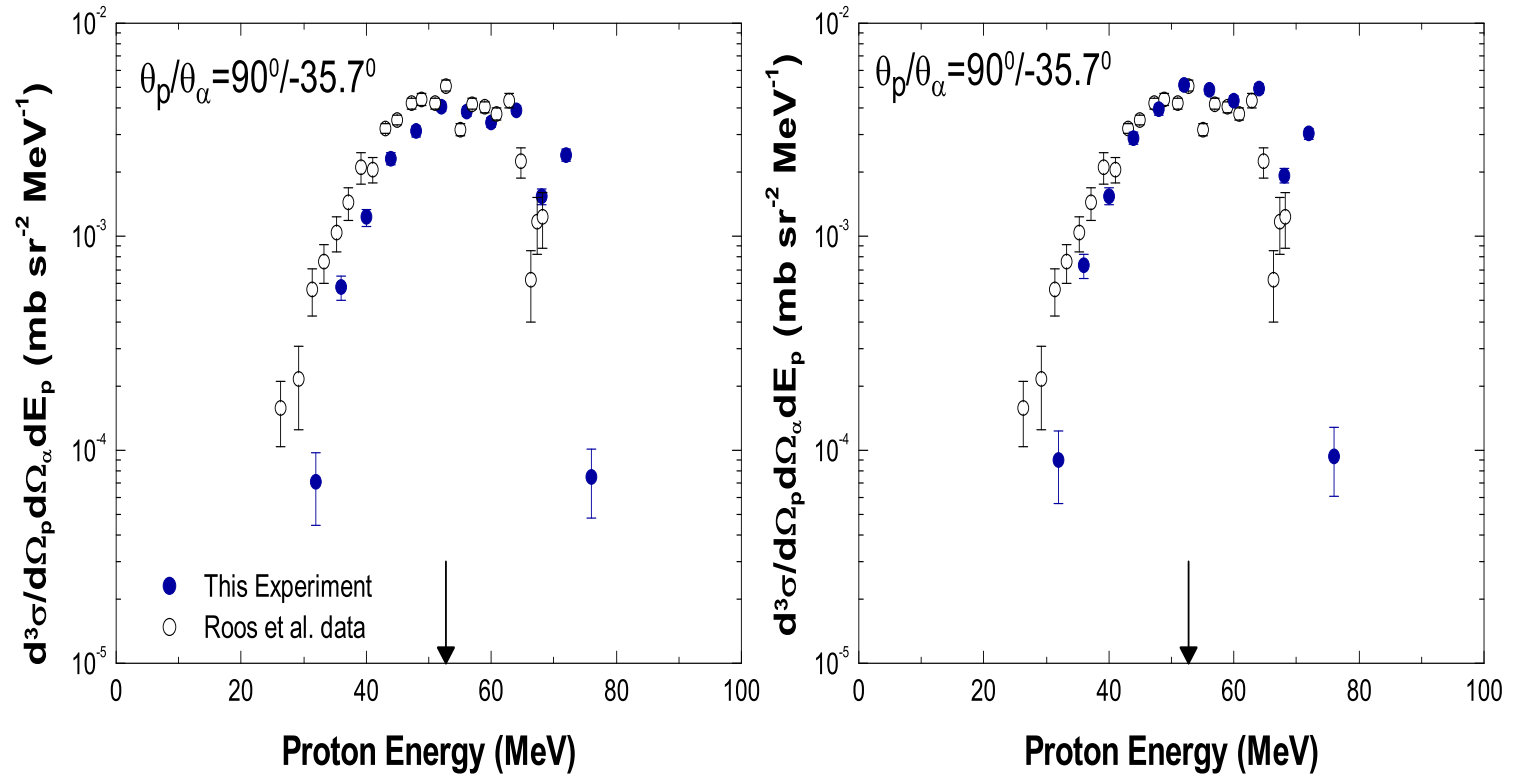


Figure 5.7: Comparison of energy-sharing cross section distributions for the reaction at $\theta_p/\theta_\alpha = 90^\circ / -35.7^\circ$ (left-hand panel). The open circles represent the data obtained in the previous work of Roos et al. [1] and the filled circles denote the data of this work. In the right-hand panel the cross section data of Roos et al. [1] and the data of this experiment normalized to the difference of 17% are shown.

θ_p/θ_α (deg)	S_α	$\langle S_\alpha \rangle^{exp}$	S_α^{theory} (Ref. [55])	$\langle S_\alpha \rangle^{exp}$ (Ref. [1])
25/-68.8	0.59			
30/-66.6	0.93			
37/-63.1	0.65			
52/-55.1	0.19			
60/-50.9	0.20	0.73 ± 0.49	0.56	0.59 ± 0.05
70/-45.6	0.55			
80/-40.5	0.98			
90/-35.7	1.28			
100/-31.0	1.68			
110/-26.6	0.28			

Table 5.4. Spectroscopic factors for quasifree angle pairs extracted using the set II in Table 5.1 of $p+{}^4\text{He}$ potential parameters. $\langle S_\alpha \rangle^{exp}$ is a statistical average of all angles.

5.4 Tests of the Reaction Mechanism: DWIA Factorization

In DWIA calculations, when spin-orbit terms are excluded in the distorting potentials, the triple differential cross section may be written in the factorized form [1]

$$\frac{d^3\sigma}{d\Omega_p d\Omega_\alpha dE_p} = F_K S_\alpha \left\{ \sum_\Lambda |T_{BA}^{\alpha L \Lambda}|^2 \right\} \frac{d\sigma}{d\Omega} \Big|_{p-\alpha}, \quad (5.1)$$

where F_K is a kinematic factor, S_α is a spectroscopic factor for the α cluster, and $\frac{d\sigma}{d\Omega} \Big|_{p-\alpha}$ is a half-shell two-body cross section for $p-\alpha$ scattering. The quantity $\sum_\Lambda |T_{BA}^{\alpha L \Lambda}|^2$ is a distorted momentum distribution for an α cluster in the target ${}^{12}\text{C}$.

5.4.1 Comparison between knockout and elastic scattering

Following Eq. (5.1), it is thus appropriate to construct the quantity

$$\left[\frac{d^3\sigma}{d\Omega_p d\Omega_\alpha dE_p} \right]_{exp} / F_K \left\{ \sum_\Lambda |T_{BA}^{\alpha L \Lambda}|^2 \right\} = S_\alpha \frac{d\sigma}{d\Omega} \Big|_{p-\alpha}, \quad (5.2)$$

where $\left[\frac{d^3\sigma}{d\Omega_p d\Omega_\alpha dE_p} \right]_{exp}$ now represents the $^{12}\text{C}(p, p\alpha)^8\text{Be}$ experimental cross section value. At the quasifree peak at which zero recoil momentum is kinematically allowed, the quantity on the left-hand-side of Eq. (5.2) is expected to be proportional to the free two-body p - ^4He cross section.

This comparison is made in Fig. 5.8 for the two-body $p+^4\text{He}$ optical model parameters of Ref. [51] and in Fig. 5.9 for the optical model parameter set of Mabilia *et al.* [4]. The solid line represents the free two-body p - α cross sections obtained with DWIA calculations, the filled and open circles represent, respectively, p - α cross sections extracted from the $^{12}\text{C}(p, p\alpha)^8\text{Be}$ reaction and corrected for distortion effects and, measured p - α elastic scattering at 100 MeV [56]. Overall, the results of this comparison are very good and indicate that the factorization approximation works very well over the whole angular range. This suggests that spin-orbit interactions in distorting potentials have a negligible effect on the convolution of the DWIA cross section.

A more direct and sensitive test of the factorization is to compare the coincident $^{12}\text{C}(p, p\alpha)^8\text{Be}$ experimental analyzing power distribution as a function of the centre-of-mass two-body scattering angle, directly with free scattering. Recall that the analyzing power for the knockout reaction $^{12}\text{C}(p, p\alpha)^8\text{Be}$ reaction is defined as

$$A_{p,p\alpha} = \frac{\sigma^\uparrow - \sigma^\downarrow}{\sigma^\uparrow + \sigma^\downarrow} \quad (5.3)$$

where $\sigma^{\uparrow(\downarrow)} \equiv \left[\frac{d^3\sigma}{d\Omega_p d\Omega_\alpha dE_p} \right]^{\uparrow(\downarrow)}$ as defined in Eq. (2.36) of Chapter 2 and arrows hold for spin directions of the projectile. Note that $A_{p,p\alpha}$ is equal to the free p - ^4He analyzing power if $\{\sum_\Lambda |T_{BA}^{\alpha L\Lambda}|^2\}^\uparrow = \{\sum_\Lambda |T_{BA}^{\alpha L\Lambda}|^2\}^\downarrow$. Therefore, this result will be true if only the cluster displays a major response to the spin direction of the projectile. In Figs. 5.10 and 5.11 the comparison between the knockout and elastic scattering analyzing power distributions displayed as functions of the two-body centre-of-mass p - α scattering angle for the two sets of $p+^4\text{He}$ optical model parameters is shown. Clearly, the experimental $(p, p\alpha)$ analyzing power data agree with the free p - ^4He data [2] to a remarkable degree. Furthermore, the full DWIA theory, i.e., without the factorization approximation reproduces very well the experimental angular distribution of the analyzing power for the knockout reaction by

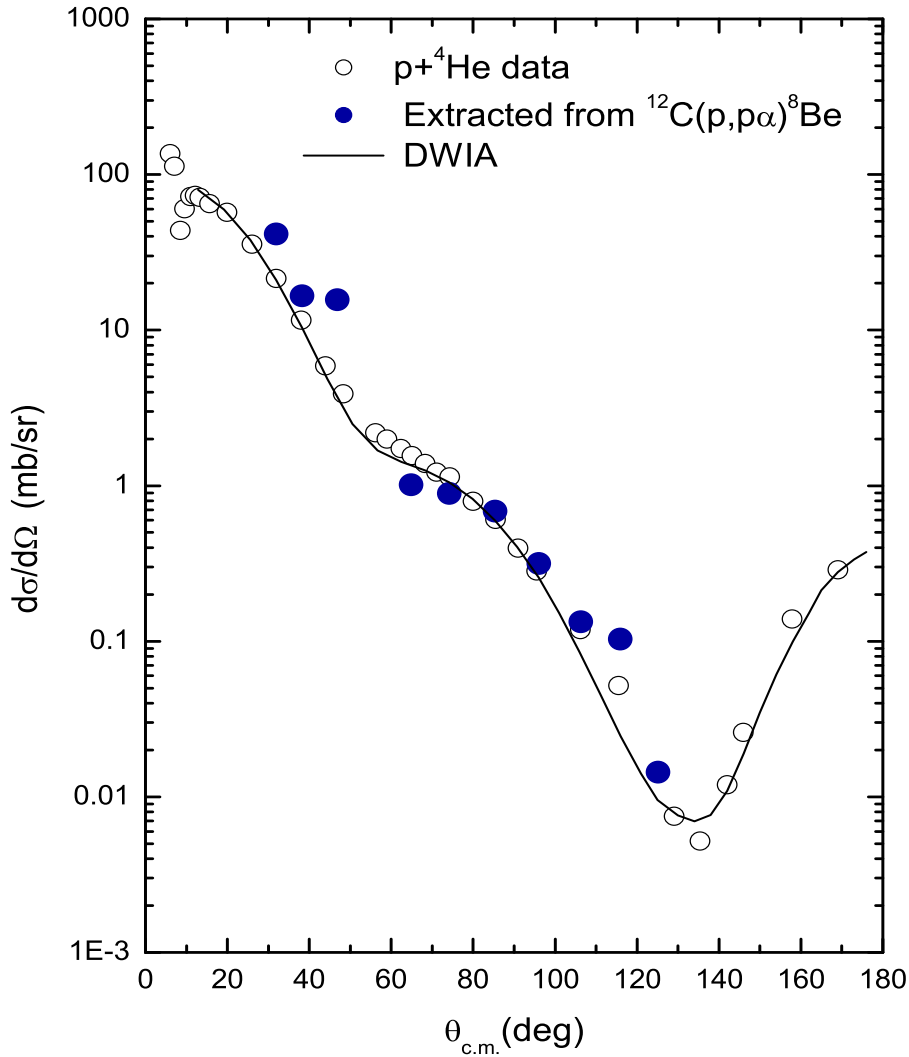


Figure 5.8. Two-body cross section values (filled circles) as a function of the centre-of-mass scattering angle extracted from the experimental ${}^{12}\text{C}(p,p\alpha){}^8\text{Be}(g.s.)$ cross sections at the quasifree peak (zero recoil momentum), compared with free $p+{}^4\text{He}$ elastic scattering data (open circles) and predictions of a factorized DWIA theory (curve). The average spectroscopic factor listed in Table 5.3 was used. The optical model parameters for $p+{}^4\text{He}$ used in the DWIA are from set I of Table 5.1.

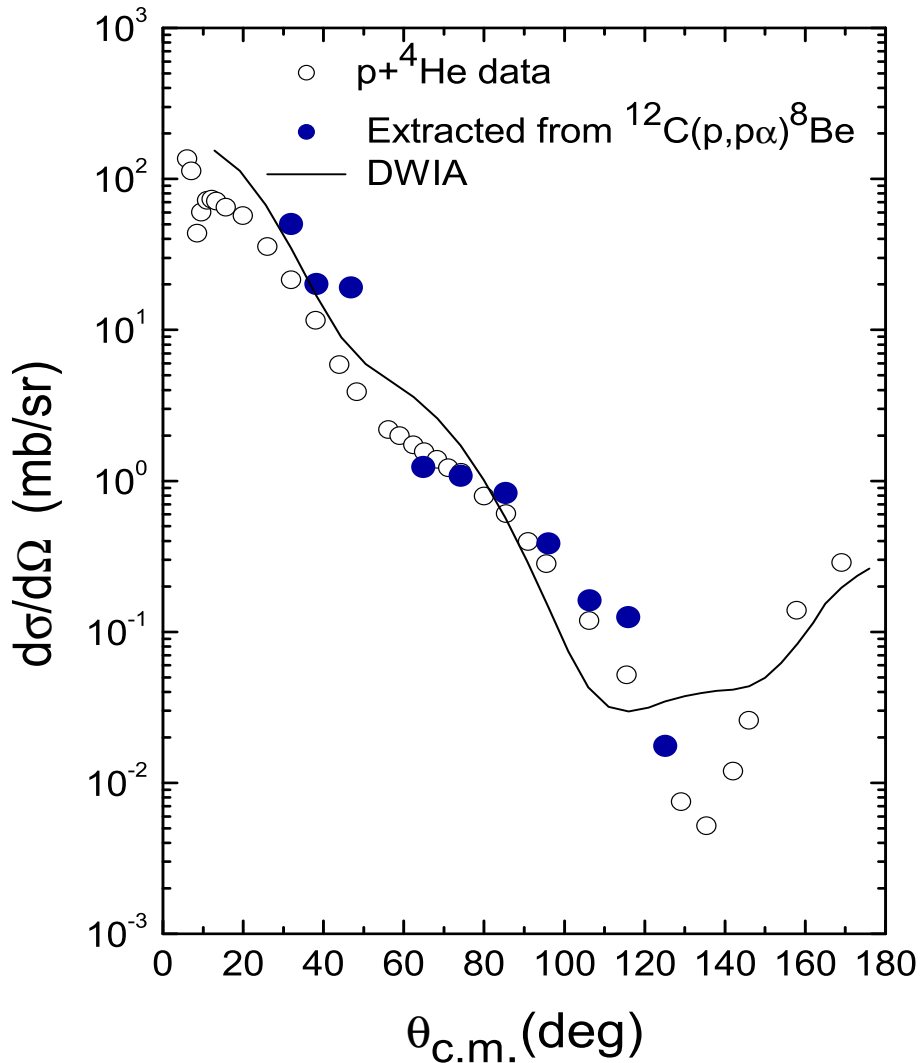


Figure 5.9. Two-body cross section values (filled circles) as a function of the centre-of-mass scattering angle extracted from the experimental ${}^{12}\text{C}(p,p\alpha){}^8\text{Be}(g.s.)$ cross sections at the quasifree peak (zero recoil momentum), compared with free $p+{}^4\text{He}$ elastic scattering data (open circles) and predictions of a factorized DWIA theory (curve). The average spectroscopic factor listed in Table 5.4 was used. The optical model parameters for $p+{}^4\text{He}$ used in the DWIA are from set II of Table 5.1.

using the set II of $p+^4\text{He}$ optical model parameters obtained in this work. This is because such a set was obtained by fitting together experimental $p+^4\text{He}$ cross section and analyzing power distribution data.

5.4.2 Alpha-cluster momentum distributions

A second test of the reaction mechanism, assuming distortion effects to be relatively constant with angle, is a comparison of the shapes of the experimental spectra for different angle pairs. In Chapter 2, we have seen that in the factorized DWIA formalism, the expression for the triple differential cross section for the $A(p, p\alpha)B$ reaction obtained in PWIA calculations is preserved [1]

$$\frac{d^3\sigma}{d\Omega_p d\Omega_\alpha dE_p} = F_K \{S_\alpha |\phi(-\vec{p}_B)|^2\} \left. \frac{d\sigma}{d\Omega} \right|_{p-\alpha}, \quad (5.4)$$

where only the $|\phi|^2$ term of the PWIA expression is replaced by the distorted momentum distribution

$$|\phi(-\vec{p}_B)|^2 \equiv \sum_{\Lambda} |T_{BA}^{\alpha L \Lambda}|^2. \quad (5.5)$$

The Eq. (5.4) may then be written as

$$\left[\frac{d^3\sigma}{d\Omega_p d\Omega_\alpha dE_p} \right]_{exp} / \left\{ F_K \left. \frac{d\sigma}{d\Omega} \right|_{p-\alpha} \right\} = \{S_\alpha |\phi(-\vec{p}_B)|^2\}, \quad (5.6)$$

in order to obtain the distorted momentum distribution, which may be plotted versus the recoil momentum \vec{p}_B . In the PWIA this quantity simply represents the Fourier transform of the α -cluster wave function, and is therefore independent of angle. In Figs. 5.12 and 5.13 the results are plotted as a function of the recoil momentum. It has been found that the distorted momentum distributions at the angle pairs studied are in excellent agreement with each other on the low-momentum side, in spite of the fact that the energy-sharing distributions are very different. This result confirms the validity of the impulse approximation, which relates the momentum of the bound α -cluster to the recoil of the residual nucleus. The difference at the top positive momentum range in Fig. 5.13 is almost

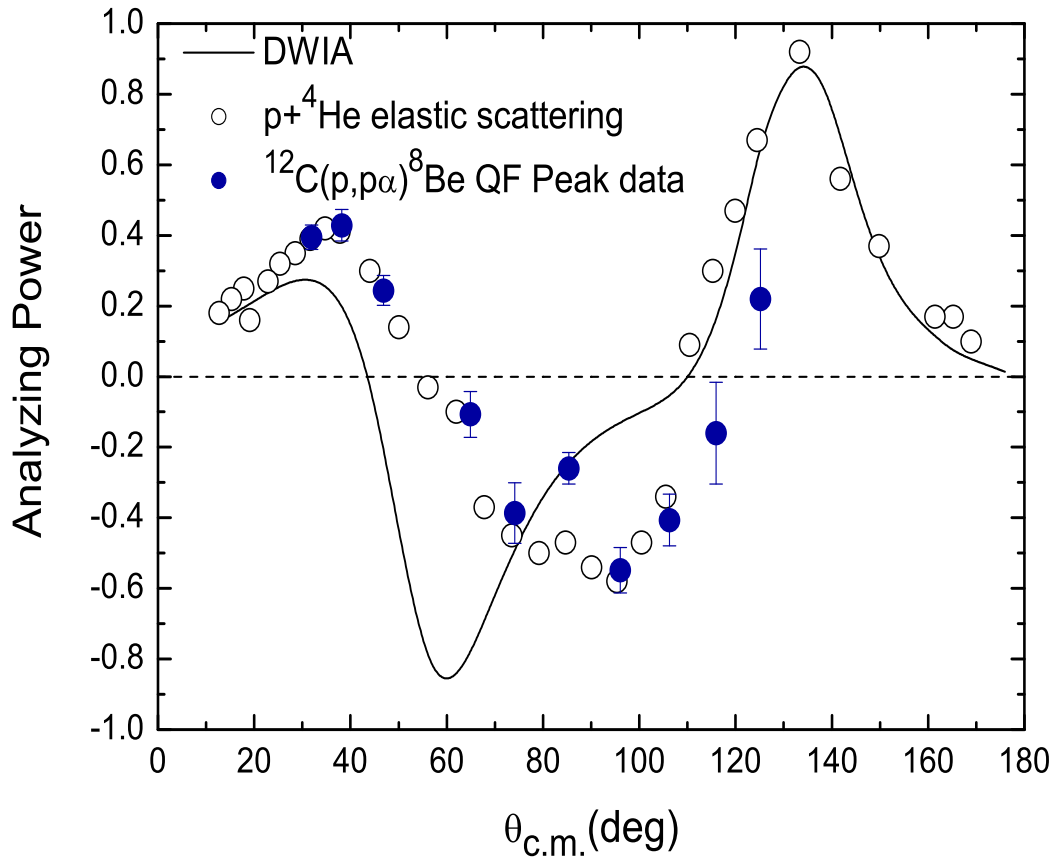


Figure 5.10. Analyzing power distribution for the $^{12}\text{C}(p, p\alpha)^8\text{Be}(g.s.)$ reaction displayed as a function of the two-body centre-of-mass p - α scattering angle. Experimental values at the quasifree peak are represented by filled circles with statistical error bars and open circles correspond to free p - ^4He elastic scattering data of Ref. [2]. The solid curve represents the result of an unfactorized DWIA calculation performed using set I of p - ^4He optical model parameters in Table 5.1.

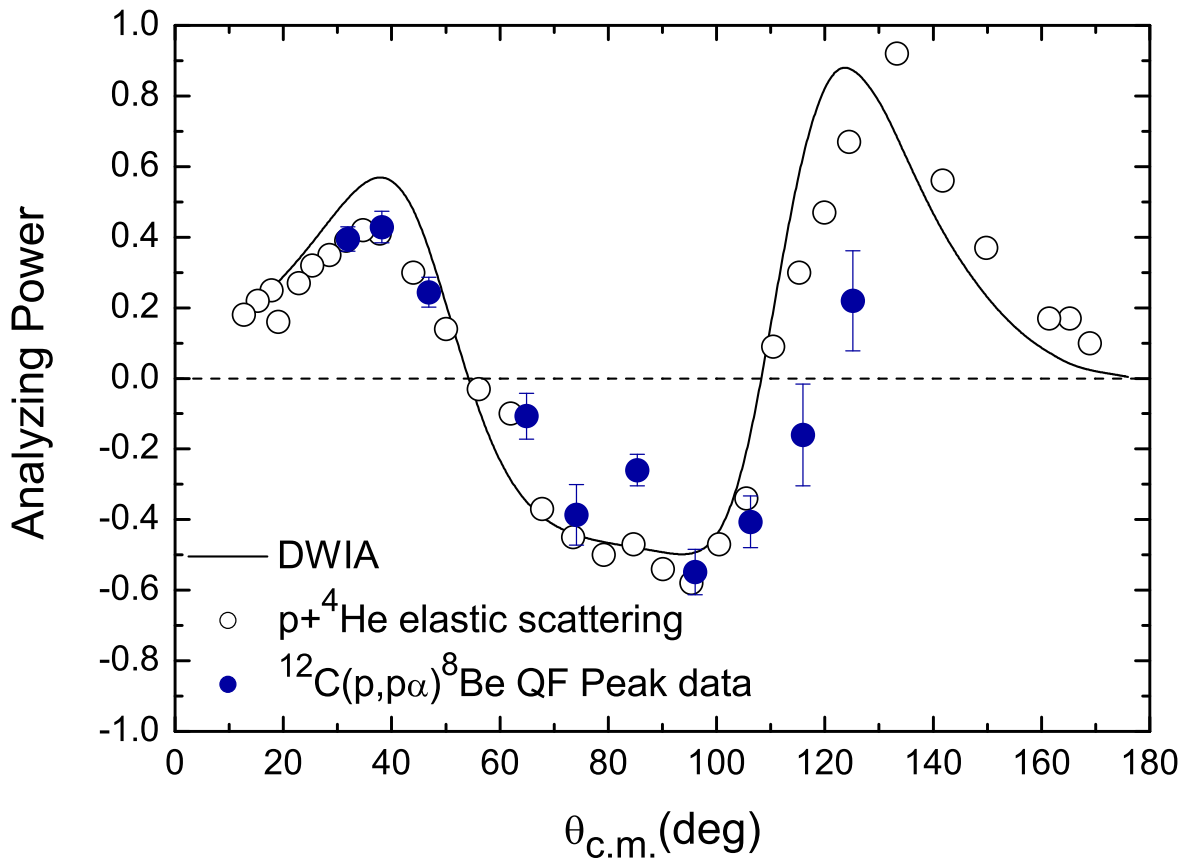


Figure 5.11. Analyzing power distribution for the $^{12}\text{C}(p, p\alpha)^8\text{Be}(g.s.)$ reaction displayed as a function of the two-body centre-of-mass p - α scattering angle. Experimental values at the quasifree peak are represented by filled circles with statistical error bars and open circles correspond to free p - ^4He elastic scattering data of Ref. [2]. The solid curve represents the result of an unfactorized DWIA calculation performed using set II of p - ^4He optical model parameters in Table 5.1.

certainly ascribable to sequential α -particle decay [1] at the large proton emission angle. This hypothesis is supported by the fact that the momentum distribution for $\theta_p = 37^\circ$ is fairly symmetric around zero momentum, as would normally be expected.

5.4.3 Spin-orbit effects on analyzing power angular distribution

We have also investigated the sensitivity of the analyzing power angular distribution to the spin-orbit interaction in order to test the factorization approximation. Fig. 5.14 shows the comparison of analyzing power angular distributions obtained by, respectively, considering and setting spin-orbit terms of the distorting potentials in set I to zero. The influence of the spin-orbit interaction is clearly very small. Other potential combinations gave also similar results. This result confirms the conclusion drawn in Subsection 5.4.1 and also validates the so-called DWIA factorization approximation of the reaction mechanism.

5.5 Sensitivity to Distorting Potentials and Bound State Wave Function of Cross Section Distributions

We have investigated the influence of the optical model potential parameters used to generate distorted waves on the values of the coincident cross section by choosing three sets for each system. These sets, labeled I, II, and III for each of the systems $p+^{12}\text{C}$, $p+^8\text{Be}$ and $^4\text{He}+^8\text{Be}$, are listed in Table 5.1. These potential sets are different, but roughly equivalent in their descriptions of the appropriate elastic scattering for each particle-target system. Representative results are shown in Fig. 5.15 for three angle pairs, with the optional parameter sets identified. Each energy-sharing cross section distribution is normalised independently to the experimental values. This implies a dependence of the spectroscopic factor extracted from the experimental data on the exact optical model parameter set. Values, which are indicated in Fig. 5.15, show this parameter-set dependence to be modest. Furthermore, the shapes of the cross section distributions are almost independent of which specific set is used.

The sensitivity of the cross section results to the radius, r_R and diffuseness a_R parameters

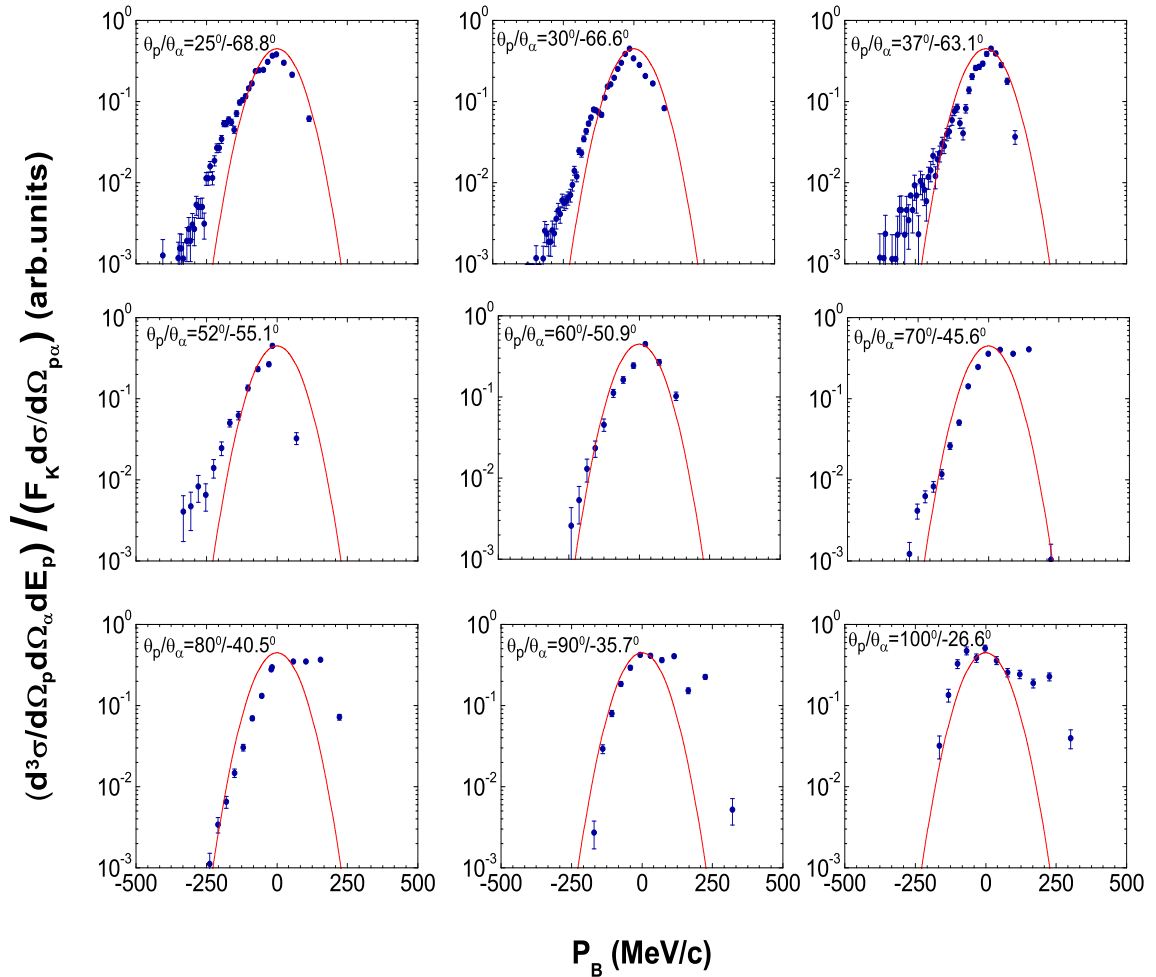


Figure 5.12. Alpha-cluster momentum distributions at the nine angle pairs extracted from the experimental cross sections for the $^{12}\text{C}(p, p\alpha)^8\text{Be}$ reaction. Statistical error bars on the experimental values are indicated. The curves represent a Gaussian fit $f(x) = A\exp[-1/2(x/\sigma)^2]$ on the momentum distribution with $\sigma = 65$ and $A \approx 0.45$. The scale on the vertical axis is in arbitrary units.

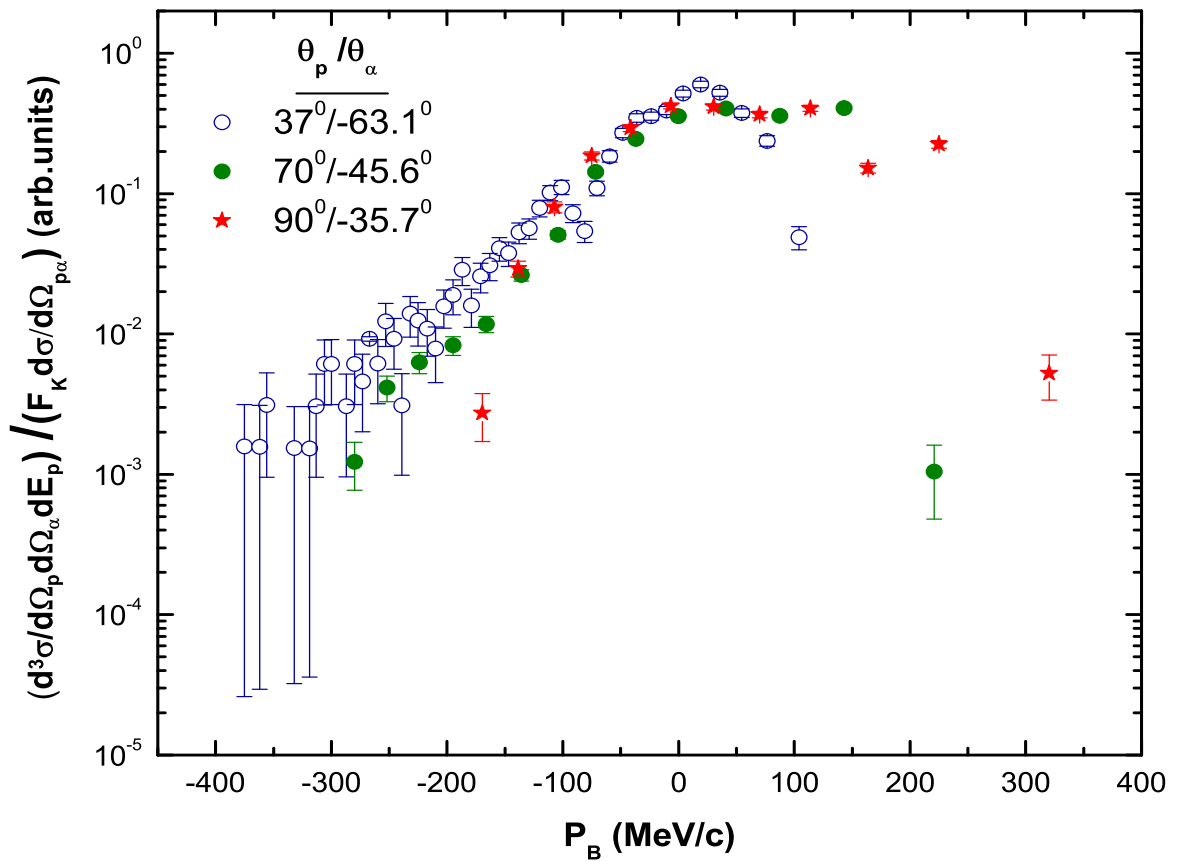


Figure 5.13. Alpha-cluster momentum distributions at three angle pairs, as indicated, extracted from the experimental cross sections for the $^{12}\text{C}(p, p\alpha)^8\text{Be}$ reaction. Statistical error bars on the experimental values are indicated. The scale on the vertical axis is in arbitrary units.

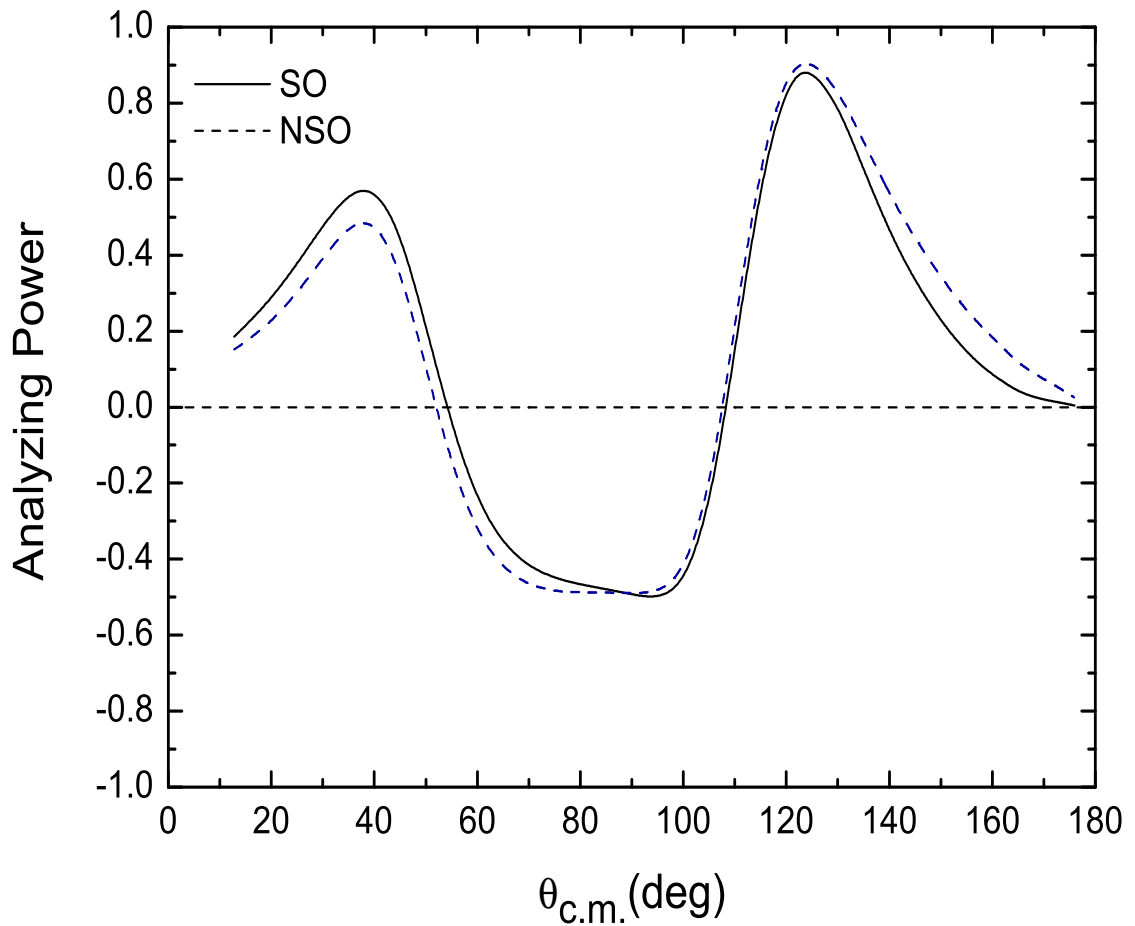


Figure 5.14. Analyzing power distributions for the reaction plotted as a function of centre-of-mass angle. Solid and dashed curves represent DWIA calculations respectively by including (SO) and excluding (NSO) spin-orbit terms in generating distorted-waves. DWIA calculations were performed using set I of distorting potentials and set II of $p+{}^4\text{He}$ optical model parameters in Table 5.1.

of the bound state has also been investigated. We confirm the general trend of the results found by Carey *et al.* [9] and Roos *et al.* [1]. As shown in Fig. 5.16, changes in shape of the energy-sharing cross section distributions are associated with variation in either of the parameter values. Comparison between theoretical prediction and experimental cross section distribution, at especially the set for the smallest proton angle, suggests that a slightly larger value of r_R or a_R could be appropriate. However, such an adjustment changes the extracted spectroscopic factor by approximately 40%, as may be inferred from Fig. 5.17. This variation should be compared with the standard deviation of approximately 70% in the average value of the spectroscopic factor listed in Table 5.4.

5.6 Analyzing Power Distributions at the Non-zero Recoil Momentum Condition

The general idea is to see how the angular distribution of the analyzing power changes when removing an alpha-cluster which is not at rest in the laboratory coordinate system as in the foregoing discussions. In Fig. 5.18 results are presented for analyzing power angular distributions which were not measured at the quasifree kinematic condition. Comparing the three plots, we find that the observed experimental trend is nevertheless reproduced by the DWIA calculations. For example, as the recoil momentum in the $^{12}\text{C}(p, p\alpha)^8\text{Be}$ reaction changes from positive to an (increasingly higher) negative value, the analyzing power at a centre-of-mass scattering angle near 90° changes from large negative to positive. Also, apart from the regions $\theta_{c.m.} < 37^\circ$ and $\theta_{c.m.} > 90^\circ$ in which small changes were observed, the region $37^\circ < \theta_{c.m.} < 90^\circ$ becomes deeper at positive recoil momentum and shallower when decreasing the recoil momentum. The trend of the DWIA results is consistent with this behaviour, and it is presumably caused by the kinematic change with recoil momentum which affects a variation in the effective two-body kinetic energy.

Finally, we can now postulate that the correspondence between experimental results and DWIA predictions also holds for large absolute values for the recoil momenta, thus the quasifree character of the knockout reaction is retained under those conditions. Conclusions regarding the simplicity of the reaction mechanism follows exactly as before.

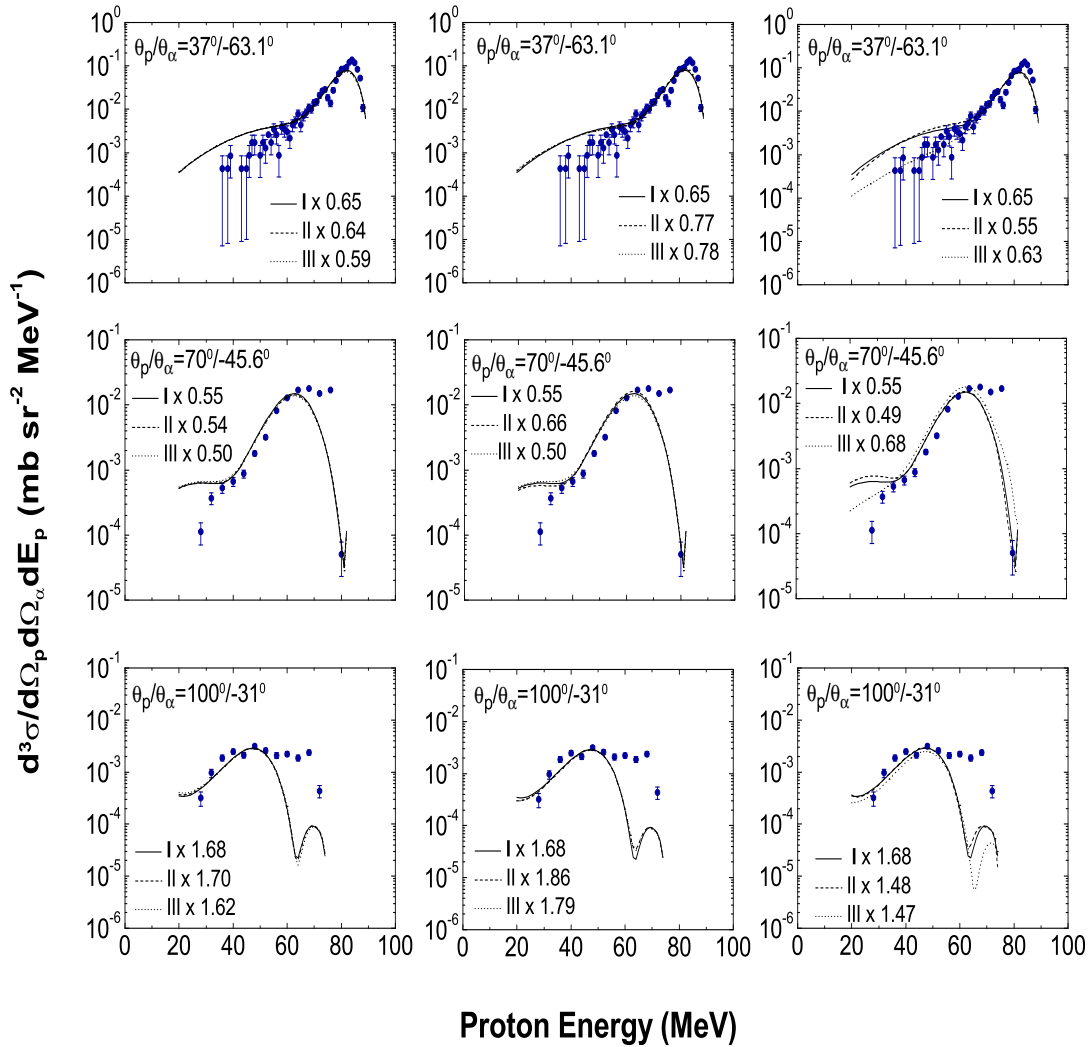


Figure 5.15. Comparison of energy-sharing cross section distributions with different optical potentials, as listed in Table 5.1. Three optical potential sets I, II and III are used in the reaction channels $p+^{12}\text{C}$ (left panels), $p+^8\text{Be}$ (centre panels), and $^4\text{He}+^8\text{Be}$ (right panels). Potential identifications in the figures are followed by numerical values of the spectroscopic factor for each case

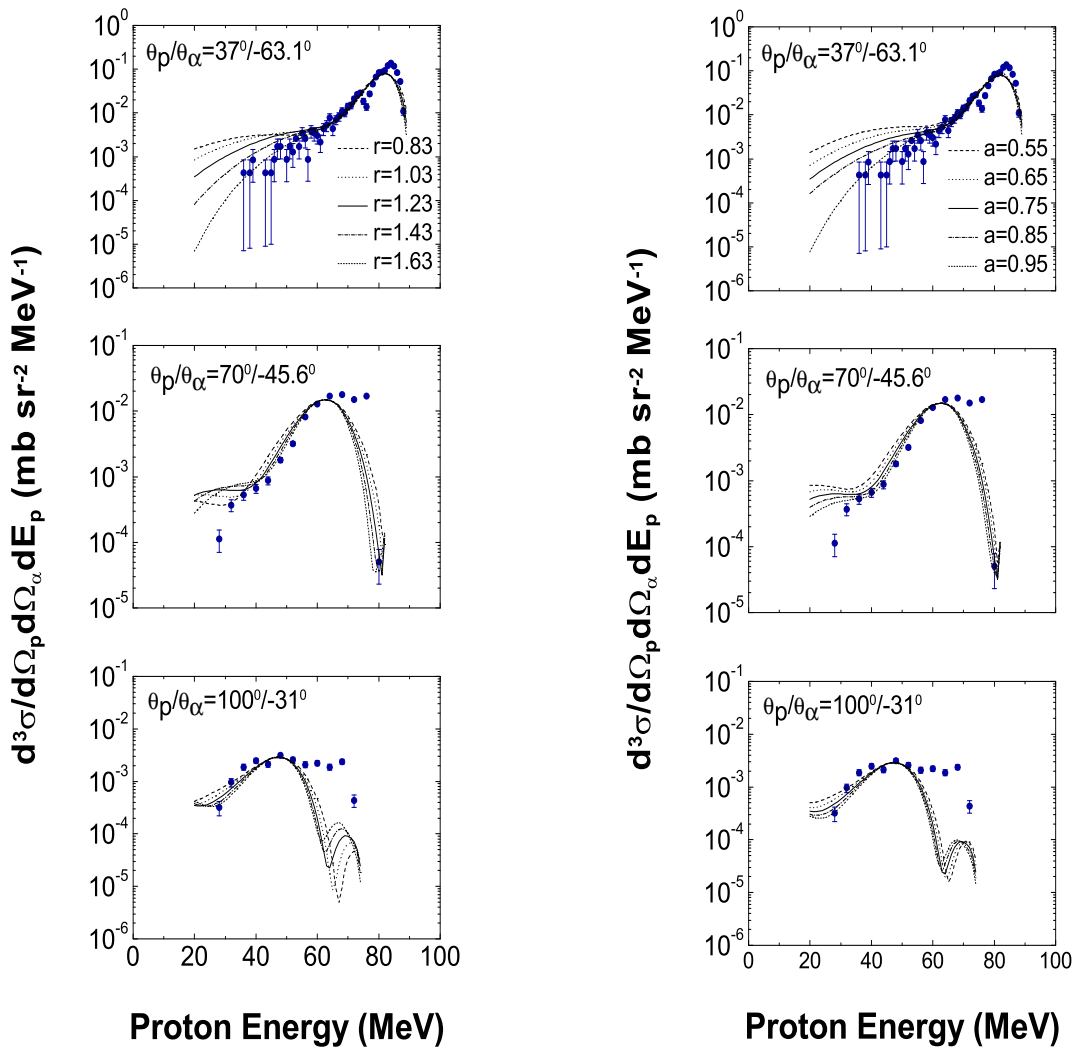


Figure 5.16. Comparison of energy-sharing cross section distributions with different values of the bound state radius parameter r_R (indicated as r in the left panels) and the diffuseness parameter a_R (indicated as a in the right panels). All curves are normalized to the peak cross section values at zero recoil momentum.

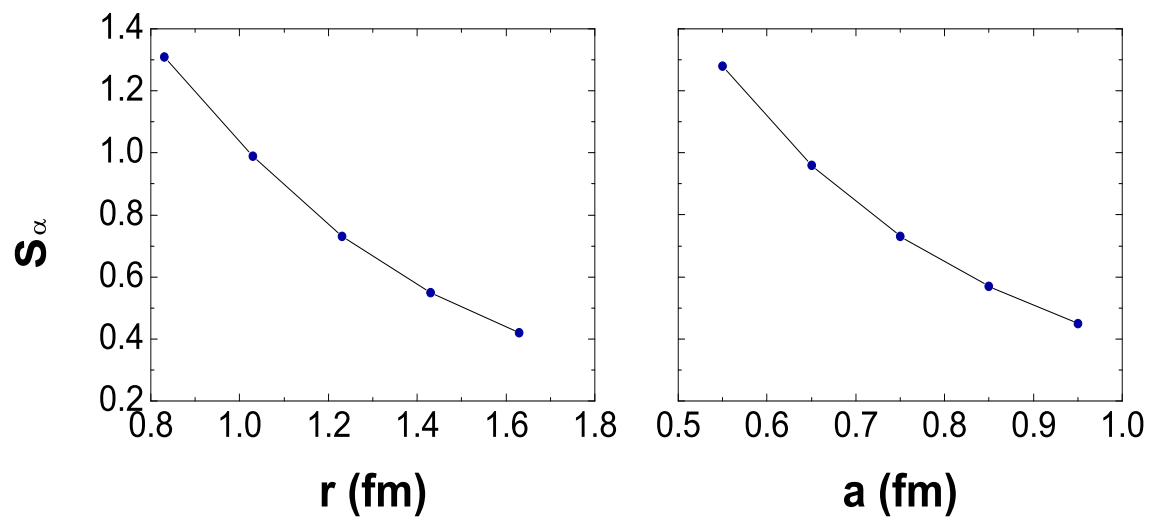


Figure 5.17. Dependence of the average extracted spectroscopic factor S_α as a function of bound state radius r_R (indicated as r in the left panel) and diffuseness parameters a_R (indicated as a in the right panel).

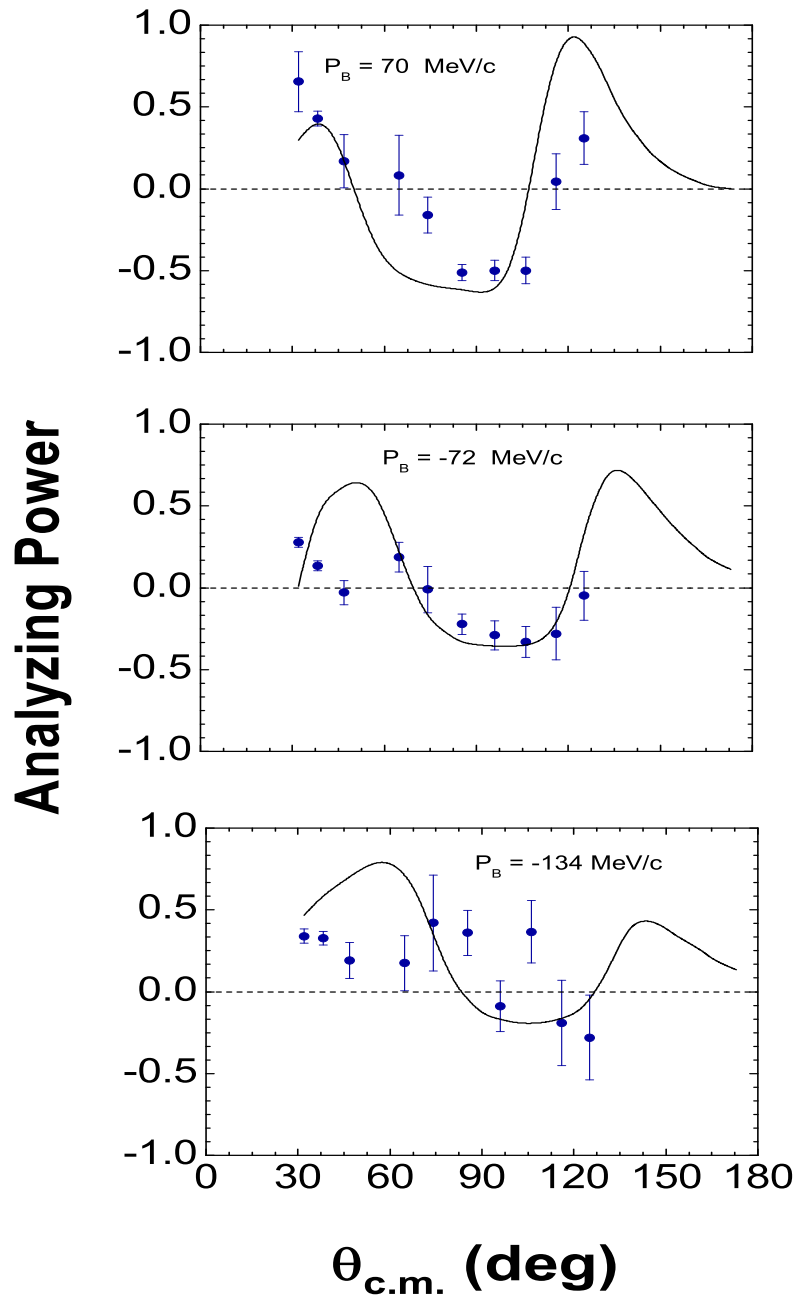


Figure 5.18. Analyzing power distributions for the $^{12}\text{C}(p, p\alpha)^8\text{Be}$ reaction displayed as a function of the two-body centre-of-mass scattering angle. Results are shown for three values of the recoil momentum of the ^8Be residue. Statistical error bars on the experimental values are indicated. The curves represent results of DWIA calculations.

Chapter 6

Summary and Conclusions

The work was devoted to the study of the $^{12}\text{C}(p, p\alpha)^8\text{Be}$ quasifree knockout reaction using polarized protons at an incident energy of 100 MeV. The focus was to investigate alpha clustering phenomena in ^{12}C by means of a knockout reaction.

In the first chapter the historical motivation for undertaking such a study was outlined. Alpha clustering in nuclei was reviewed and the most important aspects of the nuclear structure and nuclear reactions were described.

The theory used to interpret the experimental data was described in Chapter 2. A simple plane-wave model was firstly introduced as a simplistic description to provide insight into the direct knockout reaction used to probe clusters in nuclei, followed by a more realistic model, namely a distorted-wave model. The distorted-wave model takes into account distortions of particle wave functions resulting from the interaction between the incoming and outgoing particles with the target and recoiling nuclei.

The subject of Chapter 3 was the experimental details. The accelerator facility was presented, followed by the scattering chamber, the targets, the detector telescopes used during the experiment and certain electronics required for signal processing. The hardware and software used for data acquisition system, the polarimeter that enabled the beam polarization measurement and the experimental procedure were extensively described.

In Chapter 4, the replay of data that enables the extraction of the experimental data was discussed. In particular, the energy calibrations of detectors, the identification of particles,

the corrections made to the experimental data and polarization measurements, were fully described. A discussion of various features of the resulting two-dimensional energy spectra, binding energy spectra, and energy-sharing spectra was then used to present the experimental results. Both the statistical as well as the systematic uncertainties propagated through the experiment were also discussed.

In Chapter 5 the experimental and theoretical results as well as the discussion of the results were presented.

Cross sections and analyzing powers were measured at ten quasifree angle pairs $(\theta_p, \theta_\alpha)$ from $(25^\circ, -68.8^\circ)$ to $(110^\circ, -26.6^\circ)$, angles in which the remaining nucleus momentum is kinematically allowed to be zero. Experimental results of these observables were interpreted in terms of DWIA theoretical calculations performed by means of the computer code THREEDDEE. Since measurements of analyzing powers were made, the inclusion of spin-orbit distortions was required in the DWIA calculations. The DWIA predictions agree reasonably well with the shapes of the energy-sharing cross sections although some inconsequential discrepancies due to alpha-decay processes were observed at some angle pairs. In addition, it was also noted that the DWIA theory tends to overestimate the experimental yields on the low-proton-energy side of the energy-sharing cross sections for three forward angles. This was related to parameter-set dependence on the bound state, as it was suggested that a slightly larger value of radius and diffuseness parameters of the bound state would be appropriate. Overall the shapes of the energy-sharing distributions of the experimental analyzing power distributions agree fairly well with the theoretical predictions.

The spectroscopic factors extracted from the data were found to be reasonably consistent with theoretical predictions for both $p+{}^4\text{He}$ potential sets used, despite a somewhat large spread for different angle pairs. The dependence of extracted spectroscopic factors on optical model parameter sets was also investigated. A variation of approximately 40% was obtained, but this is modest if one compares it to the standard deviation of approximately 70% in the average value of the spectroscopic factor.

The validity of factorization approximation in the DWIA formulation, whereby the two-body $p\text{-}\alpha$ cross section enters as a multiplicative factor in the three-body $(p, p\alpha)$ cross section expression, is confirmed by means of a comparison between knockout and elastic

scattering, as well as the alpha-cluster momentum distribution. The $^{12}\text{C}(p, p\alpha)^8\text{Be}$ analyzing power data at the quasifree (zero recoil momentum) kinematic condition follow the trend of free elastic scattering $^4\text{He}(p, p)^4\text{He}$ data remarkably well, and comparisons with DWIA calculations also provide good agreement. The inclusion of a spin-orbit term in the distorting potentials was found to have negligible effect around the quasifree peak where the alpha-cluster momentum is small. Furthermore, analyzing power angular distributions as a function of p - α two-body centre-of-mass scattering angle, at non-zero recoil momentum of the residual nucleus ^8Be , were also investigated. The observed trend with varying recoil momentum was again reproduced reasonably well by the DWIA calculations.

The DWIA calculations were performed for different distorting, bound state and $p+^4\text{He}$ potentials and the result is consistent within the uncertainty in the input quantities (distorting, bound state and $p+^4\text{He}$ potentials). It is noteworthy that, only the new $p+^4\text{He}$ optical model parameters give a better compromise between two-body p - α cross section and analyzing power angular distributions.

These results strongly support the justification for an assumption that preformed α -clusters exist in ^{12}C because of the following conditions which were found to hold:

(i) the (distorted) momentum distribution of clusters inferred from the coincidence spectra of emitted particles is in agreement with that expected for a cluster bound in the target nucleus,

(ii) the extracted cluster preformation probability is in agreement with independent theoretical expectation,

(iii) the angular distributions of the two-body cross section and analyzing power from this coincidence experiment are in approximate agreement with those of a free interaction of the projectile with a target nucleus which is equivalent to the cluster.

This work shows that the $^{12}\text{C}(p, p\alpha)^8\text{Be}$ reaction proceeds as a quasifree process in which the core in the target system acts as a mere spectator to the knockout process in which the projectile and the cluster participate.

In the similar work of Roos *et al.* [1], it was shown that the mechanism seems to be quasifree, but this was based only on three angle pairs, and only on cross section distri-

butions. Also their study lacks a factorization test of DWIA mechanism. However in this work, we look over a much wider two-body angular range, we track the cross section over almost three orders of magnitude and the factorization of DWIA holds. The analyzing power angular distribution also shows remarkable factorization. Roos *et al.* [1] did not measure analyzing power. At 296 MeV [22], however, analyzing power distributions differ significantly from the DWIA and PWIA predictions suggesting that, there are large contributions from processes other than quasifree. However, these conclusions were based on experimental data for which the ground state was not resolved from the first excited state. The influence of the excited state is a complication, because the energy-sharing distributions of knockout to the excited state are not fitted well by the DWIA, and spectroscopic factors extracted from these calculations are almost unreasonably large, as pointed out by Roos *et al.* [1].

Clearly, the signature of the reaction mechanism is well established in the present analysis. However, further improvement of the theoretical calculations would require a better understanding of the input quantities, such as optical model parameter sets, in the DWIA theory. Additional theoretical investigations are also required to explain the results from an earlier knockout study on ^{40}Ca [23], which appears to be more complicated than the present work. Nevertheless, it is tempting to speculate that in the case of the heavier target, the phasing of distortions is such that non-factorization of the knockout cross section in the DWIA is retained. Consequently, additional experimental work needs to be carried out on targets heavier than ^{12}C at bombarding energies of 100 MeV and above. As was demonstrated in this work, a large angular range needs to be explored with sufficiently good energy resolution in order to extract useful information. Such future investigations should help to draw conclusions regarding α -clustering in nuclei heavier than ^{12}C as well as the possible general validity of the factorization approximation.

References

- [1] P. G. Roos *et al.*, Phys. Rev. C **15**, 69 (1977). [ix](#), [7](#), [8](#), [9](#), [15](#), [18](#), [24](#), [34](#), [76](#), [79](#), [81](#), [87](#), [88](#), [92](#), [95](#), [99](#), [106](#), [107](#)
- [2] A. Nadasen *et al.*, IUCF Scientific and Technical Report **No.13, 1983** (unpublished). [x](#), [89](#), [93](#), [94](#)
- [3] J. J. Lawrie *et al.*, NAC Annual Report **32** (1991). [xii](#), [62](#), [63](#)
- [4] J. Mabilia *et al.*, Phys. Rev. C **79**, 054612 (2009). [xii](#), [79](#), [89](#)
- [5] G. Gamow, Proc. Roy. Soc. A **126**, 632 (1930). [1](#)
- [6] L. A. Hafstadt and E. Teller, Phys. Rev. **54**, 681 (1937). [1](#)
- [7] J. A. Wheeler, Phys. Rev. **52**, 1083 (1937). [1](#)
- [8] H. Margenau, Phys. Rev. **59**, 37 (1941). [1](#)
- [9] T. A. Carey, P. G. Roos, N. S. Chant, A. Nadasen, and H. L. Chen, Phys. Rev. C **29**, 1273 (1984). [2](#), [7](#), [8](#), [21](#), [99](#)
- [10] G. Jacob and T. A. J. Maris, Phys. Rev. **38**, 121 (1966). [4](#)
- [11] P. E. Hodgson, *The Nucleon Optical Model* (World Scientific Publishing Co. Pte. Ltd., 1994). [4](#)
- [12] P. E. Hodgson, *Nuclear Reactions and Nuclear Structure* (Clarendon Press, Oxford, 1971). [5](#)
- [13] F. Perey and B. Buck, Nucl. Phys. **32**, 353 (1962). [6](#)

-
- [14] M. G. Mayer and J. H. D. Jensen, *Elementary Theory of Nuclear Shell Structure* (John Wiley & Sons, Inc., New York, N.Y., 1955). 7
- [15] O. Haxel, J. Hans, D. Jensen, and H. E. Suess, Phys. Rev. **75**, 1766 (1949). 7
- [16] M. G. Mayer, Phys. Rev. **75**, 1969 (1949). 7
- [17] A. Nadasen *et al.*, Phys. Rev. C **23**, 2353 (1981). 7, 8
- [18] C. W. Wang *et al.*, Phys. Rev. C **31**, 1662 (1985). 7, 8
- [19] C. Samanta, N. S. Chant, P. G. Roos, A. Nadasen, and A. A. Cowley, Phys. Rev. C **26**, 1379 (1982). 7
- [20] A. Nadasen *et al.*, Phys. Rev. C **22**, 1394 (1980). 8
- [21] A. Nadasen *et al.*, Phys. Rev. C **40**, 1130 (1989). 8
- [22] T. Yoshimura *et al.*, Nucl. Phys. A **641**, 3 (1998). 8, 9, 107
- [23] R. Neveling *et al.*, Phys. Rev. C **77**, 037601 (2008). 9, 107
- [24] G. F. Steyn *et al.*, Phys. Rev. C **59**, 2097 (1999). 9
- [25] A. A. Cowley *et al.*, Phys. Rev. C **15**, 1650 (1977). 9
- [26] T. A. J. Maris, P. Hillman, and H. Tyren, Nucl. Phys. **7**, 1 (1958). 11
- [27] G. F. Chew, Phys. Rev. **80**, 196 (1950). 11
- [28] N. S. Chant and P. G. Roos, Phys. Rev. C **15**, 57 (1977). 11, 12, 13, 17, 18, 19, 20, 21, 22
- [29] J. Mabilia, *Theoretical Description of Quasi-free $A(a,a'b)B$ Reactions* (AIMS Project, 2007 (unpublished)). 13
- [30] P. Li, *Measurement of spin observables in $(p,2p)$ quasi-free scattering from very light nuclei*, PhD thesis, Indiana University, 1994 (unpublished). 15
- [31] D. F. Jackson, *Nuclear Reactions* (Chapman and Hall, London, 1970). 15
- [32] J. W. Watson *et al.*, Nucl. Phys. A **172**, 513 (1971). 16

-
- [33] D. F. Jackson and T. Berggren, Nucl. Phys. **62**, 353 (1965). [16](#)
- [34] C. Samanta, *A study of proton and alpha particle induced quasifree knockout reactions*, PhD thesis, University of Maryland, 1981 (unpublished). [16](#), [31](#)
- [35] N. S. Chant and P. G. Roos, Phys. Rev. C **27**, 1060 (1983). [23](#), [24](#), [76](#)
- [36] N. S. Chant, Threedee code, University of Maryland (1992), (unpublished). [24](#), [25](#), [26](#), [27](#)
- [37] G. J. Arendse, *Nuclear distortions in the (p,2p) knockout reaction on ^{208}Pb at an incident energy of 200 MeV*, PhD thesis, University of Stellenbosch, 1997 (unpublished). [25](#)
- [38] G. R. Satchler, *Direct Nuclear Reactions* (Clarendon Press-Oxford, 1983). [28](#)
- [39] P. Schwandt, T. B. Clegg, and W. Haeberli, Nucl. Phys. A **163**, 432 (1971). [31](#)
- [40] R. Neveling, *Private communication*. [32](#)
- [41] J. V. Pilcher, *Coincident Proton Decay of the Continuum Induced by 200 MeV Protons on ^{12}C* , PhD thesis, University of Cape Town, 1989 (unpublished). [48](#)
- [42] S. V. Förtsch, *Proton emission in pre-equilibrium reactions induced by incident protons of 100 to 200 MeV*, PhD thesis, University of Pretoria, 1992 (unpublished). [53](#), [69](#)
- [43] G. F. Knoll, *Radiation Detection and Measurement* (John Willey & Sons, New York Chichester Brisbane Toronto, 1979). [55](#), [71](#)
- [44] W. R. Leo, *Techniques for Nuclear and Particles Physics Experiments* (Springer Verlag, 1994). [61](#), [72](#)
- [45] R. E. L. Green, D. H. Boal, R. L. Helmer, K. P. Jackson, and R. G. Korteling, Nucl. Phys. A **405**, 463 (1983). [61](#)
- [46] W. Haeberli, *Polarization Experiments, Polarized Beams* (Nuclear Spectroscopy and Reactions (Part A), edited by J. Cerny, Academic Press New York and London, California, 1974). [66](#), [67](#), [68](#)

-
- [47] T. A. Carey, *A systematic study of alpha-particle spectroscopic strengths using the $(p, p\alpha)$ reaction at 101.5 MeV*, PhD thesis, University of Maryland, 1979 (unpublished). [72](#)
- [48] P. Jipsen, A program for calculating the ranges of ions in matter, National Accelerator Centre (1984), unpublished. [73](#)
- [49] D. M. Whittall, *Quasifree knockout of charged particles from ^4He with 100 MeV protons*, PhD thesis, University of Cape Town, 1989 (unpublished). [73](#)
- [50] J. S. C. M. J. Berger and M. A. Zucker, ESTAR, PSTAR, and ASTAR: Computer Programs for Calculating Stopping-Power and Range Tables for Electrons, Protons, and Helium Ions (National Institute of Standards and Technology, Gaithersburg, MD, 1999), version 1.2.2, <http://physics.nist.gov/PhysRefData/Star/Text/ASTAR.html> [20August2003]. [73](#)
- [51] V. Comparat *et al.*, Phys. Rev. C **12**, 251 (1975). [75](#), [78](#), [79](#), [89](#)
- [52] T. Y. Li and S. K. Mark, Can. J. Phys. **46**, 2645 (1968). [79](#)
- [53] G. S. Mani, D. Jacques, and A. D. B. Dix, Nucl. Phys. A **165**, 145 (1971). [79](#)
- [54] R. M. DeVries, J. L. Perrenoud, I. Slaus, and J. W. Sunier, Nucl. Phys. A **178**, 424 (1972). [79](#)
- [55] D. Kurath, Phys. Rev. C **7**, 1390 (1973). [81](#), [88](#)
- [56] N. P. Goldstein, A. Held, and D. G. Stairs, Can. J. Phys. **48**, 2629 (1970). [89](#)

Appendix A

Tabulation of Experimental Energy-sharing Cross Section Data

Table A.1: $\theta_p/\theta_\alpha = 25^\circ / -68.8^\circ$

E_p (MeV)	$d^3\sigma/d\Omega_p d\Omega_\alpha dE_p$ (mb sr ⁻² MeV ⁻¹)
40	$(6.540 \pm 3.780) \times 10^{-4}$
41	$(2.180 \pm 2.180) \times 10^{-4}$
42	$(2.180 \pm 2.180) \times 10^{-4}$
43	$(4.360 \pm 3.080) \times 10^{-4}$
44	$(2.180 \pm 2.180) \times 10^{-4}$
45	$(2.180 \pm 2.180) \times 10^{-4}$
46	$(4.360 \pm 3.080) \times 10^{-4}$
47	—
48	$(2.180 \pm 2.180) \times 10^{-4}$
49	$(6.540 \pm 3.780) \times 10^{-4}$
50	$(8.720 \pm 4.360) \times 10^{-4}$
51	$(8.720 \pm 4.360) \times 10^{-4}$
52	$(6.540 \pm 3.780) \times 10^{-4}$
53	$(4.360 \pm 3.080) \times 10^{-4}$
54	$(1.090 \pm 0.487) \times 10^{-3}$
55	$(1.530 \pm 0.577) \times 10^{-3}$
56	$(1.090 \pm 0.487) \times 10^{-3}$
57	$(1.740 \pm 0.616) \times 10^{-3}$
58	$(1.530 \pm 0.577) \times 10^{-3}$
59	$(3.050 \pm 0.816) \times 10^{-3}$
60	$(2.830 \pm 0.786) \times 10^{-3}$
61	$(2.830 \pm 0.786) \times 10^{-3}$
62	$(2.830 \pm 0.786) \times 10^{-3}$
63	$(1.740 \pm 0.616) \times 10^{-3}$
64	$(6.320 \pm 1.170) \times 10^{-3}$
65	$(6.320 \pm 1.170) \times 10^{-3}$
66	$(8.720 \pm 1.380) \times 10^{-3}$
67	$(6.320 \pm 1.170) \times 10^{-3}$
68	$(1.020 \pm 0.149) \times 10^{-2}$
69	$(1.440 \pm 0.177) \times 10^{-2}$

Table A.1: $\theta_p/\theta_\alpha = 25^\circ / -68.8^\circ$

E_p (MeV)	$d^3\sigma/d\Omega_p d\Omega_\alpha dE_p$ (mb sr ⁻² MeV ⁻¹)
70	$(1.440 \pm 0.177) \times 10^{-2}$
71	$(1.810 \pm 0.199) \times 10^{-2}$
72	$(2.790 \pm 0.246) \times 10^{-2}$
73	$(2.750 \pm 0.245) \times 10^{-2}$
74	$(3.030 \pm 0.257) \times 10^{-2}$
75	$(2.790 \pm 0.246) \times 10^{-2}$
76	$(2.220 \pm 0.220) \times 10^{-2}$
77	$(3.430 \pm 0.273) \times 10^{-2}$
78	$(4.640 \pm 0.318) \times 10^{-2}$
79	$(4.860 \pm 0.325) \times 10^{-2}$
80	$(5.300 \pm 0.340) \times 10^{-2}$
81	$(6.470 \pm 0.376) \times 10^{-2}$
82	$(7.320 \pm 0.400) \times 10^{-2}$
83	$(1.003 \pm 0.047) \times 10^{-1}$
84	$(1.007 \pm 0.047) \times 10^{-1}$
85	$(9.740 \pm 0.461) \times 10^{-2}$
86	$(1.190 \pm 0.051) \times 10^{-1}$
87	$(1.350 \pm 0.054) \times 10^{-1}$
88	$(1.350 \pm 0.054) \times 10^{-1}$
89	$(1.012 \pm 0.047) \times 10^{-1}$
90	$(6.950 \pm 0.389) \times 10^{-2}$
91	$(3.663 \pm 0.282) \times 10^{-2}$
92	$(4.800 \pm 1.020) \times 10^{-3}$

Table A.2: $\theta_p/\theta_\alpha = 30^\circ / -66.6^\circ$

E_p (MeV)	$d^3\sigma/d\Omega_p d\Omega_\alpha dE_p$ (mb sr ⁻² MeV ⁻¹)
31	$(1.570 \pm 1.540) \times 10^{-4}$
32	—
33	$(1.570 \pm 1.540) \times 10^{-4}$
34	$(3.150 \pm 2.180) \times 10^{-4}$
35	$(3.150 \pm 2.180) \times 10^{-4}$
36	$(1.580 \pm 1.540) \times 10^{-4}$
37	$(3.160 \pm 2.180) \times 10^{-4}$
38	$(3.160 \pm 2.180) \times 10^{-4}$
39	$(1.580 \pm 1.540) \times 10^{-4}$
40	$(1.580 \pm 1.540) \times 10^{-4}$
41	$(6.340 \pm 3.080) \times 10^{-4}$
42	$(6.350 \pm 3.080) \times 10^{-4}$
43	$(4.770 \pm 2.670) \times 10^{-4}$
44	$(6.370 \pm 3.080) \times 10^{-4}$
45	$(3.190 \pm 2.180) \times 10^{-4}$
46	$(7.980 \pm 3.450) \times 10^{-4}$
47	$(6.390 \pm 3.080) \times 10^{-4}$
48	$(6.400 \pm 3.080) \times 10^{-4}$
49	$(1.600 \pm 1.540) \times 10^{-4}$
50	$(8.020 \pm 3.450) \times 10^{-4}$
51	$(1.770 \pm 0.511) \times 10^{-3}$
52	$(1.610 \pm 0.487) \times 10^{-3}$
53	$(1.290 \pm 0.436) \times 10^{-3}$
54	$(1.290 \pm 0.436) \times 10^{-3}$
55	$(1.780 \pm 0.511) \times 10^{-3}$
56	$(1.620 \pm 0.487) \times 10^{-3}$
57	$(2.430 \pm 0.597) \times 10^{-3}$
58	$(3.090 \pm 0.672) \times 10^{-3}$
59	$(2.760 \pm 0.635) \times 10^{-3}$

Table A.2: $\theta_p/\theta_\alpha = 30^\circ / -66.6^\circ$

E_p (MeV)	$d^3\sigma/d\Omega_p d\Omega_\alpha dE_p$ (mb sr ⁻² MeV ⁻¹)
60	$(4.070 \pm 0.771) \times 10^{-3}$
61	$(3.750 \pm 0.739) \times 10^{-3}$
62	$(3.920 \pm 0.755) \times 10^{-3}$
63	$(4.260 \pm 0.786) \times 10^{-3}$
64	$(4.590 \pm 0.816) \times 10^{-3}$
65	$(6.080 \pm 0.937) \times 10^{-3}$
66	$(9.060 \pm 1.140) \times 10^{-3}$
67	$(7.590 \pm 1.050) \times 10^{-3}$
68	$(1.553 \pm 0.149) \times 10^{-2}$
69	$(1.440 \pm 0.144) \times 10^{-2}$
70	$(2.140 \pm 0.175) \times 10^{-2}$
71	$(2.610 \pm 0.193) \times 10^{-2}$
72	$(3.210 \pm 0.214) \times 10^{-2}$
73	$(3.750 \pm 0.231) \times 10^{-2}$
74	$(4.680 \pm 0.258) \times 10^{-2}$
75	$(4.500 \pm 0.253) \times 10^{-2}$
76	$(4.130 \pm 0.242) \times 10^{-2}$
77	$(3.833 \pm 0.233) \times 10^{-2}$
78	$(6.150 \pm 0.294) \times 10^{-2}$
79	$(8.170 \pm 0.339) \times 10^{-2}$
80	$(8.590 \pm 0.347) \times 10^{-2}$
81	$(1.004 \pm 0.037) \times 10^{-1}$
82	$(1.270 \pm 0.042) \times 10^{-1}$
83	$(1.470 \pm 0.045) \times 10^{-1}$
84	$(1.850 \pm 0.051) \times 10^{-1}$
85	$(2.090 \pm 0.054) \times 10^{-1}$
86	$(1.520 \pm 0.046) \times 10^{-1}$
87	$(1.220 \pm 0.041) \times 10^{-1}$
88	$(8.782 \pm 0.348) \times 10^{-2}$
89	$(6.973 \pm 0.310) \times 10^{-2}$
90	$(3.770 \pm 0.228) \times 10^{-2}$
91	$(6.590 \pm 0.950) \times 10^{-3}$

Table A.3: $\theta_p/\theta_\alpha = 37^\circ / -63.1^\circ$

E_p (MeV)	$d^3\sigma/d\Omega_p d\Omega_\alpha dE_p$ (mb sr ⁻² MeV ⁻¹)
36	$(4.250 \pm 4.180) \times 10^{-4}$
37	—
38	$(4.260 \pm 4.180) \times 10^{-4}$
39	$(8.520 \pm 5.910) \times 10^{-4}$
40	—
41	—
42	—
43	$(4.270 \pm 4.180) \times 10^{-4}$
44	$(0.000 \pm 4.180) \times 10^{-4}$
45	$(4.280 \pm 4.180) \times 10^{-4}$
46	$(8.570 \pm 5.910) \times 10^{-4}$
47	$(1.710 \pm 0.836) \times 10^{-3}$
48	$(1.720 \pm 0.836) \times 10^{-3}$
49	—
50	$(0.860 \pm 0.591) \times 10^{-3}$
51	$(1.720 \pm 0.836) \times 10^{-3}$
52	$(1.290 \pm 0.724) \times 10^{-3}$
53	$(2.590 \pm 0.102) \times 10^{-3}$
54	$(1.730 \pm 0.836) \times 10^{-3}$
55	$(3.460 \pm 1.180) \times 10^{-3}$
56	$(2.600 \pm 1.020) \times 10^{-3}$
57	$(0.867 \pm 0.591) \times 10^{-3}$
58	$(3.900 \pm 1.250) \times 10^{-3}$
59	$(3.470 \pm 1.180) \times 10^{-3}$
60	$(3.040 \pm 1.110) \times 10^{-3}$
61	$(2.180 \pm 0.935) \times 10^{-3}$
62	$(4.360 \pm 1.320) \times 10^{-3}$
63	$(5.240 \pm 1.450) \times 10^{-3}$
64	$(7.860 \pm 1.770) \times 10^{-3}$
65	$(4.370 \pm 1.320) \times 10^{-3}$

Table A.3: $\theta_p/\theta_\alpha = 37^\circ / -63.1^\circ$

E_p (MeV)	$d^3\sigma/d\Omega_p d\Omega_\alpha dE_p$ (mb sr ⁻² MeV ⁻¹)
66	$(7.010 \pm 1.670) \times 10^{-3}$
67	$(8.330 \pm 1.820) \times 10^{-3}$
68	$(1.097 \pm 0.209) \times 10^{-2}$
69	$(1.011 \pm 0.200) \times 10^{-2}$
70	$(1.408 \pm 0.236) \times 10^{-2}$
71	$(1.498 \pm 0.244) \times 10^{-2}$
72	$(2.074 \pm 0.287) \times 10^{-2}$
73	$(2.650 \pm 0.324) \times 10^{-2}$
74	$(2.876 \pm 0.337) \times 10^{-2}$
75	$(1.861 \pm 0.271) \times 10^{-2}$
76	$(1.370 \pm 0.233) \times 10^{-2}$
77	$(2.750 \pm 0.329) \times 10^{-2}$
78	$(4.580 \pm 0.424) \times 10^{-2}$
79	$(6.640 \pm 0.510) \times 10^{-2}$
80	$(8.387 \pm 0.573) \times 10^{-2}$
81	$(8.530 \pm 0.578) \times 10^{-2}$
82	$(9.220 \pm 0.600) \times 10^{-2}$
83	$(1.196 \pm 0.068) \times 10^{-1}$
84	$(1.364 \pm 0.073) \times 10^{-1}$
85	$(1.173 \pm 0.068) \times 10^{-1}$
86	$(8.280 \pm 0.567) \times 10^{-2}$
87	$(5.184 \pm 0.448) \times 10^{-2}$
88	$(1.083 \pm 0.205) \times 10^{-2}$

Table A.4: $\theta_p/\theta_\alpha = 52^\circ / - 55.1^\circ$

E_p (MeV)	$d^3\sigma/d\Omega_p d\Omega_\alpha dE_p$ (mb sr ⁻² MeV ⁻¹)
32	$(1.085 \pm 0.618) \times 10^{-4}$
36	$(1.393 \pm 0.689) \times 10^{-4}$
40	$(2.649 \pm 0.962) \times 10^{-4}$
44	$(2.219 \pm 0.819) \times 10^{-4}$
48	$(5.042 \pm 1.280) \times 10^{-4}$
52	$(9.101 \pm 1.756) \times 10^{-4}$
56	$(1.910 \pm 0.201) \times 10^{-3}$
60	$(2.390 \pm 0.285) \times 10^{-3}$
64	$(5.250 \pm 0.419) \times 10^{-3}$
68	$(8.890 \pm 0.546) \times 10^{-3}$
72	$(1.008 \pm 0.058) \times 10^{-2}$
76	$(1.659 \pm 0.741) \times 10^{-2}$
80	$(1.170 \pm 0.197) \times 10^{-3}$

Table A.5: $\theta_p/\theta_\alpha = 60^\circ / - 50.9^\circ$

E_p (MeV)	$d^3\sigma/d\Omega_p d\Omega_\alpha dE_p$ (mb sr ⁻² MeV ⁻¹)
40	$(1.263 \pm 8.554) \times 10^{-4}$
44	$(2.626 \pm 1.287) \times 10^{-4}$
48	$(6.438 \pm 2.026) \times 10^{-4}$
52	$(1.140 \pm 0.265) \times 10^{-3}$
56	$(2.180 \pm 0.372) \times 10^{-3}$
60	$(5.160 \pm 0.566) \times 10^{-3}$
64	$(7.220 \pm 0.673) \times 10^{-3}$
68	$(1.039 \pm 0.080) \times 10^{-2}$
72	$(1.824 \pm 0.106) \times 10^{-2}$
76	$(1.053 \pm 0.081) \times 10^{-2}$
80	$(0.403 \pm 0.049) \times 10^{-2}$

Table A.6: $\theta_p/\theta_\alpha = 70^\circ / -45.6^\circ$

E_p (MeV)	$d^3\sigma/d\Omega_p d\Omega_\alpha dE_p$ (mb sr ⁻² MeV ⁻¹)
28	$(1.115 \pm 0.417) \times 10^{-4}$
32	$(3.673 \pm 0.755) \times 10^{-4}$
36	$(5.285 \pm 0.905) \times 10^{-4}$
40	$(6.587 \pm 1.008) \times 10^{-4}$
44	$(8.705 \pm 1.157) \times 10^{-4}$
48	$(1.800 \pm 0.166) \times 10^{-3}$
52	$(3.170 \pm 0.220) \times 10^{-3}$
56	$(8.140 \pm 0.352) \times 10^{-3}$
60	$(1.279 \pm 0.044) \times 10^{-2}$
64	$(1.704 \pm 0.051) \times 10^{-2}$
68	$(1.781 \pm 0.052) \times 10^{-2}$
72	$(1.496 \pm 0.047) \times 10^{-2}$
76	$(1.679 \pm 0.050) \times 10^{-2}$
80	$(0.504 \pm 0.273) \times 10^{-4}$

Table A.7: $\theta_p/\theta_\alpha = 80^\circ / -40.5^\circ$

E_p (MeV)	$d^3\sigma/d\Omega_p d\Omega_\alpha dE_p$ (mb sr ⁻² MeV ⁻¹)
28	$(1.152 \pm 0.403) \times 10^{-4}$
32	$(3.032 \pm 0.653) \times 10^{-4}$
36	$(4.924 \pm 0.830) \times 10^{-4}$
40	$(9.443 \pm 1.148) \times 10^{-4}$
44	$(1.650 \pm 0.151) \times 10^{-3}$
48	$(3.220 \pm 0.211) \times 10^{-3}$
52	$(5.210 \pm 0.268) \times 10^{-3}$
56	$(9.560 \pm 0.363) \times 10^{-3}$
60	$(8.890 \pm 0.349) \times 10^{-3}$
64	$(9.470 \pm 0.359) \times 10^{-3}$
68	$(8.870 \pm 0.347) \times 10^{-3}$
72	$(9.160 \pm 0.351) \times 10^{-3}$
76	$(2.010 \pm 0.164) \times 10^{-3}$

Table A.8: $\theta_p/\theta_\alpha = 90^\circ / -35.7^\circ$

E_p (MeV)	$d^3\sigma/d\Omega_p d\Omega_\alpha dE_p$ (mb sr ⁻² MeV ⁻¹)
32	$(7.104 \pm 2.649) \times 10^{-5}$
36	$(5.801 \pm 0.756) \times 10^{-4}$
40	$(1.230 \pm 0.110) \times 10^{-3}$
44	$(2.310 \pm 0.150) \times 10^{-3}$
48	$(3.120 \pm 0.174) \times 10^{-3}$
52	$(4.060 \pm 0.200) \times 10^{-3}$
56	$(3.850 \pm 0.193) \times 10^{-3}$
60	$(3.430 \pm 0.182) \times 10^{-3}$
64	$(3.930 \pm 0.194) \times 10^{-3}$
68	$(1.540 \pm 0.121) \times 10^{-3}$
72	$(2.410 \pm 0.151) \times 10^{-3}$
76	$(7.437 \pm 2.649) \times 10^{-5}$

Table A.9: $\theta_p/\theta_\alpha = 100^\circ / -31.0^\circ$

E_p (MeV)	$d^3\sigma/d\Omega_p d\Omega_\alpha dE_p$ (mb sr ⁻² MeV ⁻¹)
28	$(3.193 \pm 0.999) \times 10^{-4}$
32	$(9.606 \pm 1.729) \times 10^{-4}$
36	$(1.860 \pm 0.240) \times 10^{-3}$
40	$(2.480 \pm 0.277) \times 10^{-3}$
44	$(2.130 \pm 0.257) \times 10^{-3}$
48	$(3.150 \pm 0.311) \times 10^{-3}$
52	$(2.570 \pm 0.281) \times 10^{-3}$
56	$(2.090 \pm 0.253) \times 10^{-3}$
60	$(2.230 \pm 0.260) \times 10^{-3}$
64	$(1.880 \pm 0.238) \times 10^{-3}$
68	$(2.390 \pm 0.268) \times 10^{-3}$
72	$(4.334 \pm 1.139) \times 10^{-4}$

Table A.10: $\theta_p/\theta_\alpha = 110^\circ / -26.6^\circ$

E_p (MeV)	$d^3\sigma/d\Omega_p d\Omega_\alpha dE_p$ (mb sr ⁻² MeV ⁻¹)
28	$(1.403 \pm 0.253) \times 10^{-4}$
32	$(2.907 \pm 0.364) \times 10^{-4}$
36	$(3.903 \pm 0.421) \times 10^{-4}$
40	$(5.236 \pm 0.487) \times 10^{-4}$
44	$(4.308 \pm 0.441) \times 10^{-4}$
48	$(4.323 \pm 0.441) \times 10^{-4}$
52	$(3.243 \pm 0.381) \times 10^{-4}$
56	$(2.874 \pm 0.358) \times 10^{-4}$
60	$(2.454 \pm 0.330) \times 10^{-4}$
64	$(2.707 \pm 0.346) \times 10^{-4}$
68	$(3.351 \pm 0.384) \times 10^{-4}$

Appendix B

Tabulation of Experimental Energy-sharing Analyzing Power Data

Table B.1: $\theta_p/\theta_\alpha = 25^\circ / -68.8^\circ$

E_p (MeV)	A_y
48	-0.220 ± 0.390
52	-0.400 ± 0.344
56	0.155 ± 0.227
60	0.196 ± 0.194
64	0.094 ± 0.118
68	0.002 ± 0.082
72	0.250 ± 0.058
76	0.358 ± 0.051
80	0.322 ± 0.037
84	0.279 ± 0.029
88	0.395 ± 0.034
92	0.914 ± 0.332

Table B.2: $\theta_p/\theta_\alpha = 30^\circ / -66.6^\circ$

E_p (MeV)	A_y
40	0.000 ± 0.430
44	0.480 ± 0.390
48	-0.071 ± 0.328
52	-0.121 ± 0.248
56	-0.074 ± 0.192
60	-0.343 ± 0.158
64	-0.072 ± 0.116
68	0.117 ± 0.069
72	0.193 ± 0.048
76	0.325 ± 0.041
80	0.135 ± 0.028
84	0.214 ± 0.024
88	0.429 ± 0.044

Table B.3: $\theta_p/\theta_\alpha = 37^\circ / -63.1^\circ$

E_p (MeV)	A_y
52	-0.338 ± 0.319
56	-0.283 ± 0.289
60	0.313 ± 0.235
64	-0.433 ± 0.189
68	0.096 ± 0.128
72	0.287 ± 0.093
76	-0.028 ± 0.074
80	0.042 ± 0.047
84	0.240 ± 0.044
88	0.113 ± 0.279

Table B.4: $\theta_p/\theta_\alpha = 52^\circ / -55.1^\circ$

E_p (MeV)	A_y
36	-0.073 ± 0.744
40	-0.413 ± 0.537
44	-0.439 ± 0.657
48	-0.693 ± 0.444
52	-0.062 ± 0.273
56	-0.101 ± 0.237
60	0.174 ± 0.167
64	0.120 ± 0.112
68	0.186 ± 0.087
72	0.187 ± 0.082
76	-0.107 ± 0.065
80	0.083 ± 0.244

Table B.5: $\theta_p/\theta_\alpha = 60^\circ / -50.9^\circ$

E_p (MeV)	A_y
40	-0.774 ± 1.440
44	0.448 ± 0.690
48	0.161 ± 0.436
52	0.660 ± 0.350
56	0.179 ± 0.235
60	0.012 ± 0.152
64	-0.031 ± 0.132
68	-0.199 ± 0.113
72	-0.387 ± 0.086
76	-0.161 ± 0.109
80	-0.455 ± 0.241

Table B.6: $\theta_p/\theta_\alpha = 70^\circ / -45.6^\circ$

E_p (MeV)	A_y
28	-0.610 ± 0.582
32	-0.180 ± 0.295
36	0.210 ± 0.246
40	0.240 ± 0.221
44	0.210 ± 0.192
48	0.360 ± 0.137
52	-0.065 ± 0.100
56	-0.222 ± 0.064
60	-0.260 ± 0.051
64	-0.260 ± 0.044
68	-0.450 ± 0.045
72	-0.512 ± 0.050
76	-0.519 ± 0.047
80	-0.471 ± 0.859

Table B.7: $\theta_p/\theta_\alpha = 80^\circ / -40.5^\circ$

E_p (MeV)	A_y
28	0.691 ± 0.547
32	0.202 ± 0.312
36	0.412 ± 0.251
40	-0.066 ± 0.178
44	-0.110 ± 0.130
48	-0.210 ± 0.098
52	-0.370 ± 0.080
56	-0.480 ± 0.060
60	-0.550 ± 0.064
64	-0.530 ± 0.062
68	-0.470 ± 0.063
72	-0.750 ± 0.067
76	-0.930 ± 0.150

Table B.8: $\theta_p/\theta_\alpha = 90^\circ / -35.7^\circ$

E_p (MeV)	A_y
32	0.194 ± 0.521
36	-0.365 ± 0.191
40	-0.263 ± 0.128
44	-0.330 ± 0.095
48	-0.31 ± 0.082
52	-0.410 ± 0.073
56	-0.580 ± 0.079
60	-0.500 ± 0.082
64	-0.380 ± 0.074
68	-0.460 ± 0.120
72	-0.220 ± 0.092
76	0.190 ± 0.520

Table B.9: $\theta_p/\theta_\alpha = 100^\circ / -31.0^\circ$

E_p (MeV)	A_y
28	0.270 ± 0.440
32	-0.190 ± 0.260
36	-0.290 ± 0.190
40	-0.280 ± 0.160
44	-0.300 ± 0.180
48	-0.160 ± 0.140
52	0.088 ± 0.160
56	0.044 ± 0.170
60	0.240 ± 0.170
64	0.260 ± 0.180
68	0.380 ± 0.170
72	0.720 ± 0.420

Table B.10: $\theta_p/\theta_\alpha = 110^\circ / -26.6^\circ$

E_p (MeV)	A_y
28	-0.280 ± 0.260
32	-0.044 ± 0.170
36	-0.049 ± 0.150
40	0.012 ± 0.130
44	0.220 ± 0.140
48	0.160 ± 0.140
52	0.310 ± 0.160
56	0.180 ± 0.170
60	0.780 ± 0.210
64	0.330 ± 0.180
68	0.650 ± 0.170